Ad Lucem

Quantum Electrodynamic

Parton Distribution Functions

Ricky Nathvani

A dissertation submitted in partial fulfillment

of the requirements for the degree of

Doctor of Philosophy

of

University College London.

Department of High Energy Physics

University College London

August 24, 2019

I, Ricky Nathvani, confirm that the work presented in this thesis is my own. Where information has been derived from other sources, I confirm that this has been indicated in the work.

Abstract

Parton Distribution Functions are sets of functions that provide the momenta distributions of the constituent particles within a hadron, typically the proton, at different energy scales. This thesis describes the inclusion of Quantum Electrodynamics (QED) corrections to the existing set of MMHT (Martin, Motylinski, Harland-Lang, Thorne) Parton Distribution Functions (PDFs) which contains the photon PDF of the proton. Adopting an input distribution from the LUXqed formulation, a consistency is found with other recent sets and the methods of including QED effects for the full, coupled Dokshitzer-Gribov-Lipatov-Altarelli-Parisi (DGLAP) evolution of all partons with QED at $\mathcal{O}(\alpha)$, $\mathcal{O}(\alpha\alpha_S)$, $\mathcal{O}(\alpha^2)$ are discussed. Building on this, a set of QED corrected neutron PDFs are presented and the photon PDF provided, separated into its elastic and inelastic contributions. The resultant effects of QED on the other partons are investigated, as well as the effects of the evolution on the fit quality of the PDFs, whilst outlining the sources of uncertainty for the photon. Finally the phenomenological implications of this set are explored, giving the partonic luminosities for both the elastic and inelastic photon interactions and the effect of our photon PDF on fits to high mass Drell-Yan measurements with the inclusion of photon initiated processes.

Impact Statement

The work undertaken during my doctorate, as outlined in this thesis, was towards the development of an improved model of the proton - the most common particle accelerated in collisions at the Large Hadron Collider (LHC) to study the nature of matter.

In the collisions that occur between protons at the LHC, the constituent particles inside the protons, the quarks and gluon, interact to create products of interest to particle physicists, such as Higgs Bosons. Generating such products from proton collisions (and observing their subsequent decays) has been one of the bread-and-butter approaches in recent decades that physicists have used to investigate matter at the smallest scales. A model of the energy content carried by the quarks and gluons within the proton is vital to making predictions about the outcomes of such collisions.

My doctoral work has focused on augmenting the theoretical model of these quarks and gluons (known as Parton Distribution Functions) inside protons to include the photon as an additional particle that may interact in LHC collisions and other experiments where protons are accelerated at high energies. The sorts of products capable of being produced by photon collisions, rather than those typically initiated by quarks and gluons, can often be distinctly different and this approach may open a new way of investigating particle collisions in processes where the protons only collide peripherally, unlike current approaches where one can only predict their dynamics in head-on collisions. Furthermore, certain production mechanisms of Higgs Bosons are sensitive to photon collisions at the LHC, increasing the need to consider the photon's presence in the proton.

In general, an enhanced picture of the internal structure of the proton leads to improved accuracy in the theoretical predictions made by physicists about what kinds of behaviour they anticipate at the smallest scales of matter, supporting in a very broad way the work undertaken at the LHC. In the process of improving this model of the proton, similar work was also done to augment the model for the neutron, which could improve theoretical predictions in nuclear physics experiments.

Furthermore, Parton Distributions, which this thesis is concerned with, are often central pieces of evidence in the planning of future proton collider experiments.

The technical nature of particle physics experiments is such that the influence institutions such as the LHC exert on the public and industry are not attributable to a single individual. Publications often involved thousands of authors (such as for the discovery of the Higgs), citing the work of hundreds of other researchers. Therefore, I see the contributions I have made in this space as supporting the general efforts of the particle physics community which, as noted in STFC impact reports, has an outsized impact on generating enthusiasm from the public for fundamental research. I have had first hand experience of this have been involved in numerous outreach events to directly disseminate the scientific value of my work to the public. Lastly, the communal expertise of particle physics is often seen to guide the production of novel technologies in industry.

“Le but de ce travail est de munir son auteur du grade de Docteur,”

- Adrien Douady

Acknowledgements

This thesis represents the culmination of three and three-quarter years of work and play, both of which were supported by countless people. Throughout this text, we make reference to a variable "Bjorken" x, named after James 'BJ' Bjorken, who quipped "Theoretical physics is a socially acceptable form of mental illness." While this might be a somewhat exaggerated view, it is certainly true that the acceptance of our peers is what facilitates us to undertake work considered so esoteric and complex.

Therefore, I would like to thank my family for having supported me during this time and offering their unconditional support in times of need. I would also like to thank the friends I started this PhD with as I returned to London. Throughout every hardship, personal difficulty, struggle and frustration my dearest friends from St Hilda's College have shown me that friendships are sustained well beyond the contexts in which they are made. Their continuing support in the years spent pursuing my doctorate has given me the strength to push through, even when things looked bleak, and I am deeply indebted to their kindness. Particular gratitude to Peter Bradshaw, Callyane Desroches, Adam Gethin-Jones, Ramsay Gray-Stephens, Piotr Oleśkiewicz and Raphaëlle Vallet for countless hours spent entertaining my grievances and celebrating all the little successes with me on the way.

Furthermore, one of the most valuable developments for me during my time at UCL was the forging of new friendships along the way. Every member of the UCL HEP department has contributed to the welcoming and outgoing environment I had the privilege to enjoy for the last few years, and I extend my thanks to every staff member in the group. To my fellow PhD students I also extend a heartfelt grati-

tude for providing the most enjoyable, interesting and meaningful time I could have had during a PhD. Every last minute complaining about code, arguing about politics, wildly speculating on fringe physics and making fun our shared experiences in D109 and D14 has been an absolute joy. It goes without saying that I'm glad to know we'll continue to share those moments, even if we no longer share an office, for years to come. I could not have had better companions to undertake this journey with.

Being in London for the duration of the work undertaken in this PhD has been a mixed blessing, and it has been with a combination of envy and sympathy that I have seen so many of my friends come and go through this mad city during my PhD. Throughout that time, three of my friends, who have been present since my very first days stumbling through universities, have given me a sense of home and an unwavering sense of security at all times. Iain Frenkiel, Sabrina Slater and Tim Thomas, thank you for your friendship. Wherever we all may go from here, to have made it through this all is in no small part thanks to your help.

I wish to acknowledge that science is an inherently collaborative enterprise and the work undertaken for this thesis is no exception. My deepest thanks to Alan Martin for his invariably insightful comments on every talk, report and paper I have written. They have all been so much the better for your wisdom. Sincerest thanks to Lucian Harland-Lang for his pleasant, patient and understanding manner while guiding me through various parts of the MMHT framework throughout the years and sharing his extensive expertise.

Finally, my sincerest and heartfelt thanks to Robert Thorne for granting me the opportunity to undertake such rewarding scientific work, guiding me through every difficulty and providing unwavering support, understanding and clarity at every step of the way. As well as the thanks due for the sizeable amount of effort on your part to help me produce the work outlined in the text, I would like to give thanks for leading by example and setting the standard for having tenacity, insight and integrity as a researcher. It has influenced me deeply and I hope to bring the same values into any future undertaking.

Contents

List of Figures

List of Tables

Chapter 1

Introduction

1.1 Background

Though the results of experiments bear out its predictions extraordinarily well, many questions remain about the Standard Model of Particle Physics, such as the nature of mass hierarchies observed in particles and the lack of explanation for astronomically observed Dark Matter [1]. In the hopes of shedding light on these phenomena, the precision physics program at the Large Hadron Collider (LHC) aims to observe processes with unprecedented accuracy and experimental sensitivity. As part of these efforts, the majority of analyses conducted by the ATLAS and CMS collaborations have been undertaken with theoretical cross section predictions at Next-to-Leading Order (NLO) in Quantum Chromodynamics (QCD), with $\mathcal{O}(\alpha_S)$ corrections, and increasingly many at Next-to-Next-to-Leading Order (NNLO) in QCD [2] ($\mathcal{O}(\alpha_S^2)$ corrections). At this level of precision, it is expected that electroweak (EW) corrections, including those with photon initiated processes, will begin to have observable effects as $\alpha_{QED} \gtrsim \alpha_S^2$ at the typical scales being probed at the LHC and should therefore be incorporated in theoretical predictions. As a result, developments are needed to match electroweak corrected partonic cross sections with corresponding Parton Distribution Functions (PDFs), $xf(x,Q^2)$, calculated at NLO and NNLO in QCD and the appropriate orders in Quantum Electrodynamics (QED).

This is achieved primarily by modifying the factorisation scale evolution of

the PDFs (governed by the Dokshitzer-Gribov-Lipatov-Altarelli-Parisi or DGLAP equations [3, 4, 5]) to include QED parton splittings. The most apparent effect of this change is the necessary inclusion of the photon as constituent parton of the proton. Subsequently one can also begin to calculate the effect of photon-initiated (PI) subprocesses as corrections to the leading QCD cross section of processes such as Drell-Yan [6], EW boson-boson scattering [7] and Higgs production with an associated EW boson [8], which are expected to be experimentally sensitive to these effects.

In addition to providing corrections to processes typically initiated by the other partons of the proton, semi-exclusive [9] and exclusive production of states with EW couplings are naturally dependent on the photon content of the proton, where PI processes play an important role (as shown in recent studies [10, 11] in the context of compressed SUSY scenarios).

The Martin-Roberts-Stirling-Thorne group (MRST) provided the first such publicly available QED set [12], modelling the photon at the input scale as arising radiatively from the quarks (with their respective charges) below input, using DGLAP splitting kernels at $\mathcal{O}(\alpha)$ in QED. Other such sets were subsequently developed that either adopted similar phenomenological models [13], or sought to constrain the photon analogous to other partons by fits to Drell-Yan data [14][15], first developed by the NNPDF Collaboration. These early sets saw relatively large discrepancies between photon PDFs. Large modelling uncertainties persisted due to the freedom in the assumption of the scale above which photons are produced radiatively, an uncertainty modelled in the MRST set as the difference between the current and constituent quark masses, while the approach taken by the CTEQ14QED set [13] was to attempt to fit a parameterisation based on the total momentum carried by the photon from $ep \to e\gamma + X$ data. In the case of NNPDF23QED [14], which sought to fit the photon distribution primarily from di-lepton/Drell-Yan production with little model dependency, the constraints available from the small PI contributions directly from the data were rather weak, leading to large errors, with $\mathcal{O}(100\%)$ uncertainty at high x. In all cases the available data was unable to con-

strain the photon to a high degree of accuracy.

A final significant drawback of these early sets was that the majority did not account for the contribution to the photon PDF from elastic scattering processes, in which the proton coherently emits electromagnetic radiation without disintegration, in contrast to photon contributions previously accounted for from inelastic scattering processes, assumed to arise from quark splittings. This distinction between the "inelastic" and "elastic" photons was one that was seldom systematically treated, if considered at all.

Significant strides have been made in recent years to overcome these deficiencies. First, more accurate determinations of the photon distribution at input have been developed by making use of the experimentally well determined elastic form factors of the proton (F_2^{el}, F_2^{inel}). These approaches are predicated on the equivalence between the electromagnetic field used to probe proton structure and the photon PDF. This was outlined in a work by Martin and Ryskin [16] and further developed by the Harland-Lang, Khoze and Ryskin group (HKR) [17], who also investigated their application to central exclusive production in hadron-hadron colliders [18]. Theoretical work was also undertaken by the LUXqed group to demonstrate a rigorous theoretical equivalence between the internal photon line in both elastic and Deep Inelastic Scattering (DIS) processes and the photon PDF of the proton. They also provided the first photon set based on this formulation [19].

In addition to these developments, QED DGLAP splitting kernels have now been calculated to $\mathcal{O}(\alpha\alpha_S)$ [20] and $\mathcal{O}(\alpha^2)$ [21], whose effects, as shown in Section 6.3, are not insignificant to the evolution of the photon and other partons. Finally, since the elastic and inelastic form factors for the proton have been experimentally determined to a high precision, this has in turn allowed for the determination of the elastic and inelastic contributions to the photon to the level of, at most, a few percent.

In light of this, a greater confidence may be had regarding the effects of QED modified partons and their impact on total cross section calculations which, although investigated previously, could not be determined with a high degree of ac-

curacy.

In this thesis, the work undertaken to develop a fully consistent set of QED partons in the MMHT framework is described, adopting the LUXqed formulation at input for the photon, $x\gamma(x, Q_0^2 = 1\ \text{GeV}^2)$. Chapters 2 - 5 provide a broad background to PDFs and a more in depth discussion of the inclusion of QED in PDF sets. Chapters 6 - 9 are based on an article currently being prepared for submission to a journal that has been co-authored along with other members of the MMHT group, but it is emphasised that **all the text within this thesis has been written by the author, with all figures, unless otherwise stated, produced independently from data that has resulted from calculations carried out by the author.**

A broad summary of the work undertaken for this thesis is as follows. QED splitting kernels of $\mathcal{O}(\alpha)$, $\mathcal{O}(\alpha_S)$ and $\mathcal{O}(\alpha^2)$ are incorporated into the usual DGLAP evolution for all partons and the effect of these kernels is also explored. Furthermore, a model is adopted for Higher Twist (HT) effects in the quarks at low Q^2, since the evolution of the photon PDF, $x\gamma(x,Q^2)$, is sensitive to these corrections due to a lower starting scale in comparison to that of other PDF sets.

As well as the conventional set of QED altered PDFs, the efforts to provide grids containing the photon PDF separated into its elastic and inelastic components is detailed, as well as a consistent set of QED corrected neutron PDFs. Although the phenomenological implications of a neutron set are limited, their production is necessary for a consistent fit to deuteron and nuclear fixed target data from neutrino (νN) DIS scattering experiments used to constrain the PDFs, where the nuclei consist of large numbers of both nucleons. The QED corrected neutron PDFs of MRST [12] provided isospin violating partons, with $u_{(p)} \neq d_{(n)}$, (as discussed in Section 7.2), which were seen to reduce the NuTeV $sin^2\theta_W$ anomaly [22]. The breaking of isospin symmetry may also have implications for the development of nuclear PDFs, and our current treatment develops on our earlier approach, with new predictions for the magnitude of isospin violation.

Finally, the phenomenological consequences of this set are explored, demonstrating the effects of QED incorporation on $F_2(x,Q^2)$ as calculated from PDFs, the

partonic luminosities as a function of Centre-of-Mass (CoM) energy (which are expected to be significant for projects such as the Future Circular Collider) and the change in the fit quality after refitting the partons with QED. The consequences of fitting to high mass Drell-Yan data itself, provided by the ATLAS experiment [23], is explored with both QED effects and Photon-Initiated corrections to the cross section produced by the set, which also demonstrates that the effects of a fully coupled QED DGLAP evolution is non-negligible on the gluon and quark PDFs.

1.2 Units and Notation

Throughout this thesis, the natural-units system of particle physics is used. The base dimensions adopted are: the speed of light c, angular momentum (denoted in units of the reduced plank constant $\hbar$, and energy (typically represented in Giga-electronvolts or GeV, unless otherwise mentioned throughout this thesis). In the natural-units system, the first two are defined as $c = \hbar = 1$, and are therefore suppressed in the notation for dimensional quantities, such that energy, momentum, and mass are all uniformly expressed in units of GeV. Electric charge, where given, will be expressed in units of the elementary charge, which relates to the SI (Système International) units as $1e \simeq 1.6 \times 10^{-19}$ C (Coloumbs). Where a dot product between two for vectors is performed $p \cdot q$, the metric adopted is diag $(+,-,-,-)$. Unless otherwise defined, x will refer to the fraction of the proton's momentum carried by the partons (as explained in Section 3), while Q^2 will refer to energy scales (squared) in the context of Deep Inelastic Scattering, where the context will make clear whether it refers to the invariant mass squared of the outgoing products or the energy scale in the evolution of the partons. Where the index i is used in the context of PDFs (e.g. q_i or f_i), it will serve as an index for the active (kinematically available, $Q^2 > m_{q_i}$) flavours of quarks or partons, and summation of this index $\sum_i$, indicates that the sum of all relevant partons is being considered.

Chapter 2

Standard Model

The reductionist paradigm of physics, to understand the universe by comprehending the composition and dynamics of its most fundamental constituent parts, made significant strides in the 20th century. This program culminated in the development of a theory whose predictions about the smallest probed scales of matter have yet to be surpassed by a more accurate [24] or predictive theory: The Standard Model of Particle Physics (SM).

Historically, modern particle physics followed the development of the atomic model of Rutherford [25], Chadwick [26] and others in the 1920s and '30s and built on the enhanced understanding of the dynamics of matter provided by Quantum Mechanics (as developed by Bohr, Heisenberg, de Broglie, Schrödinger and others [27]). Subsequently, an explosion of interest in particles and their possible interactions occurred over the next few decades, driven by experimental design and observation.

The framework developed to describe the known particles and their interactions in a unified way takes the form of a Quantum Field Theory (QFT), where the predictions of the theory (e.g. scattering cross sections, decay rates, masses) are typically derived from the Lagrangian formulation of quantum mechanics (in a manner consistent with special relativity). That is, for a given initial state $|i\rangle$ and final state $\langle f|$, both of which describe distinct particle content and kinematics, the scattering amplitude A is given by $A = \langle f| e^{iS[\psi]} |i\rangle$, where S is the action given by the space-time integral over the Lagrangian density, $S[\psi] = \int d^4x \ \mathscr{L}(\psi)$, and $\psi(x)$

denotes the field content of the theory as a function of the space-time co-ordinates $x = (t, \vec{x})$. Note that while this notation is used throughout this section, in general, x will have a different meaning in the context of partonic momentum for the majority of this thesis (as explained in the next section). Furthermore, following convention, for simplicity the Lagrangian density $\mathscr{L}$, is henceforth referred to simply as the "Lagrangian".

It is the formulation of $\mathscr{L}(\psi)$ which the SM describes. In general, the SM Lagrangian, $\mathscr{L}_{SM}$, encapsulates the interactions of two classes of particle. The particles themselves arise as products of the canonical quantisation of classical fields, which are distinguished by their symmetry properties under the transformations of the Lorentz group: fermions, which have half integer spin and are represented as $\psi(x)$ for a spin $\frac{1}{2}$ spinor Dirac field, and bosons of integral spin (whose notation is introduced below).

The structure of $\mathscr{L}_{SM}$ arises from the mathematical principle of gauge symmetry, in which the fields are required to obey certain symmetry considerations (outlined below). The generators of these symmetries are then naturally seen to give rise to the bosonic field content of $\mathscr{L}_{SM}$ (with the exception of the Higgs boson, which we shall also briefly outline).

The gauge symmetry structure of the SM Lagrangian can be introduced from an inspection of the Dirac free particle Lagrangian:

$$\mathscr{L}_{\psi} = \bar{\psi}(i\gamma^{\mu}\partial_{\mu} - m)\psi, \tag{2.1}$$

which, upon use of the Euler-Lagrange equations, yields the dynamics of a free fermionic field (the Dirac equation). Interactions between fermions and bosons may then be introduced to this model by imposing the condition of invariance of the Lagrangian under gauge transformations of the fields $\psi(x) \rightarrow \mathbf{g}(x)\psi(x)$, related to a particular group G, $\mathbf{g}(x) \in G, \forall x$ (which resemble a local phase transformation of the form $\psi(x) \rightarrow e^{it_a\theta^a(x)}\psi$).

One eventually determines that in order to satisfy this condition for Eq. (2.1), one must substitute in place of the ordinary partial derivative ∂_{μ} a covariant deriva-

tive (a more complete discussion of which may be found in chapter 10 of [28]):

$$D_\mu = \partial_\mu - igA_a^\mu t^a. \tag{2.2}$$

In this expression, A_a^μ are the bosonic fields associated with the gauge group under consideration, t^a the generators of the group G (with the index a labelling each generator) and g coming to represent the strength of coupling between the fields and the fermions, or between the fields themselves as in the case of a non-abelian group. For simplicity, we shall often refer to the sum of these fields, as simply $A^\mu = A_a^\mu t^a$. Under a gauge transformation, the fields transform as:

$$A^\mu \to \mathbf{g}(x)A^\mu \mathbf{g^{-1}}(x) + \frac{i}{g}(\partial_\mu \mathbf{g}(x))\mathbf{g^{-1}}(x). \tag{2.3}$$

This property is deduced from the imposition of the fact that gauge invariance must be preserved and that the fields enter the Lagrangian through the field strength tensor, given by:

$$F_{\mu\nu}^a = \partial_\mu A_\nu^a - \partial_\nu A_\mu^a + g f_{bc}^a A_\mu^b A_\nu^c, \tag{2.4}$$

where f^{abc} are the structure constants that define the properties of the group (under the commutation of its members): $[t_a, t_b] = \sum_c f_{ab}^c t_c$. As explained below, the field strength tensor in turn enters the Lagrangian in the form $-\frac{1}{4}F_{\mu\nu}F^{\mu\nu}$, which remains invariant under the transformation properties outlined in Eq. (2.3).

The SM involves the invariance of the Lagrangian under three particular groups, each of which introduces their own gauge fields A_a^μ (and associated bosons): an $SU(3)$ gauge group [29, 30, 31, 32, 33], responsible for the "strong nuclear force", or Quantum Chromodynamics (QCD), whose gauge bosons are referred to as gluons, and a electric and "weak nuclear force", or electroweak force (EW) based on the gauge groups $SU(2) \times U(1)$ [34, 35, 36] (whose boson content is elaborated below). The latter symmetry is "spontaneously broken", due to its interactions with the Higgs field, a separate complex scalar $SU(2)$ weak doublet field, $\phi = [\phi_+, \phi_0]^T$, which is seen to be necessary to preserve the gauge invariance of mass terms ($\sim \psi^2, \sim A^\mu A_\mu$), as detailed below.

While the entirety of the Standard Model Lagrangian would be cumbersome to reproduce (due to the large number of fields and their possible interactions), a general idea of its structure and the dynamics that arise from each part may be obtained from inspection of the generalised form provided below:

$$\mathscr{L}_{SM} = -\frac{1}{4}F_{\mu\nu}F^{\mu\nu} + i\bar{\psi}(i\gamma^{\mu}D_{\mu})\psi + y\bar{\psi}\psi\phi + |D_{\mu}\phi|^2 - \mu^2\phi^{\dagger}\phi - \lambda(\phi^{\dagger}\phi)^2. \quad (2.5)$$

Taking each term in isolation:

- $-\frac{1}{4}F_{\mu\nu}F^{\mu\nu}$ represents the dynamics of the gauge fields; both their propagation and self interaction terms. For Abelian groups (such as $U(1)$) the group structure constants $f^{abc} = 0, \forall c$ and therefore, from inspection of Eq. (2.4), do not contain gauge boson self-interaction terms at leading order.

- $i\bar{\psi}(i\gamma^{\mu}D_{\mu})\psi$ describes not only the free propagation of fermions as described above, but also introduces interaction terms: $ig\bar{\psi}\gamma^{\mu}A_{\mu}\psi$, which describes a vertex between fermion fields and a gauge boson.

- $y\bar{\psi}\psi\phi$ describes the Yukawa interactions of fermions with the scalar Higgs field ϕ.

- $|D_{\mu}\phi|^2$, analogous to the covariant derivative term for fermions, describes the propagation of the free Higgs field as well as its interactions with gauge bosons.

- $-\mu^2\phi^{\dagger}\phi - \lambda(\phi^{\dagger}\phi)^2 \equiv -V_H(\phi)$ describes the potential of the Higgs field (with $\mu^2 < 0$ and $\lambda > 0$, such that the potential is bounded from below), which also incorporates the dynamics of the Higgs self interactions. The minima of this potential creates a continuous spectrum of vacuum state solutions for $|\phi|$ (with a degeneracy in three of the massless real scalar fields of the complex doublet field of the Higgs), leading to spontaneous symmetry breaking.

The introduction of the scalar Higgs field ϕ, serves multiple purposes from a theoretical perspective. The idea of a scalar field potential was introduced into the

SM long before the observation of the Higgs boson in 2012 [39, 40] (the associated particle excitation associated with the field), in order to produce gauge invariant particle mass terms from Yukawa couplings. Specifically, mass terms for bosons, of the form $mA_\mu A^\mu$, when subjected to a transformation in the manner of Eq. (2.3) do not ordinarily maintain gauge invariance.

In the absence of the Higgs field (or some alternative mechanism), the absence of gauge invariant mass terms in the SM Lagrangian would be impossible from a theoretical perspective to reconcile the observed massive gauge bosons associated with the weak force. Furthermore, the cross section for longitudinal $W-W$ boson scattering grows without bound in the SM, violating unitarity at the TeV scale, and without the gauge invariance imposition on the electroweak force (which ordinary boson mass terms do not obey), there would be no assurance of the renormalisability of the theory [41], discussed in more detail below.

In broad terms the Higgs-Brout-Englert-Guralnik-Hagen-Kibble mechanism [42, 43, 44, 45] (hereon referred to simply as the Higgs mechanism, following convention) resolves these problem in the following manner. Unlike all other terms given in Eq. (2.5) (whose energy is minimised by $\psi, F_{\mu\nu} = 0$), the vacuum state of the Higgs field potential, $V_H(\phi) = \mu^2\phi^\dagger\phi + \lambda(\phi^\dagger\phi)^2$, is minimised for the following condition:

$$|\phi| = \sqrt{\frac{-\mu^2}{\lambda}} \equiv v, \tag{2.6}$$

where we note that because the field ϕ is a weak $SU(2)$ doublet, its normalisation follows the convention $\phi^\dagger\phi = |\phi|^2/2$ (which in turn, defines the field magnitude $|\phi|$ in Eq. (2.6)). Thus, while the magnitude of the vacuum Higgs state is fixed, there is a degeneracy (or symmetry) of solutions due to the choice in phase about the origin of the potential. Once we define, by convention, a particular choice for the phase however, this "breaking" of the symmetry (the selection of a particular vacuum state), leads to a corresponding breaking of the $SU(2)\times U(1)$ electroweak symmetry, and gives the effective gauge bosons that result from this symmetry breaking, gauge invariant mass terms.

A brief outline of the derivation is given below, with interested readers referred

to chapter 7 of [37]. Fixing the phase of the vacuum, using the conventional choice of the unitary gauge, one may write the vacuum state of the Higgs field as:

$$\langle \phi \rangle = \frac{1}{\sqrt{2}} \begin{bmatrix} 0 \\ v \end{bmatrix}. \tag{2.7}$$

Furthermore, the covariant derivative associated with the (unbroken) $SU(2) \times U(1)$ electroweak symmetry, is given by:

$$D_\mu^{(EW)} = \partial_\mu + ig' B_\mu + ig \frac{\tau_a}{2} W_\mu^a, \tag{2.8}$$

where $g' B_\mu$ corresponds to the gauge field and coupling for the $U(1)$ group and $\tau_a W_\mu^a$ the weak doublet fields for the $SU(2)$ group (which indicates that the generators τ_a correspond to the normalised Pauli matrices such as those used in the spin $1/2$ algebra of Quantum Mechanics). We now consider the effect of excitations of the Higgs field, about the minimum of the vacuum, expressed as:

$$\phi = \frac{1}{\sqrt{2}} \begin{bmatrix} 0 \\ v + \eta(x) \end{bmatrix}. \tag{2.9}$$

The term $|D_\mu \phi|^2$ was constructed as manifestly gauge invariant, and we may consider the resultant field content of the Lagrangian upon substituting the expression for the field as given in Eq. (2.9), which yields (after a few lines of algebra):

$$|D_\mu \phi|^2 = \frac{1}{2}(\partial_\mu \eta)(\partial^\mu \eta) + \frac{1}{8}(v+\eta)^2 (g'^2 B_\mu B^\mu + g^2 W_\mu^a W^{\mu,a} - 2gg' B_\mu W^{3,\mu}). \tag{2.10}$$

The first part of this equation represents the free propagation of the excited Higgs fields, while the latter represents the interactions of this fields and the vacuum state with the fields. It is the latter contribution which is seen to give the gauge bosons a gauge invariant form of mass. Here we introduce redefinitions of the fields, W_μ^a, B_μ, which we shall see, come to represent the mass eigenstates of the field content

of the theory:

$$W_\mu^\pm = \frac{1}{\sqrt{2}}(W_\mu^1 \pm iW_\mu^2), \qquad Z_\mu = \frac{-gW_\mu^3 + g'B_\mu}{\sqrt{g^2+g'^2}}, \tag{2.11}$$

$$A_\mu = \frac{gB_\mu + g'W_\mu^3}{\sqrt{g^2+g'^2}}. \tag{2.12}$$

The fields in Eq. (2.11) represents the massive gauge bosons of the broken weak $SU(2)$ symmetry (the experimentally investigated weak nuclear force), while A_μ in Eq. (2.12) will come to represent the massless $U(1)$ gauge boson, i.e. the photon, associated with Quantum Electrodyanmics (QED). This is seen upon the substitution of these definitions into the term between the brackets of Eq. (2.10):

$$g'^2 B_\mu B^\mu + g^2 W_\mu^a W^{\mu,a} - 2gg' B_\mu W^{3,\mu} = (g^2+g'^2) Z_\mu Z^\mu + 2g^2 W_\mu^+ W^{-\mu}. \tag{2.13}$$

Note that the term A_μ, is absent from this expression, indicating that the mass of the photon is zero and that three and four vertex Higgs-photon point interactions are forbidden in the SM. For the remaining gauge bosons, an inspection of Eq. (2.10) shows that when the coefficient of this term is expanded, it will contain a constant term (proportional to the vaccum expectation of the Higgs field), $v^2/8$, which, using the fact that bosonic mass terms in QFT have the form $m^2\varphi^2/2$ yields $M_W = gv/2$ and $M_Z = (g^2+g'^2)^{1/2}v/2$.

The effective coupling of the A_μ field that emerges from this mechanism to the fermions also differs from the naïve coupling one obtains by inspection of the coefficient of the original $U(1)$ B_μ field given in Eq. (2.8). After redefining the fields in terms of the mass eigenstates given above, the $i\bar{\psi}(i\gamma^\mu D_\mu)\psi$ terms in the SM give rise to terms of the form $ie\bar{\psi}\gamma^\mu A_\mu \psi$, where e is an effective coupling related to the original couplings in Eq. (2.8) in the following manner:

$$e = \frac{gg'}{\sqrt{g^2+g'^2}}. \tag{2.14}$$

It is this coupling e, which differs for the fermion field in question, that repre-

sents the electromagnetic couplings of the fermions to the photon in QED, as listed in Table 2.1.

Terms that contain the excited Higgs field η then represent interactions with the bosons (leading to couplings of the form ZZH, WWH, $ZZHH$ and $W^+W^- \to HH$, etc). The issue of gauge invariant masses for the fermions meanwhile is resolved by noting that the term $y\bar{\psi}\psi\phi$, will also contain a term proportional to the constant vacuum expectation value v, and are quadratic in the fields (and hence create mass eigenstates). This works in particular, because all left-chiral fermions in the SM, whether they carry the "colour" charge associated with the $SU(3)$ symmetry of QCD (quarks) or not (leptons) are arranged in weak doublets that also couple with the Higgs field, and therefore its vacuum expectation value.

Of further note is the fact that the effective mass of the fermions, is then seen to be proportional to the coupling between those fields and the Higgs, y, which are free parameters in the model. In fact, y is more completely represented as matrices y_{ij}, which leads to a rotation between the mass eigenstates of the theory and the weak interaction states. By convention, the rotation in quark flavours is defined solely for the down type quarks, yielding the Cabibbo-Kobayashi-Maskawa [46, 47] or CKM matrix, while for the leptons it is defined for the neutrino flavour states in terms of the Pontecorvo-Maki-Nakagawa-Sakata [48, 49] or PMNS matrix. Since this thesis is primarily concerned with the interactions in QCD and those of QED, we neglect this component for our purposes and refer the reader to section 9.6 of [28].

A final feature of the weak force that is of importance in the SM is that the $SU(2) \times U(1)$ gauge group is chiral. The charged, massive gauge bosons of the group couple exclusively to left-chiral fermions i.e. those fermion fields which are eigenstates of the left chiral projection operator: $P_L = (1 - \gamma^5)/2$, where γ^5 is related to the standard Dirac matrices by the relation $\gamma^5 = i\gamma^0\gamma^1\gamma^2\gamma^3$. Chirality corresponds to handedness (the orientation of spin with respect to the direction of 3-momentum) in the massless limit, and for neutrinos, due to their extremely small masses (given below), one typically considered them occurring solely in the left handed helicity state. Practically speaking, the left-chiral nature of the electroweak

$SU(2)$ interactions has implications for the kinematics of particles in scattering processes involving the relevant gauge bosons, generating parity violation in certain interactions. Since the details of electroweak theory are beyond the scope of this thesis, we limit the discussion provided here.

Together, the weak gauge bosons W, Z, the photon A (more commonly described by the symbol γ) and the gluons (which we shall denote as g) comprise the forces of the SM. The fermion fields then consist of colour charged quarks and colourless leptons, which are also organised by three generations with identical coupling properties to gauge bosons but with different masses. A summary of the fermion and boson content of the SM is given below in tables 2.1 and 2.2, respectively, with their relevant properties provided. Note that the $\overline{MS}$ masses are given for all quarks except for the top quark, for which the pole mass is given, since its large mass means that it decays on timescales, $\mathcal{O}(1/m_t)$, much shorter than those that QCD causes quarks to hadronise in ($\mathcal{O}(1/\Lambda_{QCD})$). Because of this, the top quark is phenomenologically treated as a free particle, for which the pole mass is a more readily intepretable choice of mass scheme, unlike the light quarks whose behaviour can only be inferred from observations of the hadronic interactions, in which they are bound.

For the purpose of this thesis, we shall be primarily concerned with the quarks, u, d, c, s, b, (where the top is excluded for much of our theoretical discussion since its large mass prohibits its appearance at the energy scales concerned) and the gauge bosons of QED and QCD, the photon (γ) and the gluons.

In the next chapter, an overview of QCD in the framework of hadrons and Deep Inelastic Scattering (DIS) is presented, the original context in which the theory of QCD was developed (since quarks themselves are never observed in isolation). However, in order to provide a comparison between the theories of QED and QCD, we provide a discussion of the primary vertices (i.e. the Feynman rules) for both theories, which will also be relevant to the discussion of splitting functions introduced in the next section.

As indicated above, the $U(1)$ theory of QED incorporates an abelian symmetry

	Particle		EM Charge	Mass [GeV]
Quarks	Up	u	$+\frac{2}{3}$	$0.002^{+0.0005}_{-0.0002}$
	Down	d	$-\frac{1}{3}$	$0.005^{+0.0003}_{-0.0004}$
	Charm	c	$+\frac{2}{3}$	$1.27^{+0.009}_{-0.003}$
	Strange	s	$-\frac{1}{3}$	$0.096^{+0.009}_{-0.003}$
	Top	t	$+\frac{2}{3}$	173.0 ± 0.4
	Bottom	b	$-\frac{1}{3}$	$4.18^{+0.04}_{-0.03}$
Leptons	Electron	e^-	-1	0.0005
	Electron neutrino	ν_e	0	$< 2 \times 10^{-9}$
	Muon	μ^-	-1	0.1057
	Muon neutrino	ν_μ	0	$< 1.9 \times 10^{-4}$
	Tau	τ^-	-1	1.777
	Tau Neutrino	ν_τ	0	$< 18.2 \times 10^{-3}$

Table 2.1: A table of the fermions in the SM, and their electromagnetic charges and experimentally measured masses [38]. Note that the bounds on the neutrino masses are taken from direct mass experiments, and that oscillation experiments provide an even stronger bound on all three masses of $\lesssim 2$ eV. Further note that the weak and strong charge couplings are neglected since the strong force couples to all quarks with uniform strength g_S and the weak force couples to all fermions universally with strength g_W, though with different hypercharges, which lead to Z couplings dependent on the chirality of the fermions (see chapter 9 of [28]). Colours correspond to groupings by "generations" in the SM, which represent identical doublets of fermions in the SM, distinguished by their masses. Antifermions (denoted using the bar notation, $\bar{f}$), share identical properties with the exception that the sign of their charges are reversed ($e_f = -e_{\bar{f}}$).

Particle		J^P	Mass [GeV]
Photon	γ	1^{-1}	0
Gluon	g ($\times 8$)	1^{-1}	0
W	$W^\pm$	1^{-1}	80.379 ± 0.012
Z	Z	1^{-1}	91.1876 ± 0.0021
Higgs	H^0	0^{+1}	125.18 ± 0.16

Table 2.2: A table of all bosons in the SM, their spin and parity properties and experimentally measured masses [38]. The $\times 8$ for the gluon represents the 8 gauge fields associated with each generator t^a (the Gell-Mann matrices) of QCD ($SU(3)$).

in the SM ($f^{abc} = 0$ such that there are no quadratic terms in the photon fields $A_\mu A^\mu$ in the Lagrangian). Therefore, (neglecting the mathematical details necessary for scattering calculations) the primary vertex in QED is simply that between a fermion and a photon as shown in Fig. 2.1.

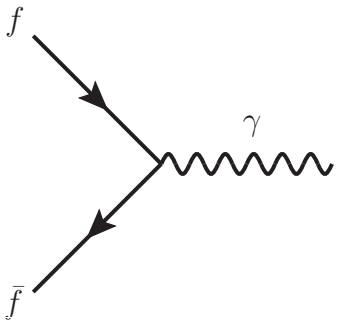

Figure 2.1: The primary (Leading Order) vertex in QED between a fermion line and a photon. The factor associated with vertex is the electromagnetic coupling between the fermion and the photon, e_f.

Higher order diagrams such as Next-to-Leading-Order (NLO), Next-to-Next-to-Leading-Order (NNLO) etc in QED are fundamentally comprised of copies of this vertex, where each additional vertex indicates a higher order in perturbation theory. In QCD meanwhile, as well as the coupling between quarks and gluons (which shares a virtually identical mathematical construction to Fig. 2.1 except for the strength of the coupling), gluon-gluon interactions are not only present, but play an important role even at LO QCD. These vertices are shown in Fig. 2.2.

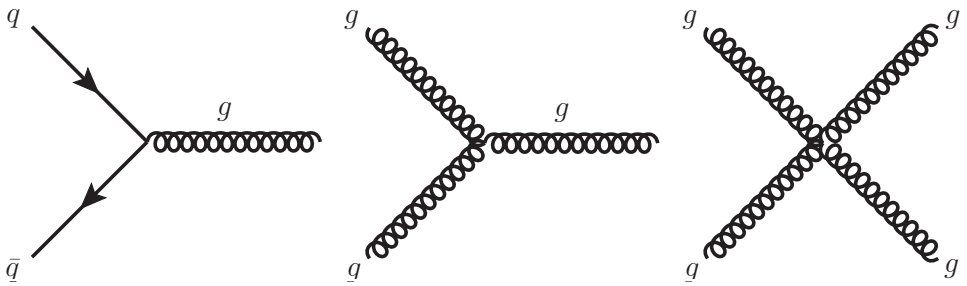

Figure 2.2: The primary (Leading Order) vertices in QCD between a quark line and a gluon, and the trilinear and quadrilinear gluon interactions. The vertex factor associated with each of these diagrams is g_s.

The presence of gauge boson self interaction terms in QCD is of crucial importance in how it is distinct from the other forces present in the SM. To highlight

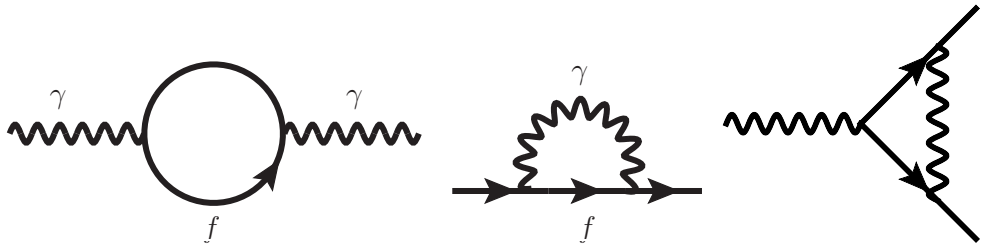

Figure 2.3: Loop correction diagrams in QED for (from left to right) a photon line, fermion line and vertex coupling. Note that other single loop corrections exist for the vertex, where one may replace any of the legs given in Fig. 2.1 with the loop corrections shown on the left and middle for the photon and fermion lines, respectively.

this, we conclude this chapter with a discussion of how the gauge couplings g_i, (and more generally other observables such as masses and decay rates) in the SM change as functions of the energy scale of the process. It is well known [50] that naïvely applying the Feynman rules adapted from certain QFT Lagrangians with constant coupling constants (and indeed masses) leads to logarithmically divergent predictions when computing higher order integrals ($\sigma \sim \int_0^\infty dQ^2[...]/Q^2 \to \infty$), particularly those which contain closed loops in the diagrams, as illustrated in Fig. 2.3. Such divergences are known as ultraviolet divergences, since the nature of the divergence corresponds to high (and prior to renormalisation, infinite) energy limits in the integrals.

The resolution to this is found with the procedure of regularisation, in which the kinematic upper limit to these integrals is bounded by some scale Λ, which is taken as much greater than the energy scales being probed $\Lambda \gg Q^2$. Alternatively, one may characterise the divergence by the dimensions in which the integral is performed $\int d^D k$, by extending the number of dimensions $D = 4 \to D = 4 - 2\varepsilon$, and calculating divergences as a function of the difference $(1/\varepsilon)$ from the usual 4 spacetime dimensions.

The procedure of renormalisation (details of which may be found in [51]), is then used to redefine the parameters of the theory (couplings, masses etc) in finite terms, but in doing so introduces a Q^2 scale dependence of the theory (and requires that the fixing of this scale depends upon empirical observation at some particular value, such that the parameters are not solely deducible from the theory alone).

We sketch how this is performed in the context of loop corrections in QED, which leads to renormalisable parameters. In general, renormalisation rescales divergent parameters, ϕ, such that the ultraviolet divergent components are "absorbed" into a rescaling constant: $\phi \to \phi_0 = Z\phi$, where the subscript 0 represents the bare quantity and Z the scaling constant into which divergences are absorbed. In the instance of the electric charge coupling of QED, $g_e \equiv e$, the scaling is of the form $e_0^2 = e^2/Z_3^2$, more conveniently expressed as $e^2 = Z_3^2 e_0^2$. The subscript 3 is used since (excluding the mass renormalisation scaling term Z_m), the three scaling parameters of QED are $Z_{1,2,3}$, which denote the vertex, fermion and photon wave function renormalisation constants.

In an abelian theory, the renormalisation of the coupling constant is insensitive to $Z_{1,2}$ (the scaling constants for the vertex and fermion line) and is dependent solely on that of the photon wavefunction scaling, though this does not hold true in non-abelian gauge theories. Nonetheless, for QED, we may restrict our attention to Z_3 in this context.

The one loop correction corresponds to the leftmost diagram of Fig. 2.3. If the leftmost photon line in this diagram is labelled by the index a with spacetime index μ, four-momentum q and the rightmost photon line is indexed by b with spacetime index ν and the momenta in the fermion loop denoted as k and $q+k$ (for either fermion or antifermion lines), then the photon "self-energy" (the amplitude expressed by the graph), $i\pi^{ab}_{\mu\nu}(q)$ is given by:

$$i\pi^{ab}_{\mu\nu}(q) = -4\pi\alpha \int \frac{d^4k}{(2\pi)^4} \frac{Tr[\gamma_\mu(\not{k}+\not{q}+m)\gamma_\nu(\not{k}+m)]}{(k^2-m^2+i0^+)((k+q)^2-m^2+i0^+)}, \tag{2.15}$$

where we introduce a widely used alternative notation for the coupling strengths $\alpha(Q^2) = \frac{g^2(Q^2)}{4\pi}$ and use the terminology 0^+ rather than ε to denote a small shift around the complex pole in the propagator, since it will have a different usage in the context of dimensional regularisation.

Since $d^4k \sim k^3dk$, counting powers of the loop momentum k in the numerator and denominator, on finds the integral scales as $\int_0^\Lambda d|k|k \sim \Lambda^2$ (which leads to a quadratic divergence). However, as discussed in [52], the property of gauge

invariance requires that $\pi_{\mu\nu}$ obeys the proportionality relation: $\pi_{\mu\nu} = (g_{\mu\nu}q^2 - q_\mu q_\nu)\Pi(q^2)$. While the leading factor is finite, the term $\Pi(q^2)$ causes the integral to diverge logarithmically, rather than quadratically as would otherwise be assumed, and is responsible for the ultraviolet divergence of photon self interaction.

As briefly described above, the process of dimensional regularisation then proceeds by changing the number of dimensions in which the integral is evaluated in the following manner:

$$4\pi\alpha\frac{d^4k}{(2\pi)^4} \to 4\pi\alpha(\mu^2)^\varepsilon\frac{d^{4-2\varepsilon}k}{(2\pi)^{4-2\varepsilon}}. \tag{2.16}$$

This expression will be seen to diverge for $\varepsilon \to 0$, but, as shown below it allows us to characterise the form of the divergence of the integral in terms of $1/\varepsilon$. Performing the regularised integral then yields:

$$\Pi(q^2) = -\frac{\alpha}{2\pi}\Gamma(\varepsilon)\int_0^1 dx\left(\frac{4\pi\mu^2}{m^2 - x(1-x)q^2}\right)^\varepsilon 2x(1-x), \tag{2.17}$$

where $\Gamma(z)$ represents the Gamma function of the form $\Gamma(z) = \int_0^\infty dx\, x^{z-1}e^{-x}$. Here we omit the details of the integration and evaluation of the $\Gamma(\varepsilon)$ function, (referring the reader to [52] for a more complete treatment) and highlight the salient result, which is that the divergence of $\Pi(q^2)$ occurs for $\Pi(0)$, with higher orders in q^2 giving finite corrections, such that the divergent term may be expressed (for an abelian theory such as QED) as:

$$\Pi(0) \simeq -\frac{\alpha}{3\pi}\frac{1}{\varepsilon} + \mathscr{O}(\varepsilon). \tag{2.18}$$

Since we eventually wish to take the limit $\varepsilon \to 0$ in order to properly evaluate our original integral, the latter terms will be seen to vanish in this limit. With this result, it becomes possible to calculate the (leading order) "running" (variation with scale) of the electromagnetic coupling, whilst eliminating the divergences that previously plagued the theory. This is readily seen by noting that the photon propagator, G_0, may be renormalised by considering additions to the ordinary amplitude

from those of photon lines, corrected by the loop self corrections π (as we have calculated above) applied successively, $G_0 \to G = G_0 + G_0\pi\, G_0 + G_0\pi\, G_0\pi\, G_0 + ...$

For example, the term $G_0\pi G_0$ would correspond to the single loop photon correction diagram on the left side of Fig.2.3, with the latter terms representing incrementally more fermion loops on the photon line. Then, by adopting knowledge of the fact that the longitudinal contributions vanish due to gauge invariance [52], this series may be summed by the expression:

$$G = G_0 \frac{1}{1-\Pi(q^2)}. \tag{2.19}$$

In essence, since $G_0 \sim e_0^2/q^2$, this expression may be used to determine the renormalisation scaling relation for the electromagnetic coupling:

$$e_0^2 \to \frac{e_0^2}{1-\Pi(q^2)} \simeq \frac{e_0^2}{1-\Pi(0)} \frac{1}{1-[\Pi(q^2)-\Pi(0)]+\mathscr{O}(\alpha^2)}. \tag{2.20}$$

The first fraction represents the renormalised coupling e^2 which, using the relation given above, allows us to determine that $Z_3 \simeq 1+\Pi(0) = 1-\frac{\alpha}{3\pi}\frac{1}{\varepsilon}$. In general, the numerator and denominator of the leftmost fraction on the RHS in Eq. (2.20) are defined to yield a finite, physically observable e, the renormalised coupling in QED, while the rightmost fraction on the RHS describes how the renormalised coupling e obtains scaling with q^2. In the limit $q^2 \gg m_e$ (the mass of the fermion in consideration, typically considered as an electron) from Eqs. (2.17) and (2.18) one obtains, $\Pi(q^2)-\Pi(0) \simeq \frac{\alpha}{3\pi}\ln\frac{q^2}{m^2}$ (the details of which are given in [52]), which gives the LO expression for the running of the electromagnetic coupling in QED:

$$\alpha(q^2) = \frac{\alpha}{1-\frac{\alpha}{3\pi}\ln\frac{q^2}{m^2}}. \tag{2.21}$$

While the exact results vary depending on the gauge theory being considered (and the choice of renormalisation procedure in some instances), in general, gauge couplings in the SM acquire scale dependence in line with the form of the Callan-

Symanzik [53][54] equation:

$$Q\frac{\partial g}{\partial Q} = \beta(g). \tag{2.22}$$

The functions $\beta(g)$ then determine the form of scale variation, and play a strong role in determining the nature of the gauge forces. Omitting the details, much of the resultant behaviour is determined by the two cases $\beta > 0$ and $\beta < 0$. The former is true for QED (where using Eq. (2.21), one determines at LO $\beta_{QED} = 2\alpha^2/3\pi > 0$), such that the effective electromagnetic and weak couplings after symmetry breaking, at low scales, are small $\alpha_{e,W} \ll 1$ and perturbation theory produces sensible results.

We note that historically, α denotes the redefined coupling strength for QED and α_S that for QCD, a notation adopted for the remainder of this thesis. Due the small electroweak values for α at low scales, the leptons may propagate freely and their interpretation as individual particles corresponds with the results from experimental measurements. While $\beta > 1$ implies that at high scales these couplings (such as the expression in Eq. (2.21)) grow without constraint and eventually violate the unitarity constraints of the theory, the point at which this happens, the Landau pole, occurs at scales much greater than the Plank mass $Q^2 \gg m_P$. As mentioned in the introduction, one is almost certain that the SM should be supplemented long before considering such scales.

In the case of QCD, unlike QED, more scaling constants must be considered than solely Z_3, corresponding to the additional vertices present in the theory, represented by the middle and rightmost diagrams of Fig. 2.2. After applying the procedure of renormalisation for an $SU(3)$ gauge group, one finds:

$$\beta(\alpha_S) = -\left(11 - \frac{8}{3} - \frac{2n_F}{3}\right)\frac{\alpha_s^2}{2\pi}, \tag{2.23}$$

where n_F denotes the number of interacting flavours (quarks) in the theory. Only six quark flavours are known, and for $n_F < 16$ one finds that in QCD $\beta < 0$ [55][56]. It is this, coupled with the fact that its bosons are massless, that distinguishes the behaviour of QCD from the other forces. In particular, the coupling in QCD dimin-

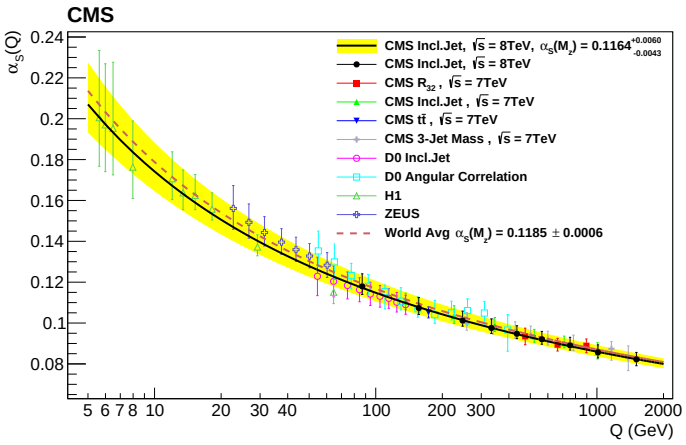

Figure 2.4: The strong coupling $\alpha_S(Q)$ (solid line) and its total uncertainty (band) as determined in [57] by the CMS Collaboration.

ishes at higher scales, such that $\alpha_S(Q^2) \to 0$, $Q^2 \to \infty$, and the quarks and gluons decouple, a condition known as asymptotic freedom.

At low energies however, $\alpha_S(Q^2) \gtrsim 1$ and the perturbative nature of the calculations in QFT no longer yield sensible results as one approaches the vacuum states of the theory. In fact, the interaction strength between coloured particles is of such a high magnitude that unlike the leptons, they coalesce into colourless combinations of particles known as hadrons. This phenomenon is known as confinement, a terminology which reflects the fact that when trying to disassociate the quarks within hadrons from one another, the energy of the incoming probe generates net-colourless combinations of particles from the vacuum which then arrange into more hadrons (a process called hadronisation) i.e. quarks are always confined in hadrons. The proton is such a hadron consisting primarily of the quark combination *uud*.

As shown in Fig. 2.4, many experimental results for processes sensitive to QCD are used in combination to obtain the scale variation for $\alpha_S(Q^2)$. Some experiments are sensitive to $\alpha(Q^2)$ at a given scale, while others provided a range of data points across many values for Q^2. The decrease in the coupling at higher scales is clearly visible, indicating the presence of asymptotic freedom as $Q^2 \to \infty$, and confinement at low scales.

It is useful to note that at LO in QCD, the scale dependence of α_S adopts the

following form:

$$\alpha_S(Q^2) \simeq \frac{4\pi}{\left(11 - \frac{2n_F}{3}\right)\ln\left(Q^2/\Lambda^2_{QCD}\right)}, \tag{2.24}$$

where the parameter $\Lambda_{QCD} \sim 200$ MeV is the approximate energy scale at which the quarks hadronise (and reflects the parameter dependence mentioned above for renormalisable theories).

It is precisely because the quarks and gluons are bound within hadrons, that phenomenological models must be developed in order to make predictions about scattering experiments that involve hadrons, such as those at the LHC. In the next chapter, the model of hadrons is reviewed from a context in which we begin with fewer assumptions about their internal structure (since historically the presence of quarks was stipulated as an explanation for hadron structure). This is in order to motivate a discussion about scattering experiments and how such models, supplemented with QCD, give rise to the Parton Distribution Functions (PDFs). We also discuss the conditions under which the distributions are suitably descriptive and how they may be related at different energy scales, Q^2.

Chapter 3

QCD and DIS

3.1 A Model of Hadrons

Historically, the existence of quarks was preceded by the observations of hadrons. The most commonly observed, with which this thesis is primarily concerned, are the proton and neutron, which comprise the nuclei of the chemical elements. Since they were found to interact strongly relative to the electromagnetic force within nuclei (which would later be shown to be an emergent property of their QCD interactions), with a strength independent of their electric charges, the protons and neutrons were associated in the same category of particles as the pions and other such hadrons discovered in the early 20th century whose interactions were observed to be similar (though the pion was originally posited to be the carrier of strong force interactions within the nucleus [58]).

The primary theme of the investigation of hadrons was concerned with the nature of their interactions with one another (decays and scattering processes), in which certain symmetries were observed. In particular, the proton and neutron were well related to one another by a property known as "isospin", an effective $SU(2)$ symmetry that predicted the rate of interactions between the Δ baryons, protons, neutrons and the pions, π^0, $\pi^{\pm}$. In addition to this, the property of "strangeness" was conceived of (extending the $SU(2)$ symmetry of isospin to $SU(3)$) to accommodate the observed interactions between the K and Σ baryons, which also led to the prediction of the Ω^- baryon in 1962, two years before its experimental observation

[59].

To explain the quantum numbers associated with these symmetries, it was conceived of that hadrons were in fact comprised of more fundamental constituent particles [60, 61], where Gell-Mann's terminology of "quarks" was adopted as the label. The quarks, it was hypothesised, were spin ½ particles which made up the baryons and mesons in triplets and quark-antiquark pairs respectively, where every component of the symmetry associated with hadronic interactions was associated with a distinct flavour of quark. The quarks would then interact identically in their strong force interactions, but with each flavour having a distinct mass (a property of strangeness that predicted the observed mass of the Ω^-).

That this model held true [62] was determined primarily from lepton-probe scattering events at high energy with hadrons [63]. In particular, much like the α scattering experiments of Rutherford determined that the scattering of a probe with the structure of the atom was best modelled from a small, concentrated charge, which led to the determination of the nuclear model of the atom, similarly, the inelastic scattering of leptons from scattering events that disassociated (i.e. led to hadronisation of) the proton were found to be consistent with scattering from point-like spin ½ particles, consistent with the quark model.

In addition to this picture, in the following section and the next chapter, it will be demonstrated that corrections from QCD and QED necessarily lead to the need to introduce the gluons and photons as constituents of the hadrons, alongside the quarks.

3.2 Deep Inelastic Scattering

Experiments that involve a lepton probe interacting inelastically with hadrons, at scales where the effects of the quark-parton model are resolvable, are known as Deep Inelastic Scattering (DIS). In order to discuss, quantitatively, how the results of such experiments motivate the quark model and the subsequent corrections that arise from QCD, we first lay out the dynamics and kinematic quantities associated with DIS events, i.e. inelastic lepton-hadron scattering, $lH \to l'X$. The lepton

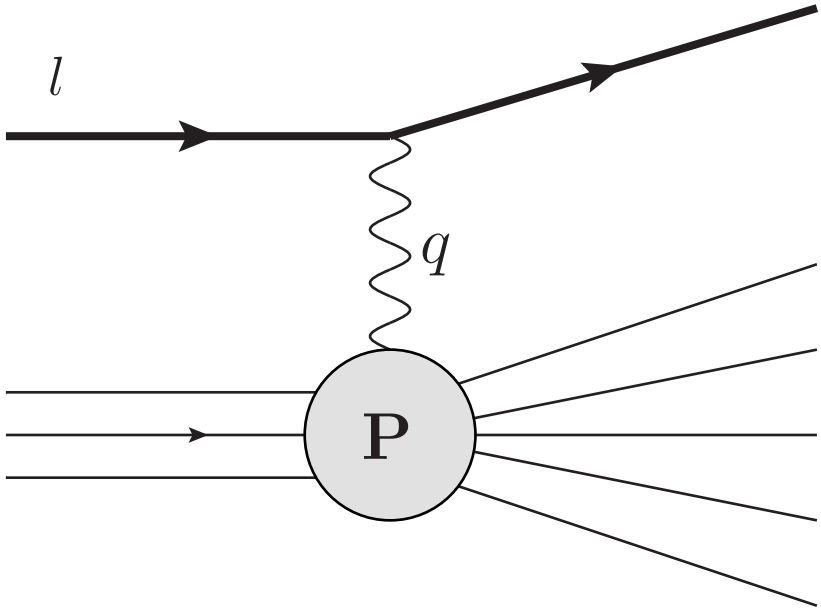

Figure 3.1: The primary (Leading Order) representation of a Deep Inelastic Scattering event, where the incoming (upper left) lepton interacts via $\gamma/W^{\pm}/Z$ exchange with a hadron (here represented by a proton). In the case of $W^{\pm}$ exchange, an incoming charged lepton is converted into the corresponding neutrino flavour ν_l or vice versa for an incoming neutrino probe. The outgoing products of the proton in DIS (bottom right) will be a jet of lighter hadrons, whose kinematics (W^2) is described in the text.

may be charged (typically an electron or occasionally a μ, since the τ decays on timescales that prohibits its acceleration through conventionally practical means) or a neutrino. We illustrate the leading order representation of such an event in Fig. 3.1.

The incoming lepton probe is denoted with four momentum k, the outgoing lepton with k', the incoming hadron (henceforth referred to explicitly as a proton) with P ($P^2 = m_p^2$, the proton mass squared) and the exchanged boson carries $q = k - k'$ from the lepton to the proton. It is useful to introduce several relativistically invariant quantities associated with the event. :

- $\nu \equiv q \cdot P/m_p = (E - E')$ is proportional to the loss of energy of the lepton in the rest frame of the proton.

- $Q^2 \equiv -q^2 = 2k \cdot k' = 2EE'(1 - \cos\theta)$, where both lepton masses have been neglected, for reasons given below. Note that $Q^2 > 0$, and for a DIS event

$Q^2 \gtrsim 1$ GeV^2 for a process capable of interacting with individual quarks and hence disassociating the proton, as discussed in the rest of the chapter.

- $W^2 \equiv (P+q)^2 \equiv m_X^2$ is the invariant mass squared of the entire recoiling hadronic system (X) produced from the event (the lower right side of Fig. 3.1).

- $x \equiv Q^2/2m_p\nu$, a dimensionless variable (that is definitionally $0 < x < 1$), which we shall see comes to represent the longitudinal fraction of the proton's momentum carried by a particular parton under consideration.

- $s \equiv (k+P)^2$, the total invariant mass squared of the system (the incoming lepton and proton). Also referred to as the Centre-of-Mass (CoM) energy.

- $y \equiv q \cdot P / k \cdot P = \nu/E$ is known as the "inelasticity". In the rest frame of the proton, y represents the fractional energy lost by the lepton probe during the scattering.

As alluded to above, for a typical DIS event $Q^2 \gg \Lambda^2_{QCD}$, such that the dynamics of the scattering process occurs on a "harder" scale (and therefore shorter timescale) than the process of QCD interactions within the proton or subsequent hadronisation. This will prove to be of central importance when introducing the notion of factorisation.

We shall formulate the relevant cross section for the process, heuristically shown in Fig. 3.1, restricting our attention to the case of a pure QED (a neutral current without consideration of the Z weak neutral current) scattering with virtual photon γ^* exchange, though we note that the discussion may be extended in an appropriate way to consider both unpolarised neutral current (NC) and weak current (CC for charged current, since the W boson intermediary carries electromagnetic charge) scattering events [65] (where the treatment of polarised scattering requires a substantially different treatment, not considered in this thesis).

At LO in QED, (as represented in Fig. 3.1) the matrix element associated with

the scattering is:

$$\mathscr{M} = (ie)^2 \bar{u}(k')\gamma^\mu u(k) \frac{-g_{\mu\nu}}{q^2} \langle X| J^\nu |H(P)\rangle , \tag{3.1}$$

where we use the index H to denote the proton wavefunction to distinguish it from its four momentum P and e is used to represent the electromagnetic coupling strength at each vertex. J^ν meanwhile represents the photon current which probes with the proton. The differential cross section $d\sigma$ (whose expression is provided below) is proportional to $|\mathscr{M}|^2$. In squaring this amplitude, we may separate the contribution into a leptonic (L) and hadronic (W) tensor:

$$|\mathscr{M}|^2 \propto L_{\mu\nu} W^{\mu\nu}, \tag{3.2}$$

where we are implicitly assuming that the sum over all lepton spins, $\sum_{spins}$ has been applied such that the cross section is unpolarised. Since the lepton lines of the amplitude in Eq. (3.1) are provided by the standard spinor algebra of field theory, some straightforward algebra yields an expression for the leptonic tensor:

$$L_{\mu\nu} = 4e^2(k_\mu k'_\nu + k_\nu k'_\mu - g_{\mu\nu} k \cdot k'). \tag{3.3}$$

Without any assumption about the internal nature of the proton and summing over all possible proton final states, $\sum_X |X\rangle \langle X| = 1$, the hadronic tensor (derived from the squaring of the amplitude given in Eq. (3.1) and defined in Eq. (3.2)) is simply expressed as:

$$W_{\mu\nu} = \frac{1}{4\pi} \int d^4x e^{iq\cdot x} \langle H(P)| [j_\mu(x), j_\nu(0)] |H(P)\rangle , \tag{3.4}$$

where an implicit sum over all proton spin states and all possible final state hadronic products X has also been performed. The evaluation of $W_{\mu\nu}$ would depend on the wavefunction $|H(P)\rangle$. We first introduce a parameterisation of $W_{\mu\nu}$ which uses only the considerations of the QED nature of the scattering process and Lorentz invariance to constrain its form, before discussing how the quark model of the proton

modifies this parameterisation and the difficulties (namely the non-perturbative nature of QCD at low scales) associated with an explicit evaluation of $W_{\mu\nu}$ in terms of quark and gluon states. This will be shown to prevent an explicit form from being calculable as in the case of the leptons (Eq. (3.3)).

Firstly, we note that since the nature of QED conserves electromagnetic currents ($\partial_\mu j_\mu^{QED} = 0$), one finds the lower vertex of Fig. 3.1 obeys $q^{\mu,\nu} W_{\mu\nu}(q,P) = 0$ (and likewise for the upper vertex, $L_{\mu\nu}(q,P)q^{\mu,\nu} = 0$). Under this constraint, the most general, Lorentz covariant form for the tensor under assumption of parity and charge conservation, may be expressed as:

$$\begin{aligned} W_{\mu\nu} &= \left(g_{\mu\nu} - \frac{q_\mu q_\nu}{q^2}\right) F_1(x,Q^2) \\ &+ \left(p_\mu + \frac{q_\mu}{2x}\right)\left(p_\nu + \frac{q_\nu}{2x}\right)\frac{1}{p\cdot q} F_2(x,Q^2)\left[1 + \mathscr{O}(\frac{m_p^2}{Q^2})\right]. \end{aligned} \tag{3.5}$$

The functions introduced in this expression, $F_1(x,Q^2)$ and $F_2(x,Q^2)$, are called the structure functions, and are representations of the internal structure of the hadrons (generally, since such functions also serve as descriptions for the neutron) and their determination is a central focus of DIS experiments. Their dependence on the incoming proton and lepton momenta (P and k) are implicit in the variables x and Q^2. In weak scattering processes, that do not necessarily obey the same parity and charge conservation, a third such structure function is also present, $F_3(x,Q^2)$. In deriving the above expression, the terms related to the lepton mass $\mathscr{O}(m_l^2/Q^2)$ have been neglected since at the scales considered, the lepton mass is substantially smaller than the energy scales being probed. Corrections related to the proton mass will be explored in later chapters.

A final general observation is that if one chooses to parameterise the structure functions in terms of the polarisation of the incoming photon, one may instead express the structure functions in terms of longitudinal and transversely polarised scattering. Omitting some of the details, one finds that the longitudinal component relates to the structure functions given in Eq. (3.5) by the relation $F_L = F_2 - 2xF_1$. In the naïve Quark-Parton model, one may determine (as shown below) that $F_2 = 2xF_1$

and the longitudinal component disappears, known as the Callan-Gross relation. However, corrections from QCD give non-zero contributions to F_L, and indeed it shall be seen to play a role, albeit restricted in its contributions, in the determination of the photon PDF (Chapter 5).

In conjunction with the leptonic tensor given in Eq. (3.3), one may use the standard expression for a differential cross section, $d\sigma$ to obtain the LO expression for pure photon exchange DIS scattering:

$$\frac{d^2\sigma}{dxdQ^2} = \frac{4\pi\alpha}{Q^4}\left[[1+(1-y)^2]F_1(x,Q^2) + \frac{1-y}{x}F_2(x,Q^2)\right], \tag{3.6}$$

where the latter term is seen to be small in experiments (as expected from the discussion above).

We now consider how one may relate this generalised perspective of DIS to the model of the hadrons constituted by quarks as well as the gluons that keep them confined to the hadrons as briefly outlined in Chapter 2.

The quark-parton model (QPM) assumes that the DIS proton scattering cross section is modelled simply as the sum of cross sections from the scattering of spin ½ quarks, as described above (though, in the following text, the term parton shall be used more generally to refer to any particle constituent of the proton). In the absence of QCD (where we merely consider the quarks as constituents of the hadron without any consideration of the nature of their confinement), we assume that the transversely polarised scattering occurs simply as the sum of many spin half particles, which in sum constitute the proton's full momentum along the direction of its propagation.

Implicit in this, is the assumption that we have integrated over any transverse momentum ($p_\perp$) carried by the quarks with respect to the direction of the total three-momentum of the proton. In principle, distributions provided as a function of the transverse momentum can be considered and are essential when determining the spin distributions of the quarks and other partons within the proton (and the reader is referred to section 19.6 of [65] for a brief overview). However, since the magnitude of the transverse momentum $p_\perp$ induces corrections of $\mathcal{O}(\Lambda^2_{QCD}/Q^2)$,

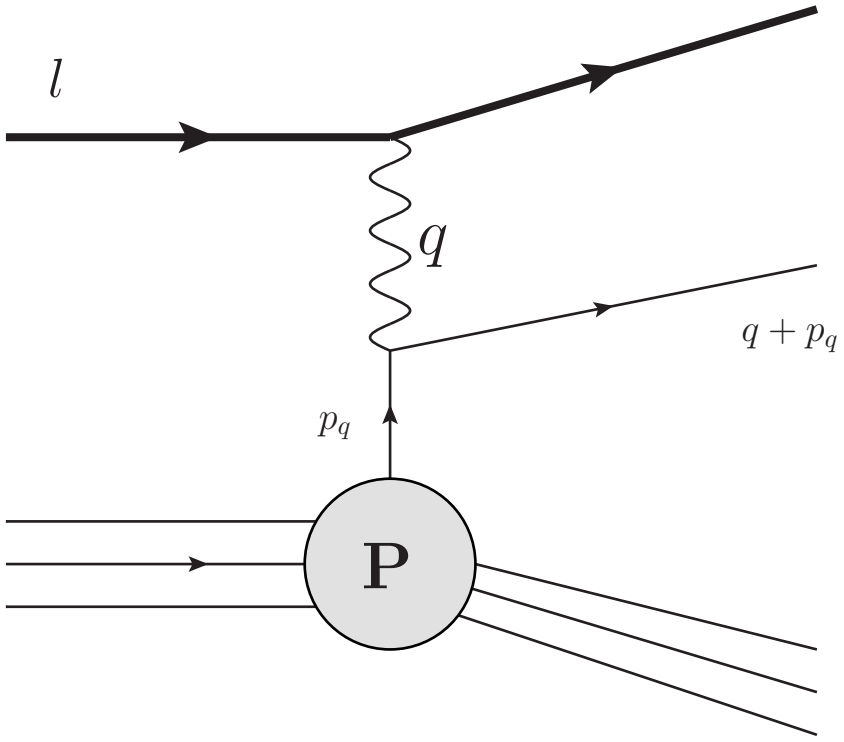

Figure 3.2: DIS represented in the case of the photon probe interacting with an isolated quark from within the proton.

they are therefore negligible in the kinematic limits being considered and irrelevant to our purposes.

In the case outlined above, the scattering of the photon occurs with one of the quarks within the proton (an assumption elaborated on in the next section), as shown in Fig. 3.2. From this figure, we may infer that the momentum of the quark with which the photon interacts carries a fraction, ξ of the total momentum of the proton, $p_q = \xi P$. Using the invariant mass relation of the quark, we find:

$$m_q^2 = (p_q + q)^2 \simeq 2\xi P \cdot q - Q^2 = \frac{Q^2}{x}\xi - Q^2 \simeq 0. \tag{3.7}$$

In the limit of massless quarks, $Q^2 \gg m_q^2$, known as the Bjorken limit, the variable x is associated with the fractional longitudinal momentum of the proton $\xi \simeq x$. This approximation holds to a very good degree of accuracy for DIS events and higher scales, and we shall make extensive use of it throughout this thesis (and will often refer to x in context as simply momentum).

In this instance outlined above, by considering that the scattering of the photon occurs with a spin ½ fermion line, the structure functions are related to the longitudinal momentum distribution of the quarks $f_q(x)$, the probability to scatter of a particular flavour of quark q carrying momentum fraction x, by the following relation [66]:

$$F_2(x,Q^2) = 2xF_1(x,Q^2) = \sum_{q,\bar{q}} e_q^2 x f_q(x). \tag{3.8}$$

Note that this is approximately sensitive to the total (charge-weighted) sum of quark and anti-quark distributions for a given value of x, a feature that makes it one of many processes valuable for the determination of the individual parton distribution functions $f_q(x)$. However, although Eq. (3.8) holds to a crude approximation, we shall see that in the process of incorporating the predictions of QCD, the $f_q(x)$ are themselves renormalised, obtaining a dependence on Q^2, as explored in the next section.

3.3 QCD and Parton Distribution Functions

In our discussion of QCD, we stated that its non-perturbative nature was manifest at lower scales ($\Lambda_{QCD} \simeq 200$ MeV), but that the quarks experienced so called asymptotic freedom at higher scales ($Q^2 \gg \Lambda_{QCD}^2$). Therefore, although one anticipates difficulty in explicitly calculating $W_{\mu\nu}$ from field theory at lower scales, one might assume that this tensor may be calculated in the high energy limit. In practice, $W_{\mu\nu}$ is dependent on the proton wavefunction $|H(P)\rangle$, whose momentum satisfies $P^2 = m_p^2$, and is therefore inherently dependent on the nature of the quarks at low energies.

Therefore, at all scales, one requires a means of separating the calculable, perturbative nature of QCD from the (presently) incalculable nature of QCD at the lowest scales, even when interpreting hadron scattering events at high energies. In order to do this, one needs to adopt a factorisation theorem. The assumption in general terms, is that the "hard" scattering process (the vertex involving the photon and the quark in Fig. 3.2), occurs on a timescale, $\mathcal{O}(1/Q)$, which is much shorter than the "soft" scale at which the effects of QCD occur $\mathcal{O}(1/\Lambda_{QCD})$, both in the internal

structure of the proton amongst the partons prior to scattering and in the subsequent hadronisation of the proton remnants. Therefore, the dynamics of the hard process can heuristically be interpreted as being independent of the soft physics of low scale QCD.

While the calculation of the proton wavefunction itself may not be performed perturbatively, the factorisation of the hard scattering process from the non-perturbative factor (which we shall show may be absorbed into the definition of the parton distribution functions) has been proven up to corrections of $\mathcal{O}(\Lambda^2_{QCD}/Q^2)$ [67]. Furthermore, it may also be shown that the non-perturbatively factored component in such events (DIS) may also be related to the non-perturbative elements of hadron-hadron scattering at high scales, such as those that occur at the LHC.

In essence, under the assumption of the factorisation theorem, one may consider the outgoing wavefunction of the proton $|X\rangle$ as a factorised wavefunction of an on shell "parton" (either a quark or antiquark) with momentum $\tilde{k}$ and the remnants of the proton X', $|X\rangle \to \left|q_i(\tilde{k})\right\rangle |X'\rangle$, where the index i denotes the flavour of (anti-)quark under consideration. This allows one to obtain the relationship in Eq. (3.8).

The salient result of the factorisation theorem is that at all orders in QCD, the structure functions (F_1 and F_2) may be calculated by separating the dynamics of the hard process, from the PDFs (into which we absorb by definition the non-perturbative phenomena associated with scales at $Q^2 \sim m_p^2$). Using the notation $(f \otimes g)(x) = \int_x^1 \frac{dy}{y} f\left(\frac{x}{y}\right) g(y)$, we may express this as:

$$F(x,Q^2) = \sum_{i=q,\bar{q},g} C_i(x,Q^2) \otimes f_i(x). \tag{3.9}$$

The $C_i(x,Q^2)$ are known as the Wilson coefficients (or simply, coefficient functions) and carry the high Q^2 scale information of the process, and are calculable in perturbative QCD:

$$C_i(x,Q^2) = C_i^{(0)}(x,Q^2) + \frac{\alpha_S(Q^2)}{2\pi} C_i^{(1)}(x,Q^2) + \frac{(\alpha_S(Q^2))^2}{(2\pi)^2} C_i^{(2)}(x,Q^2) + \ldots \tag{3.10}$$

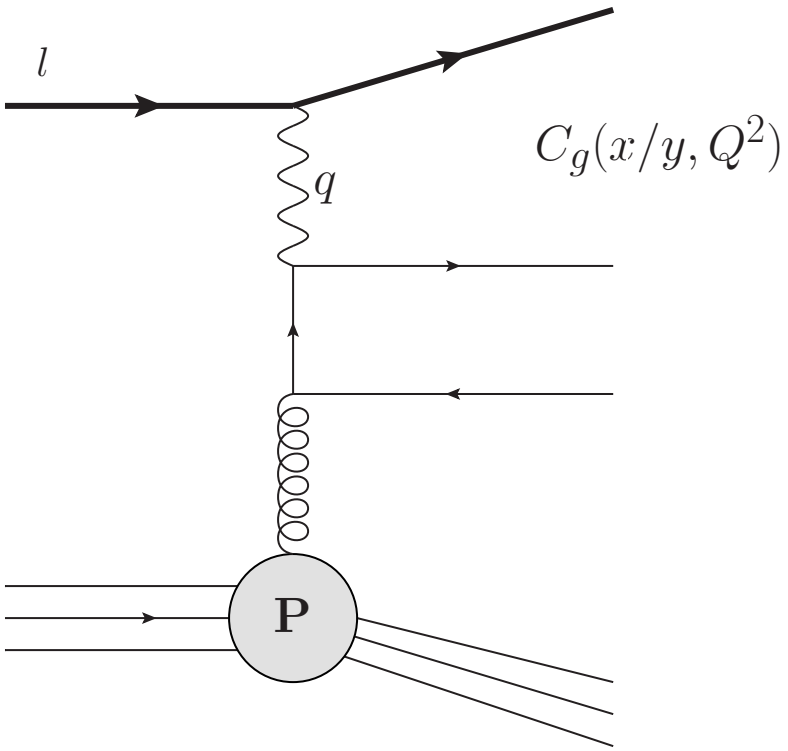

Figure 3.3: DIS represented in the case of the photon probe interacting with a gluon, by mediation of an emitted quark line.

However, there is one further step needed in relating these function to observable cross sections, associated with the regularisation of these functions in field theory. Beyond LO, coefficient functions are susceptible to divergences at low Q^2 (known as infrared divergences), a consequence of naïvely extending the results of QCD to low energies (while ultraviolet, high Q^2 divergences are handled with methods such as dimensional regularisation, as outlined in the previous chapter).

To resolve this, an infrared cutoff is introduced into both the Wilson coefficients and, crucially, into the definition of the PDFs themselves, $f_i(x) \to f_i(x, \mu_F^2)$ where μ_F is the factorisation scale, an arbitrary scale adopted to regularise both the coefficient functions and the PDFs. In adopting this procedure (elaborated in [64]), the "bare" quark distributions (the unrenormalised distributions discussed above) may themselves be renormalised, by considering QCD processes at higher orders. It is in this manner that partons such as the gluons may also be considered hard scattering objects within the proton, as illustrated in Fig. 3.3 . For the quarks, after renormalisation, the measurable (as discussed in the next chapter) PDFs are related

to the bare distributions, $f_q^{(0)}(x)$ by:

$$f_q(x,\mu_F^2) = f_q^{(0)}(x) + \frac{\alpha_S(\mu_F^2)}{2\pi}\int_x^1 \frac{d\xi}{\xi} f_q^{(0)}(\xi) P_{qq}\left(\frac{x}{\xi}\right)\ln\frac{Q^2}{\mu^2} + ..., \tag{3.11}$$

where for $\mu < \mu_F$, the low scale dynamics are absorbed into the PDFs to create a finite, observable distribution. The function P_{qq} will be of particular significance, as explained in the next section. We conclude this section, by noting that while Eq. (3.9) indicates that the structure functions are calculable in terms of the PDFs, the measurements of DIS are in principle used in the opposite fashion; the measured differential DIS cross section in x and Q^2 is used to constrain the PDFs themselves.

Although this prevents an a-priori determination of the structure functions from theory, a property of the factorisation theorem, mentioned above, makes this a powerful observation for phenomenological purposes. The distribution measured in one process, such as neutral current weak scattering, is readily related to the same distribution in another process sensitive to the internal structure of the proton, such as charged weak boson scattering. The enormous advantage afforded by the universality of the PDFs in distinct scattering processes is that the precision measurements that constrain the PDFs in certain DIS experiments (discussed in greater detail in the next chapter) allows us to establish a well determined set of distributions that we may apply when calculating hard cross sections in proton-proton scattering, outside of the setting of DIS.

Specifically, the total cross section, σ may be considered as simply the hard cross section, $\hat{\sigma}$ between two colliding partons (such as quark-quark collisions in the instance of Drell-Yan production, illustrated in Fig. 3.4), integrated over the PDFs, whose momenta distributions determine the likelihood for a hard scattering at a given scale Q^2 (along with centre of mass energy of the protons). For a final state X, produced from two incoming beams of protons A and B, this is summarised in the following equation:

$$\sigma_{AB} = \sum_{i,j\in q,\bar{q},g}\int dx_A dx_B f_i(x_A) f_j(x_B)\hat{\sigma}_{ij\to X}, \tag{3.12}$$

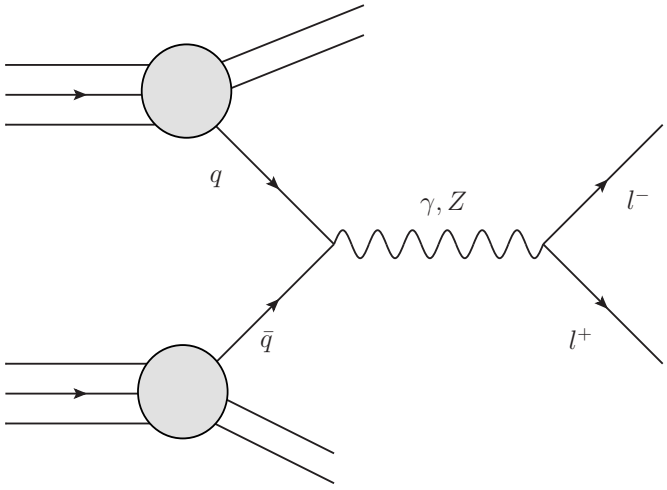

Figure 3.4: Drell-Yan (di-lepton) production via quark-antiquark annihilation from proton-proton scattering. The central Feynman diagram consisting of both photon vertices, represents our hard process $\hat{\sigma}$ while the distribution of the quarks (summed over any relevant flavours) is information encoded in the PDFs.

where the f_i are the PDFs for the relevant incoming partons, which may be experimentally determined from previous experiments.

3.4 DGLAP

As mentioned in the previous chapter, observable quantities typically acquire scale dependence after renormalisation. The PDFs are also subject to this variation in scale, as evidenced in Eq. (3.11). However this expression is dependent on several bare quantities (such as $f_q^{(0)}$) from which we cannot calculate observable parameters (hence the initial need for renormalisation). Therefore it is convenient to consider the PDFs at a given scale and formulate a means of relating the distributions at one scale to another (referred to as the PDF's "evolution"), in the form of a differential equation. This is more generally known as the renormalisation group equation, and for the PDFs one may obtain this relation by differentiating Eq. (3.11) with respect to $\ln \mu_F^2$, to obtain:

$$\mu_F^2 \frac{\partial}{\partial \mu_F^2} f_q(x, \mu_F^2) = \frac{\alpha_S(\mu_R^2)}{2\pi} \int_x^1 \frac{dz}{z} P_{qq}\left(\frac{x}{z}, \alpha_S(\mu_R^2)\right) f_q(z, \mu_F^2). \tag{3.13}$$

This equation, known as the Dokshitzer-Gribov-Lipatov-Altarelli-Parisi [3, 4, 5] (DGLAP) equation, is of paramount importance in the study of PDFs. First, we note that μ_F is an arbitrarily low scale for the purposes of regularisation and that a separate scale μ_R is introduced, known as the renormalisation scale. In relating the PDFs to a given scale, provided we are consistent in our definition, any dimensionally appropriate kinematic quantity may be chosen when considering an observable scale for the process. The typical choice, adopted for the remainder of this thesis, is $\mu_F = \mu_R = Q$.

Since experiments that measure the PDFs at different values of x and Q^2 only provide limited information about the distributions at each region in phase space, by providing a means of relating the PDFs at one scale to another, once a given $f(x, Q_0^2)$ is determined at a given scale, the DGLAP equations may relate the distribution to higher (or in principle lower) scales, $Q^2 > Q_0^2$. As we shall see in the next section, this is crucial for determining the PDF distributions in global fits to data.

Here we elaborate on the role of the function $P_{qq}(x)$ (where we suppress the dependence on α_S in the notation). When introducing the notion of QCD to the parton model, one must account for higher order corrections in field theory to the fermion/boson lines and coupling vertices (as explored briefly in Chapter 2). In general, the functions P_{ij} encapsulate this behaviour with indices that now run over all flavours of (anti-)quark q and the gluon g (and as we shall see in Chapter 5, the γ in QED) and describe the dependency of the PDFs on the scale Q^2.

Heuristically, they may be considered as functions that "resolve" the higher scale behaviour of the partons, in which a quark line "splits" to comprise a quark and gluon. In fact, there are many such splittings possible, though at leading order, the possible splittings correspond identically to the diagrams (including possible rotations) given in Fig. 2.2 of the proceeding chapter.

Therefore, the more general form of the DGLAP equations, adopting the $\otimes$ convolution notation introduced in the preceding section and $t \equiv \ln Q^2$, is:

$$\frac{\partial f_i}{\partial t} = \sum_{j=q_f,\bar{q}_f,g} P_{ij} \otimes f_j, \tag{3.14}$$

where the sum runs over all appropriate flavours of quark, antiquark and gluon. Henceforth, we shall refer to the PDF for a given parton, simply using the notation for the relevant parton, e.g. $f_q(x,Q^2) \to q(x,Q^2)$. Typically, the splitting functions are calculated to a given order in QCD, which for a consistently renormalised definition of a total cross section (e.g. Eq. (3.12)), should match the order in which the hard process is calculated. The leading order expressions for the quark splitting functions are given below:

$$P_{qq} = C_F \left[\frac{1+x^2}{(1-x)_+} + \frac{3}{2}\delta(1-x) \right], \tag{3.15}$$

$$P_{qg} = T_R \left[x^2 + (1-x)^2 \right], \tag{3.16}$$

$$P_{gg} = 2C_A \left[\frac{x}{(1-x)_+} + \frac{1-x}{x} + x(1-x) \right] + \left(\frac{11}{6}C_A - \frac{4}{6}n_F T_R \right) \delta(1-x), \tag{3.17}$$

$$P_{gq} = C_F \left[\frac{1+(1-x)^2}{x} \right], \tag{3.18}$$

where $C_F = 4/3$, $C_A = 3$ and $T_R = 1/2$ are factors associated with the $SU(3)$ algebra of QCD and n_F the number of quarks whose mass obeys the condition $m_q > Q$ for the scale being considered and $\delta(x)$ a Dirac delta function. The subscript $+$ meanwhile, refers to a prescription commonly found in splitting functions, i.e. at NLO and NNLO in QCD:

$$\int_0^1 dx \frac{f(x)}{(1-x)_+} = \int_0^1 dx \frac{f(x)-f(1)}{1-x}. \tag{3.19}$$

In general, an inspection of the form of Eq. (3.14) shows that the evolution of the partons, $q, \bar{q}$ and g, in DGLAP are in fact coupled differential equations. That is, the splittings associated with a given distribution give rise to changes and contributions to other parton distributions and vice versa.

Furthermore, at higher orders, the splitting kernels are modified, simply by linearly adding the contributions from higher order splittings, such that the P_{ij} (such

as P_{qj} in Eq. (3.14)) are extended in the following manner:

$$P_{ij} = \frac{\alpha_S}{2\pi} P_{ij}^{(1)} + (\frac{\alpha_S}{2\pi})^2 P_{ij}^{(2)} + (\frac{\alpha_S}{2\pi})^3 P_{ij}^{(3)} + ... \tag{3.20}$$

where in this instance the superscript denotes the order in QCD. When introducing QED, we shall find that Eq. (3.20) is extended in a virtually identical manner, with the processes that determine the splitting kernels being those of QED, or mixed order (with internal lines that contain both photons and gluons).

Since the PDFs denote the fractional momenta distributions carried by each flavour of parton, their evolution should be subject to the constraint that integration of their sum should yield 1. In fact, the splittings are naturally seen to observe the so called momentum sum rule. Introducing the notation $\Sigma = \sum_{i=u,d,s,c,b} q_i(x,Q^2) + \bar{q}_i(x,Q^2)$, we obtain:

$$\int_0^1 x(\Sigma(x,Q_0^2) + g(x,Q_0^2)) = 1. \tag{3.21}$$

In later chapters, we shall see how this equation is modified upon the inclusion of the effects of target mass corrections, higher twist contributions, QED and more specifically the inclusion of the photon distribution. In the next chapter, we cover in more detail how the PDFs themselves, $f(x,Q^2)$, are determined from experimental measurements and their uncertainties produced.

Lastly, superseding the notion of isospin, the flavour of the quarks and their content in the hadrons is seen to provide the necessary quantum numbers to explain the properties of the proton and neutron (under the assumption that the charges of the u and d quarks are $e_u = 2/3$ and $e_d = -1/3$, respectively, in units of the electron charge). Defining the "valence" distribution for a particular flavour as $q_V = q - \bar{q}$, and denoting the proton and neutron as (p) and (n) respectively, the PDFs are subject to the exact constraint:

$$\begin{aligned} \int_0^1 u_{V,(p)}(x)\mathrm{d}x &= \int_0^1 d_{V,(n)}(x)\mathrm{d}x = 2, \\ \int_0^1 d_{V,(p)}(x)\mathrm{d}x &= \int_0^1 u_{V,(n)}(x)\mathrm{d}x = 1, \end{aligned} \tag{3.22}$$

known as the flavour sum rules. The nature of the valence distributions between the proton and neutron is explored more thoroughly, with the added consideration of the effects of QED, in Chapter 7.

Chapter 4

Parton Distribution Functions

Having introduced the Parton Distribution Functions (PDFs) in the context of DIS scattering and proton-proton collisions, we now look to how one determines the PDFs from empirical observations, separated by their flavours, and how their uncertainties are calculated, in the framework of pure QCD splitting kernels. In this chapter, and for the remainder of the thesis, we shall restrict our attention to unpolarised PDFs.

4.1 The Determination of PDFs

As mentioned in the previous chapter, the ability to express the cross sections for DIS and other scattering events in terms of their explicit dependence on the PDFs, such as in Eqs. (3.9) and (3.12), allows one to determine their values, $f(x,Q^2)$, at given regions in x and Q^2. Furthermore, the universality of the PDFs related by different scattering processes yields multiple constraints on the same distributions, improving the accuracy of their determination.

Typically, one considers the u,d,s,c and b flavour quark (q) and antiquark ($\bar{q}$) distributions within the proton, where the top, t, is generally excluded at the centre of mass collision energies considered here. This is because its large mass ($m_t^2 >> m_p^2$) generally prohibits its production through splitting kernels from the gluon $g \to gt$ (the only QCD sensitive parton capable of generating a top distribution at LO), though some studies [68, 69, 70] have investigated the phenomenology associated with its presence at large centre of masses, such as those of potential future colliders

Process	Subprocess	Partons	x range
$l^{\pm}p,n \to l^{\pm}X$	$\gamma^* q \to q$	$q,\bar{q},g$	$x \gtrsim 0.01$
$l^{\pm}n/p \to l^{\pm}X$	$\gamma^* d/u \to d/u$	d/u	$x \gtrsim 0.01$
$pp \to \mu^+\mu^- X$	$u\bar{u}, d\bar{d} \to \gamma^*$	$\bar{q}$	$0.015 \lesssim x \lesssim 0.35$
$pn/pp \to \mu^+\mu^- X$	$(u\bar{d})/(u\bar{u}) \to \gamma^*$	$\bar{d}/\bar{u}$	$0.015 \lesssim x \lesssim 0.35$
$\nu(\bar{\nu})N \to \mu^-(\mu^+)X$	$W^* q \to q'$	$q,\bar{q}$	$0.01 \lesssim x \lesssim 0.5$
$\nu N \to \mu^-\mu^+ X$	$W * s \to c$	s	$0.01 \lesssim x \lesssim 0.2$
$\bar{\nu}N \to \mu^+\mu^- X$	$W * \bar{s} \to \bar{c}$	$\bar{s}$	$0.01 \lesssim x \lesssim 0.2$
$e^{\pm}p \to e^{\pm}X$	$\gamma^* q \to q$	$g,q,\bar{q}$	$10^{-4} \lesssim x \lesssim 0.1$
$e^+p \to \bar{\nu}X$	$W^+\{d,s\} \to \{u,c\}$	d,s	$x \gtrsim 0.01$
$e^{\pm}p \to e^{\pm}c\bar{c}X, e^{\pm}b\bar{b}X$	$\gamma^* c \to c, \gamma^* g \to c\bar{c}$	c,b,g	$10^{-4} \lesssim x \lesssim 0.01$
$e^{\pm}p \to j+X$	$\gamma^* g \to q\bar{q}$	g	$0.01 \lesssim x \lesssim 0.1$
$p\bar{p}, pp \to j+X$	$gg, qg, qq \to 2j$	g,q	$0.00005 \lesssim x \lesssim 0.5$
$p\bar{p} \to (W^{\pm} \to l^{\pm}\nu)X$	$ud \to W^+, \bar{u}\bar{d} \to W^-$	$u,d,\bar{u},\bar{d}$	$x \gtrsim 0.05$
$pp \to (W^{\pm} \to l^{\pm}\nu)X$	$u\bar{d} \to W^+, d\bar{u} \to W^-$	$u,d,\bar{u},\bar{d},g$	$x \gtrsim 0.001$
$p\bar{p}(pp) \to (Z \to l^+l^-)X$	$uu, dd, ...(u\bar{u}, ...) \to Z$	$u,d,...(g)$	$x \gtrsim 0.001$
$pp \to W^-c, W^+\bar{c}$	$gs \to W^-c$	$s,\bar{s}$	$x \gtrsim 0.001$
$pp \to (\gamma^* \to l^+l^-)X$	$u\bar{u}, d\bar{d}, ... \to \gamma^*$	$\bar{q},g$	$x \gtrsim 10^{-5}$
$pp \to (\gamma^* \to l^+l^-)X$	$u\gamma, d\gamma, ... \to \gamma^*$	γ	$x \gtrsim 10^{-2}$
$pp \to b\bar{b}X, t\bar{t}X$	$gg\bar{b}, t\bar{t}$	g	$x \gtrsim 10^{-5}, 10^{-2}$
$pp \to$ exclusive $J/\psi, \Upsilon$	$\gamma^*(gg) \to J/\psi, \Upsilon$	g	$x \gtrsim 10^{-5}, 10^{-4}$
$pp \to \gamma X$	$gq \to \gamma q, g\bar{q} \to \gamma\bar{q}$	g	$x \gtrsim 0.005$

Table 4.1: A list of the processes (as outlined in [65]) whose experimental measurements have yielded constraints on the PDFs, provided with the flavour of parton and the approximate range in x that is constrained. The sub-process column describes the internal Feynman diagram that probes the partons. The upper, middle and lower segments of the table are categorised by fixed target, ep and hadron-hadron collider experiments, respectively. In this table, j indicates the production of a hadronic jet. Note that lepton production in proton-proton collisions provided (weak) constraints on the photon PDF, γ, whose role is discussed more prominently in subsequent chapters.

(e.g. $\sqrt{s} = 100$ TeV as proposed for a Future Circiular Collider).

In addition to the quarks, as mentioned previously, the gluon is also seen to enter scattering processes with its own associated PDF, $g(x,Q^2)$ and may be constrained from similar processes. In Table 4.1 (adapted from [65]) we outline the scattering processes that provide constraints to the PDFs, along with the partons they constrain and the range in x to which they display the most sensitivity.

This table is separated into three groups that provide broad categorisations of PDF sensitive scatterings: fixed target experiments (in which a probe impinges on a

target stationary nucleus, N, or individual nucleon in the lab frame), high energy electron-proton scattering in which both the lepton and hadrons are accelerated in the lab frame, as performed by the HERA experiment, and proton-anti-proton (Tevatron) or proton-proton scattering (LHC). At the time of writing, although only experiments of the latter kind continue to be performed at high luminosity, the data from HERA experiments (H1 and ZEUS) continues to provide some of the most sensitive constraints on the PDFs, due to the fact that the uncertainties on the data were low from a combination of high statistics and the ability to reconstruct final state hadronic jets (in contrast to fixed target experimental designs) and the kinematics of the outgoing lepton probe (unlike hadron-hadron colliders).

For a given data point from an experiment, while typically able to provide data for a given Q^2, the cross sections are sensitive to a convolution of the PDFs that involve an integral over a particular range in x, as indicated in Eqs. (3.9) and (3.12). While at LO, (i.e. neglecting the effects of QCD and assuming the QPM), one may suitably approximate the charge weighted sum of the PDFs as in Eq. (3.8), beyond leading order one cannot strictly associate them with a given point in x (that is, directly measure $f(x, Q^2)$ even indirectly) when considering scattering processes.

Furthermore, for the purposes of phenomenology, one often requires a continuous representation of the $f(x, Q^2)$ in both variables. Finally to reduce the uncertainty carried forward from experimental measurements to the PDFs themselves, we also require a way of constraining the distributions in a global comparison to the data, in order to best incorporate the information provided from it. This is of particular importance, since hadron collider phenomenology is often constricted by the uncertainties associated with PDFs [71].

The general methodology adopted by all major PDF sets (discussed in the next section) is as follows. First, as noted in the previous chapter, one only needs to determine the distributions at a given scale Q_0^2, which we shall call the input or starting scale, in order to relate them to higher (or lower) scales by "evolving" them via the DGLAP equation. This allows data from a range of Q^2 values to be incorporated into a single fit to all available data.

In order to provide a suitable representation of the PDFs in x space, one typically uses an ansatz solution in polynomial form. Parameterisations are often of the form $xf(x,Q_0^2) = x^a(P(x))(1-x)^b$, where the $a,b...$ represent free parameters that are fit by the data and $P(x)$ represents a family of polynomials. Typically, PDF sets use 14-28 such parameters (with the notable exception of NNPDF [72], discussed in the next section), whose values determine the form of the PDFs during a fit and whose tolerance to the data (i.e. the variation of the parameter values in a manner consistent with a fit to the data) determine the uncertainties associated with the PDFs. In the next section we will distinguish between two broad categorisations of PDF uncertainties defined by the "Hessian" and "Monte-Carlo" strategies.

Note that at input, the c and b quark and antiquark distributions are not typically included for starting scales $Q_0^2 < m_c^2, m_b^2$. This is because their production, such as from the gluon PDF at low scales, $g \to q\bar{q}$ at LO, is kinematically prohibited due to their masses (for which reason we shall refer to them as "heavy" flavours). Therefore, in many sets no parameterisation is provided for them, since their appearance during evolution is determined from the splitting from other PDFs and is therefore predicted from the determination of the other flavours. In doing so, one must adopt a scheme for incorporating the quark masses into the evolution (and coefficient functions for the purposes of comparison to data), which are discussed in the next section. One may in principle include a separate "intrinsic" component of the heavy flavour distributions, though investigation have shown that their magnitude is likely to be small and not well determined [73, 74].

Broadly speaking, the determination of the PDFs from fits to data, which we shall henceforth refer to simply as "fitting", is conducted in the following manner:

- Define ansatz distributions for the PDFs, $f_i(x,Q^2)$. These may be separated by flavour, though for practical purposes related to the nature of the splitting kernels $P_{ij}(x)$ used in DGLAP evolution, linear combinations of partons that fully span the space of flavours are often defined in ways that are efficient for numerical integration.

- Evolve the PDFs using DGLAP evolution (outlined in the previous chapter)

to produce values for the PDFs at given values for x and Q^2. Although a perfectly continuous representation is not numerically feasible, by defining the values at suitably densely spaced points in both variables, (typically logarithmically) one may then define interpolation routines that may provide values at a given numerical accuracy for $f(x, Q^2)$.

- Use the coefficient functions associated with various processes (as outlined in Table 4.1) $C_i(x, Q^2)$ or expressions for the differential cross sections $d\sigma$ to make predictions against data provided from experimental observations in the appropriate kinematic regions. The order to which the processes and differential cross sections are calculated are generally made to match the order to which the splitting kernels are calculated (as in Eq. (3.20)). This then defines the "order" of the PDFs (which are typically calculated at LO, NLO and NNLO in QCD).

- Calculate the χ^2 (which we shall give an explicit form for in Section 4.3) fit to the data for the given PDFs.

- Repeat the above steps for small variations of the PDF parameters in order to locally estimate $\partial\chi^2/\partial a_i$, where the a_i represent the free parameters in the fit (except in the case where an optimisation scheme is performed by alternative means, say a genetic algorithm, as covered in the next section).

- Use local information estimating the gradient of the χ^2 in order to minimise the χ^2, by the use of an appropriate optimisation scheme.

The parameters found to minimise the χ^2 are then adopted as the best fit values which then define the "central" curves for the PDFs at the input scale, and serve as the input distributions to DGLAP evolution to extend the PDFs into all ranges in Q^2. The uncertainties are then produced in a similar manner, where sufficient variation in fit, $\Delta\chi^2$, is used to define PDF uncertainties. Since each free parameter induces an independent component of uncertainty, a range of PDF uncertainty bands are calculated. Since the parameters may be correlated in the fit (as discussed in the next

section), one first diagonalises the covariance matrix associated with the parameter uncertainties in order to determine "eigenvector" directions within the parameter space for independent uncertainties. The final uncertainties are then calculated from a sum in quadrature of the independent uncertainty contributions.

Several groups have been involved in the determination of the PDFs using the method outlined above. In the next section we provide a brief overview of the most widely used sets, and the differences in their methodologies.

4.2 Overview of Modern Sets

The main distinguishing factors between modern PDF sets are the choice of data that are incorporated into the fit, the parameterisation of the input PDFs, the methods by which the DGLAP evolution and fit are performed and subsequently how error sets are produced. While PDF sets exist that focus on data available from a particular experiment or types of scattering process (restricting the fit to a subset of processes from Table 4.1), such as the HERAPDF [75], in this section we shall restrict our attention to the most widely used PDF sets that perform global fits (for a more relevant like-to-like comparison with the MMHT framework). Furthermore, many of these groups have provided sets with QED corrections, which shall be the focus of subsequent chapters.

In the following discussion, the broad details of the parameterisation, the "Hessian" approach to determining error sets based on polynomial form inputs will apply to the ABMP [76], CT [77] Collaboration and MMHT [78] collaboration sets. The notable exception is NNPDF [72], whose formulation based on a "Neural Network" approach we shall discuss separately, differing from other sets in their parameterisation, the form of producing error sets and the manner in which their DGLAP integration is performed.

First we outline the most common method for the parameterisation and the production of uncertainties for PDF sets. As mentioned in the previous section, a polynomial parameterisation is typically adopted with linear coefficients and certain exponents serving as free parameters of the fit. We shall provide a more specific

example in the next section. Each parameter, a_i, then serves as source of uncertainty, though not independently. As discussed in the previous section, during the fit one obtains a matrix of how the χ^2 changes as a function of varying the parameters and their correlations, known as the Hessian matrix $H_{ij} = 1/2(\partial^2\chi^2/\partial a_j \partial a_i)$.

It is by diagonalising the Hessian matrix that one may obtain the eigenvectors, consisting of linear combinations of the parameters a_i, that represent independent uncertainty contributions to the PDFs. We note that in the case of MMHT, while the PDFs have 36 free parameters in principle, practically speaking some parameters become very highly correlated in the fit, such that the diagonalisation procedure is numerically unstable. In particular, certain parameter combinations are seen to be very tightly and non-linearly constrained by the data, with negligible uncertainties (described by the tolerance condition below). In this case, a certain number of parameters, while left free in the initial fit, are fixed when producing the eigenvector uncertainties (such that there are 25, rather than 36 eigenvector directions).

The uncertainties on the PDFs are then obtained by creating a "tolerance" condition for the confidence interval, $T = \Delta\chi^2_{global}$, i.e. a variation in the "goodness of fit" (heuristically speaking) that encompasses a 1σ (68%) confidence limit. The standard parameter fitting criterion would yield $T = 1$ as the condition for a 1σ level uncertainty band. However, in practice, when fitting to many disparate datasets in tension with one another, one has to adopt a "dynamic" scheme (which we provide more details about in the next section), in which the tolerance, T, must be increased, $T > 1$ to provide sufficient variation in the fit to the data for a 68% confidence interval (typically in the region of $T \sim 3$). This then provides the magnitude by which the eigenvectors, e, (in the space of parameters with independent uncertainty contributions) must vary to produce the uncertainty bands. In particular, parameter displacements away from the best fit (the values seen to minimise the χ^2) values, a_i^0, may be expressed as:

$$a_i - a_i^0 = \sum_{k=1}^{n} e_{ik} z_k. \tag{4.1}$$

The z_k determine the magnitude of the variation from the best fit values in the parameters. The condition for variation within the tolerance (to generate uncertainty

PDF collaboration	Polynomial form	Number of free parameters
MMHT	Chebyshev	36
CT	Bernstein	28
ABMP	Generalised	25

Table 4.2: A list of the major Global fit PDF collaborations (excluding NNPDF whose parameterisation is distinct), the polynomial parameterisation form adopted in their fits and the number of free parameters in each. For the ABMP parameterisation, more details may be found in their paper [76]. Note that the number of parameters may differ between sets since the fit quality depends jointly on the form of the initial polynomial being fit, the number of free parameters, the data being fit to and the fitting procedures themselves, which differ as described in the main text to provide a suitable fit while avoiding over-fitting.

bands) is expressed simply as $\sum_{k=1}^{n} z_k^2 \leq T$. It is often more convenient to define this relation in terms of the parameters for the eigenvector pairs, $S_k^{\pm}$ (where the $\pm$ indicates that each parameter generates two eigenvector sets representing a positive and negative variation in the eigenvector space) that is, the values of the PDFs at the uncertainty bands defined by our tolerance scheme:

$$a_i(S_k^{\pm}) = a_i^0 \pm t e_{ik}, \tag{4.2}$$

where the t is adjusted to give the desired T (and in the approximation that the χ^2 is a quadratic function of the parameters a_i is simply $t \simeq T$, though this is not universally true in practice [79]).

The parameters themselves (with respect to the form of the input PDF parameterisation) are chosen by each group to provide suitable results after fitting, capable of providing sufficient variation to produce reasonable uncertainty sets in line with the data, without over-fitting. The exact form of polynomials chosen are typically done with respect to a particular kind of polynomial provided at a given order in x^n, whose details for each of the three sets presently discussed, we provide in Table 4.2.

4.2.1 NNPDF

The procedure of fitting, as described in the previous section, is an iterative process that involves changes in the input PDFs, ($Q^2 = Q_0^2 \sim m_p^2$), which are then related to the data by first evolving the input PDFs to all relevant regions in Q^2 via DGLAP

evolution and then calculating the appropriate cross sections for the process being considered. The former of these steps relies extensively on the convolution of the PDFs with the splitting kernels P_{ij}, as in Eq. (3.13). Since the PDFs are typically only defined by discrete points in x, an appropriate numerical scheme is needed to approximate this integration (which due to the relatively smooth nature of the PDFs, may be performed to a high degree of accuracy).

However, we note that in principle, the integration need not be performed in x space. Although the initial parameterisation is given in x space, one then may also transform the PDFs and splitting kernels into Mellin N space, defined by the following relations:

$$\begin{aligned} f(N,Q^2) &= \int_0^1 dx x^{N-1} f(x,Q^2), \\ \gamma_{ij}(N,Q^2) &= \int_0^1 dx x^{N-1} P_{ij}(x,\alpha(Q^2)), \end{aligned} \tag{4.3}$$

where the Mellin N space transformations of the splitting kernels γ_{ij} are known as the "anomalous dimensions".

In Mellin space, the DGLAP equations then resemble the form:

$$Q^2 \frac{\partial}{\partial Q^2} f_j(N,Q^2) = \frac{\alpha_S(Q^2)}{2\pi} \sum_i \gamma_{ji}(N,Q^2) f_i(N,Q^2). \tag{4.4}$$

Note that $\gamma_{ij}(N,Q^2)$ is not, as evidenced by the indexing, the photon PDF in a Mellin space representation, but the anomalous dimension as defined above. In certain contexts, the Mellin space evolution may be more practical to perform since the resemblance to a first order differential equation allows for analytically defined PDF distributions to be exponentiated (loosely speaking) by the anomalous dimension, $\sim e^{\gamma_{ij}}$, rather than having to perform computationally expensive convolutions. The PDFs themselves may then be simply obtained by performing the inverse transformation of Eq. (4.3).

This is the approach adopted by NNPDF, whose other distinct difference we highlight for the remainder of this section. First, we note that rather than using a purely polynomial parameterisation NNPDF instead defines input PDFs in terms

of a Neural Network (NN), $NN_i(x)$, a graph of connected, computational elements ("neurons") with many parameters capable of providing a flexible representation of the PDFs. With a simple polynomial term, known as the preprocessing exponents (included to speed up the fit), their inputs are then given as:

$$f_i(x,Q_0^2) = A_i x^{-\alpha_i}(1-x)^{\beta_i} NN_i(x). \tag{4.5}$$

Gradient based approaches for many parameter models such as NNs are often computational expensive to execute for the purposes of a fit. Therefore, in order to minimise the χ^2 to a suitable degree (without over-fitting, discussed below), a genetic algorithm approach is adopted, in which the parameters of the network are coded into a sequence of variables, which are then randomly generated and "bred" (by suitably merging their strings of values for the parameters in the network) and selected over successive generations.

Since the NN's number of free parameters is an order of magnitude larger than those of Hessian based PDFs, in order to prevent over-fitting, the data used in the calculation of the χ^2 is split into training and validation sets, where the χ^2 calculated from the training data is minimised, while monitoring the appropriate change in the out-sample (validation data) χ^2. When the reduction in the training fit no longer leads to similar reductions in the validation χ^2 (or indeed it begins to increase), the minimisation with respect to the former is halted, yielding a set of parameters for the network.

Finally, errors in the NNPDF formulation are produced in the "Monte-Carlo" fashion rather than the Hessian approach outlined above. In this strategy, the parameters of the PDFs are not systematically varied about the value of best fit but the data themselves are varied subject to their associated errors about their own central values (in a Gaussian manner) to create replica data-sets. The PDFs are then fit to each of these replica data sets to produce many variations of the PDFs, which are then averaged, with the standard deviation of the PDF replicas used to define the uncertainty bands for the PDFs.

Recently, it has been shown that the Hessian and Monte-Carlo approach to PDF

error generation have a correspondence to one another, and that the two representations of the PDFs may in fact be related to one another [80]. A Monte-Carlo produced set of PDFs, such as NNPDF, may be converted into a Hessian representation by using a sample of the Monte-Carlo PDFs to determine the parameter variations needed (as in Eq. (4.1)) for each eigenvector direction in parameter space and vice versa [81]. Furthermore, converting one set to the other and back reproduces the initial PDFs to a good degree of correspondence, demonstrating the robustness of this method. Therefore, one may freely relate the error sets produced by one method to the other, with a good agreement seen between the two approaches.

4.3 MMHT Framework

The broad features of the MMHT approach to PDF fitting, (polynomial parameterisation, a Hessian approach to uncertainties and x-space DGLAP evolution) were given in the previous section. Here we elaborate on the precise methods used at each step.

The partons are parameterised solely at the input scale, the majority of which, as discussed in section 2.1 of [78], are based on an expansion of Chebyshev polynomials ($T_i^{Ch}(y)$). These have the convenient property of $T_i = 1$ for $y = \pm 1$ and vary in such a way that in the fit the a_i are seen to be well behaved (and small in magnitude), producing smooth PDFs that vary in the phenomenologically relevant regions of x as outlined in Table 4.1 to produce a good fit (as studied in [82]):

$$xf(x,Q_0^2) = A(1-x)^{\eta}x^{\delta}\left(1+\sum_{i=1}^{n} a_i T_i^{Ch}(y(x))\right), \tag{4.6}$$

with $y = 1-2\sqrt{x}$ and $n = 4$. Distributions of this form are used for $f = u_V, d_V, S, (s+\bar{s})$, where S denotes the light-quark sea distribution:

$$S = 2(\bar{u}+\bar{d})+s+\bar{s}, \tag{4.7}$$

and the parameters A, η, δ, a_i are all left free, determined simultaneously in the fit to the data. An exception is the parameter A in the instance of the u_V and d_V distri-

butions, where rather than being fit to data, it is determined by the valence number rules (Eq. (3.22) of the previous section), since A is essentially the normalisation constant of the entire distribution. The differences $\bar{d}-\bar{u}$ and $s-\bar{s}$ are then provided in a form with a reduced parameterisation (fewer free parameters), practically chosen to reflect the inability of the data to constrain these distributions to a high degree (outlined in section 2.1 of [78]).

In addition to this, the gluon is provided in a form similar to Eq. (4.6), but with an additional term:

$$xg(x,Q_0^2) = A_g(1-x)^{\eta_g}x^{\delta_g}\left(\sum_{n=1}^{2} a_{g,i}T_i^{Ch}(y(x))\right) + A_{g'}(1-x)^{\eta_{g'}}x^{\delta_{g'}}. \tag{4.8}$$

This term is included since it has been found to significantly improve the quality of a global fit for the partons [83], and essentially provides more freedom for the gluon at low x. In particular, η_g, η_g', A_g and A_g' are all correlated in the fit, and are delicately balanced to provide the best fit for the gluon in this region. In particular, while the former two terms tend to increase the gluon contributions at low x, in the fit, the latter terms display a preference for reducing the gluon in the same region and these effects cancel each other out to a degree during the fitting procedure. However, unlike the other parameters A_g is not fit from the data but is instead constrained solely by the conservation of momentum as given in Eq. (3.21).

As will be shown in Chapter 8, upon the introduction of QED effects the gluon parameters can be artificially disrupted, leading to significant changes in the gluon if the partons are not refit (discussed in more detail in Section 8.2). In total, the MMHT parameterisation yields 36 free parameters, which after freezing the value of 11 of them after determining the best fit (as described above, to ensure the stability of the diagonalisation in parameter space) leads to 50 eigenvector variations for the PDF uncertainties.

The Hessian matrix in the previous section was given as:

$$H_{lm} = \frac{1}{2}\sum_n \frac{\partial \chi_n^2}{\partial a_l \partial a_m}, \tag{4.9}$$

where the sum over n indicates the sum over data sets incorporated into the fit. In the treatment of the χ^2 itself as a measure of the "goodness of fit" of the PDFs, one needs to incorporate the correlated errors associated with the data. Furthermore, systematic errors associated with the experiment in essence allow for normalisations $\mathcal{N}_n$ of entire data sets to better align the predictions from the PDFs with experimental observations. However, the change induced by such a normalisation $(1-\mathcal{N}_n)$ must also be penalised in the fit (to prevent shifting all data in line with the predictions and over-fitting).

To simultaneously accommodate all of these requirements, the χ^2_n for a given data set is defined, for data points $D_{n,i}$ and theoretical predictions $T_{n,i}(\{a\})$ (a function of the set of PDF parameters a) as:

$$\chi^2_n(a,\mathcal{N}_n) = \sum_{i=1}^{N_{pts}} \left(\frac{\hat{D}_{n,i} - T_{n,i}(\{a\})/\mathcal{N}_n}{\sigma^{uncorr}_{n,i}} \right)^2 + \sum_{k=1}^{N_{corr}} r^2_{n,k} + \chi^2_{\mathcal{N}_n}, \tag{4.10}$$

where $\chi^2_{\mathcal{N}_n} = ((1-\mathcal{N}_n)/\sigma^{\mathcal{N}}_n)^2$ is a penalty term for normalisation against the 1σ normalisation term for data set n, and analytic expressions for the best fit values of $r_{n,k}$ may be found in section 5.2 of [79], where the statistic procedure is outlined in greater detail (which in turn is adopted from [84, 85]).

This completes a definition for the Hessian (Eq. (4.9)) which is then minimised with respect to the parameters using the Levenburg-Marquardt method [86, 87], which used the information of the local gradients to incrementally reach a minimum.

During the evolution, at a given step in Q^2, the PDFs are defined at 96 logarithmically spaced values of x. The integration procedure used to perform the convolutions associated with DGLAP (Eq. (3.14)) is Gaussian-Legendre Quadrature, in which an integral is approximated by the weighted sum of the function as defined on several points:

$$\int dx f(x) \simeq \sum_{i=1}^{n} w_i(x_i) f(x_i), \tag{4.11}$$

which holds to a good degree of approximation provided the number of points n is

greater than the degree of a polynomial which can suitably approximate the function being considered (or is greater than the degree of $f(x)$ if it is already provided as a polynomial).

A complete discussion of the coefficient functions, $C_i(x, Q^2)$ and differential cross section $d\sigma$ calculations used during the fit to make comparisons to the processes provided in Table 4.1 is beyond the scope of the discussion provided here, though is covered extensively in [79] and [78], where the details of the MMHT (and predecessor set MSTW) are provided more extensively. However, in Chapter 10 we shall discuss the implementation of such a cross section calculation when investigating photon-initiated Drell-Yan processes (fourth from the bottom in Table 4.1).

We conclude this Chapter by summarising the method in which the PDF sets are stored and used in practical circumstances (for example, the calculation of a cross section). As described above, in the MMHT framework, during the evolution the PDFs are defined on 96 grid points in x space, which are then interpolated between when an intermediate value between those points is needed (for example, in the calculation of a coefficient function) at a given Q^2. Similarly, the DGLAP evolution itself occurs incrementally in small, logarithmically spaced steps in Q^2 with the PDFs being defined at fixed points in both variables, $xf(x, Q^2)$.

Since the values are only stored computationally at fixed points, the final PDF is represented as a grid of values at pre-defined points in x and Q^2, referred to simply as a "grid". There is typically one such grid for the central values of the PDFs as defined at input and their subsequent evolution, and one extra grid for every eigenvector direction determined by the independent uncertainties (50 in the case of MMHT). The set of grids is what is known as the "PDF set".

In order provide a consistent manner in which such grids may be used by different software tools designed for cross section calculations, as well as providing a standardised means of re-interpolating from grids to continuous representations of the PDFs, modern grids are defined in a format consistent with LHAPDF6 [88], a software package that provides an interface in Fortran and C++ for obtaining

$f(x, Q^2)$ and its associated uncertainties from the PDF grids.

Provided a grid is supplied in the correct format, LHAPDF6 also provides convenient methods for producing PDF uncertainties. The final output from this thesis is provided as a set of grids in the LHAPDF6 format, as discussed in Appendix B.

With a discussion of the general approach to PDF determination, for the case of pure QCD splitting kernels, in place, we may now extend our discussion to the inclusion of the effects of QED within the evolution itself, which is the focus of the next chapter.

Chapter 5

The Inclusion of QED

Having laid the theoretical and practical foundations for the PDFs (in the case of pure QCD DGLAP evolution), we now consider the effects of QED and the various strategies one may implement to incorporate its effects into the determination of the PDFs, beginning with a brief summary of the motivations to pursue this goal. We note that in Chapter 2, the gluon was brought into consideration as a parton with its own associated distribution under the theoretical framework that QCD provided, where processes at various orders in perturbative field theory (in modern sets, up to NNLO) provided scaling corrections and determine the form of DGLAP evolution.

In particular, the gluon emerges by extending the pure quark model of hadrons to include diagrams such as the left-hand side of Fig. 2.2 (where a quark is seen to emit a gluon at LO). Furthermore, in Chapter 2, we highlighted that at LO, the emission of a gluon, up to coefficient terms related to the gauge symmetries, is diagrammatically identical to that of photon emission in QED. More generally, since the quarks carry electromagnetic charge, QED processes, diagrams in which one of the lines in the associated splitting diagram is a photon rather than a gluon, may enter into the calculation of splitting kernels.

As mentioned in Chapter 3, technically the order to which the splitting kernels are calculated should match the order in which the cross section for the process being studied (in a hadron-hadron collision or DIS for example) is being calculated, e.g. NLO QCD PDFs for a process calculated to NLO in QCD. Although the pure QCD kernel PDFs have been a reasonable approximation in most cases

until present, as the accuracy of cross section calculations and experimental precision has become $\sim \mathcal{O}(\alpha)$, with electroweak corrections being applied to cross section calculations, the effects of QED have needed to be incorporated. Extending the splitting kernels to include QED effects, though the calculations themselves require the effort generally involved in the determination of higher order Feynman diagrams, is straightforward to comprehend from a theoretical perspective, in light of the discussion above.

As we shall discuss at greater depth in Chapter 6, splitting kernels have been developed at $\mathcal{O}(\alpha)$, $\mathcal{O}(\alpha\alpha_S)$ and $\mathcal{O}(\alpha^2)$ [20][21], which are straightforwardly incorporated into the DGLAP evolution frameworks of modern PDF sets. However, as noted in the previous chapter, the evolution of the partons to all phenomenologically relevant regions of x and Q^2 involves an initial set of PDFs, constrained from the data (as in the processes given in Table 4.1). Therefore, one must include the photon, γ, as an independent PDF distribution at input, $x\gamma(x, Q_0^2)$, which must be evolved and coupled to the other partons for a fully consistent set of QED evolved PDFs.

As well as providing the necessary accuracy in the partons for electroweak processes in hadron scattering events, as mentioned in the introduction to this thesis and explored in Chapter 9, by including the photon (in both its elastic and inelastic components, as explained below), we introduce the possibility for a growing landscape of phenomenology offered by photon-initiated (PI) processes, in which the photon enters as either one or both of the incoming partons. Such processes may be sensitive to investigation at the CoM energies of the LHC at present (13 TeV) in proton-proton collisions, and will become more feasible to study in experimental set ups such as those of the High-Luminosity LHC.

Examples of such processes include electroweak boson pair production, top quark pair production, Higgs boson production associated with a W boson and photon initiated Drell-Yan at low ($M_{ll} \ll M_Z$) and high ($M_{ll} \gg M_Z$) dilepton masses, which are illustrated in Fig. 5.1. At time of writing, the most recent investigation [90] of the relative difference to cross sections induced by these processes (from

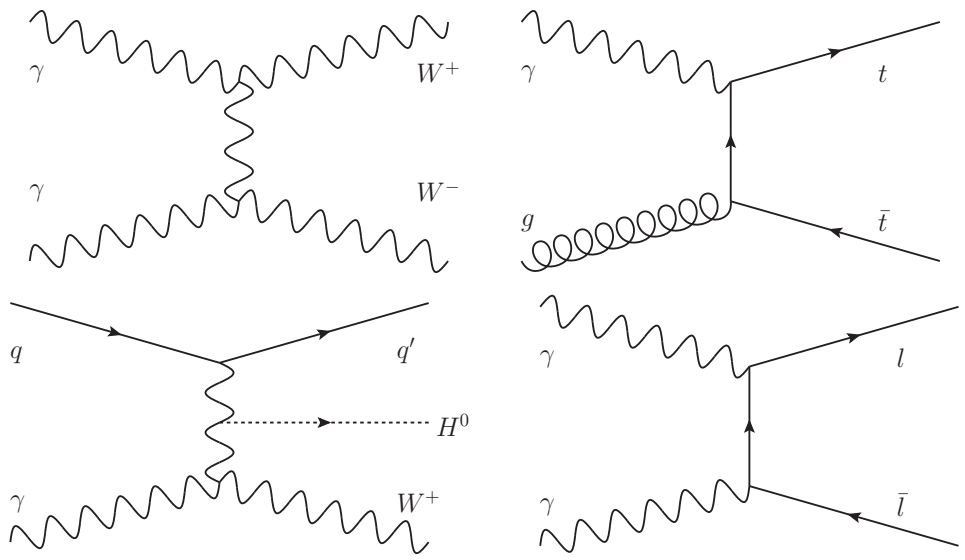

Figure 5.1: Feynman diagrams illustrating examples of photon initiated (PI) processes. Top Left: electroweak vector boson pair production from the γ-γ channel; Top Right: $t\bar{t}$ production from γ-g scattering; Bottom Left: Higgs production with an associated W boson from γ-q scattering; Bottom Right: photon initiated Drell-Yan (discussed in greater depth in Chapter 9).

that of the NNPDF3.1luxQED PDF set, which as will be shown in Chapter 8, bears a strong resemblance to the $\gamma(x, Q^2)$ distribution developed in this thesis) are given in Table 5.1. All PI processes shown are expected to have some experimental sensitivity for a given region in phase space with the exception of $t\bar{t}$ production. This is because it is most sensitive to the high x content of $\gamma(x, Q^2)$, which we shall show in later chapters is proportionally very small in comparison to the other parton contributions. In Chapter 9, we shall demonstrate this more thoroughly for the case of high mass Drell-Yan.

Having motivated the need to produce QED corrected PDFs, we now focus the remainder of this chapter on the determination of the input distribution for the photon, $x\gamma(x, Q_0^2)$ and how it differs from that of the other partons. Since, as shown in Table 4.1, only one process (Drell-Yan) is weakly sensitive to the $\gamma(x, Q^2)$ distribution in the fitting process at high x, alternative approaches have typically been used to determine its initial distribution, in contrast to that of the other PDFs. A brief summary of the history of photon PDFs is provided below.

Anticipated experimental sensitivity to photon-induced sub-processes			
Process	Cross Section Variables	Relative change to cross section	PDF uncertainty
High mass VV production	M_{WW}, p_T^W	∼1-35%	∼1-5%
Top pair production	M_{tt}, p_T^{tt}	$\sim 10^{-5}$	$\sim 10^{-2}$
Higgs + W	P_T^H,$\lvert y_h \rvert$	∼2-5%	∼1-3%
Low mass Drell-Yan	M_{ll},$\lvert y_{ll} \rvert$	∼3-4%	∼1%
High mass Drell-Yan	M_{ll},$\lvert y_{ll} \rvert$	∼1-6%	∼0.5-35%

Table 5.1: A table documenting various processes with PI contributions, the variables that the cross section is dependent on, the relative change in the cross section induced by PI contributions and, for comparison, the uncertainty associated with the PDFs in the relevant range for PI contributions [90].

5.1 The Photon as a Parton

While QED provides a description of the production of photons from individual quarks, the development of a theoretically well determined photon PDF distribution requires a slightly broader framework than that provided solely from DGLAP and the relevant QED splitting kernels.

First, as alluded to in Chapter 2, the photon itself arises as from the canonical quantisation of the fields, where the photon is associated with the (emergent from electroweak symmetry breaking) A_μ field of QED. This picture suggests that any source of an electromagnetic field may equivalently be considered as a source of photons, with the relevant field strength defining an increased flux of photons. This picture was formalised by Weizsacker [91] and Williams [92] (who in turn adapted work from Fermi [93]), which came to be known as the equivalent photon approximation (EPA).

In such a framework, any source of charge is a source of photons that may contribute to a scattering process. This observation leads to one of the primary distinguishing features of the photon PDF. We noted in Chapters 2 and 3 that the nature of confinement inside hadrons due to QCD is such that isolated quarks and gluons are not observed and that their individual, point-particle like nature is only appar-

ent at high energy scattering processes. Because the proton carries no "net" QCD colour charge, to be sensitive to the colored partons, such processes are necessarily inelastic[1], and leads to the proton disassociating into a jet of hadrons.

This need not be true for the photon, since the proton carries net, non-zero electromagnetic charge, producing a net electromagnetic field flux. Using the EPA, one can associate the presence of this electromagnetic field with a density of photons whose kinematic distribution acts as an effective photon PDF that enters into the calculation of cross sections in proton-proton collisions where the incoming lines of the internal process are photons. Such was the approach adopted by Budnev et al [94], to calculate cross sections such as those for lepton production from photon photon scattering between protons [95] (the lower right hand side of Fig. 5.1).

Therefore, as well as the "intrinsic" photon component that arises from DGLAP evolution, there exists a photon component that is in some sense "extrinsic" to the proton. A clearer distinction between these two contributions is to distinguish the photon distributions by the final state of the proton in the scattering process. One associates the photon flux associated with elastic photon scattering, simply as the "elastic" component of the photon, while inelastic proton scattering defines the "inelastic" component of the photon flux. This terminology, specifically in referring to the two components of the photon PDF, $\gamma^{(el)}$ and $\gamma^{(inel)}$, will be used for the remainder of this thesis.

Further clarification will be given below, but here we highlight that in general, the input distribution $x\gamma(x, Q_0^2)$ is generally modelled by considering how the photon density arises from either the point charges of the charged quarks themselves, the proton in its entirety, or by considering the exact nature by which the photon enters into scattering processes. The latter approach, which requires experimental determination from structure functions rather than phenomenological modelling from the existing PDFs, has proven in recent years to be the most reliable and least

[1]Note that this does not mean that only inelastic scattering processes are sensitive to the QCD nature of the proton, as the exchange of net colour-neutral QCD objects may occur, as in Pomeron exchange, where both protons may scatter elastically. However, in such a case, one cannot treat the incoming line of the scattering process as an individual quark or gluon, as in the Feynman diagrams shown in previous chapters.

susceptible to theoretical and experimental uncertainty. However, for the purposes of completeness and comparison, we provide a brief overview of the former approaches below.

5.2 Previous Determinations

The earliest publicly available QED corrected PDF set was that of MRSTQED04 [12]. In this framework, which extended the MRST PDFs, as well as the inclusion of LO QED splitting kernels in the PDFs, the input photon distribution at Q_0^2 = 1 GeV^2 was considered to arise radiatively from the valence quark distributions. Specifically, a leading-logarithm approximation was used, which yielded the following expression for the photon at input:

$$\gamma(x,Q_0^2) = \frac{\alpha}{2\pi}\left[\frac{4}{9}\log\left(\frac{Q_0^2}{m_u^2}\right)u_0(x) + \frac{1}{9}\log\left(\frac{Q_0^2}{m_d^2}\right)d_0(x)\right] \otimes \frac{1+(1-x)^2}{x}, \quad (5.1)$$

where the u_0 and d_0 are "valence-like" distributions for the proton that satisfy the flavour sum rules $\int_0^1 dx u_0 = 2, \int_0^1 dx d_0 = 1$. This expression also retains a dependence on quark masses, m_u and m_d, which determine the scale from which the quarks are taken to radiate in the leading-log approximation. Since the quarks are not observed as free particles, (and masses in QFT are technically renormalised parameters), one may consider two approaches to accounting for these parameters. The predominant approach used was the "current" mass scheme, in which the quark masses are assumed to be light, in line with predictions from lattice QCD (the choices used in MRST were m_u = 6 MeV, m_d = 10 MeV). Alternatively, one can consider the quark masses in the low energy picture in which the valence quarks are the dominant contribution to the proton's binding energy, the "constituent" mass scheme ($m_u \simeq m_d \simeq 300$ MeV). In practice, the difference between choices for the quark masses was negligible for the overall fit quality of the partons, though the current mass choice was theoretically favoured since in principle, a radiative QED process should be largely insensitive to the strong scale binding energy of QCD (which is essentially the mechanism of generating large masses in the constituent mass framework).

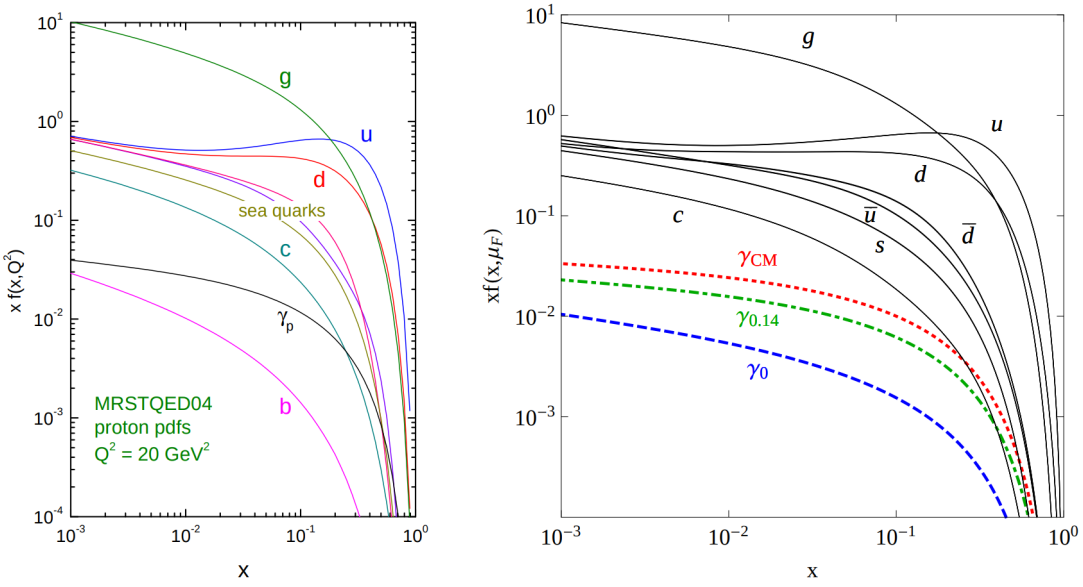

Figure 5.2: Left: the MRSTQED04 partons [12] at $Q^2 = 20$ GeV^2. Right: the CT14QED partons [13] at $Q = 3.2$ GeV.

This set also introduced an approximation for a QED corrected neutron PDF (discussed in greater detail in Chapter 7), using the assumption that charge sensitive splitting functions would create differences in the u_V and d_V valence distributions, such that isospin symmetry between the hadrons (e.g. $u_{V,(p)}(x) = d_{V,(n)}(x)$) was broken. In combination, the isospin violating neutron and proton PDFs were seen to reduce the $sin^2\theta_W$ NuTeV anomaly [22] from a $\sim 3\sigma \rightarrow \sim 2\sigma$ discrepancy. The photon PDF itself was validated by considering the LO sub-process of QED compton scattering $e\gamma \rightarrow e\gamma$ in ep scattering with data measured from the ZEUS collaboration [97], and was shown to have modest agreement, with the current mass photon providing a slightly better fit, though the uncertainties on the measurement and the theoretical uncertainties (taken from a conservative variation of the PDF scale, $E_T^\gamma/2 < Q < 2E_T^\gamma$) were both relatively large.

Considering a similar approach, the CTEQ14QED [13] set generalised the MRST approach with a method that was independent of the quark mass choices. Instead, it relied on a more general parameterisation which absorbed the mass de-

pendency into normalisation constants $A_i = \ln Q_0^2/Q_i^2$:

$$\gamma(x,Q_0^2) = \frac{\alpha}{2\pi}\left[\frac{4}{9}A_u u_V(x,Q_0^2) + \frac{1}{9}A_d d_V(x,Q_0^2)\right] \otimes \frac{1+(1-x)^2}{x}, \qquad (5.2)$$

with $Q_0^2 = 1.295\ \text{GeV}^2$.

Rather than attempting to determine a precise mass scale from which the radiation occured, the CTEQ parameterisation constrained the normalisation of the photon PDF by first taking the assumption that $A_u = A_d$ and then noting that in fact the normalisation may be determined by considering the overall momentum carried by the photon at input: $p_0^\gamma = \int_0^1 x\gamma(x,Q_0^2)$. This was done by considering an $\mathcal{O}(\alpha)$ corrected cross section for the Compton scattering sub-process at ZEUS used by the MRST set for validation, to determine a best fit value of $p_0^\gamma = 0.14$. This PDF bore a resemblance to that of MRSTQED04, but was better able to determine an uncertainty for the photon PDF, making use of improved theoretical calculations for the Compton scattering sub-process used in the fit.

While both MRSTQED04 and CTEQ14QED, illustrated in Fig. 5.2, relied on a phenomenological model, based on radiative production from the quarks, other approaches were pursued independently by groups who sought to constrain the photon PDF in an unbiased way purely from the data, described in the next section.

5.3 Approaches based on fitting to high-mass Drell-Yan Data

The previously described approaches relied on phenomenological models based on quark radiation. As such, the $x\gamma(x,Q^2)$ distributions associated with these sets correspond to the $\gamma^{(inel)}$ distributions, since no provision was made for elastic proton scattering. In determining $x\gamma(x,Q^2)$ from data, one is in principle determining the entirety of the photon PDF $\gamma = \gamma^{(inel)} + \gamma^{(el)}$, since typically the data used (Drell-Yan and DIS) does not distinguish between the state of the proton post-scattering. However, although these approaches implicitly encompass the elastic component, in contrast to the MRST and CTEQ sets, as described below, they are susceptible to

large uncertainties.

The NNPDF2.3QED set [14] aimed to determine $x\gamma(x,Q^2)$ in a manner analogous of that to the other partons, providing a general ansatz at $Q_0^2 = 2$ GeV^2, in the form of the output from its neural network (modified by a pre-processing component):

$$\gamma(x,Q_0^2) = (1-x)^{m_\gamma} x^{-n_\gamma} NN_\gamma(x), \tag{5.3}$$

where $1 \leq m_\gamma \leq 20$ and $-1.5 \leq n_\gamma \leq 1.5$ are preprocessing exponents that are selected from uniform distributions for each PDF replica in the NNPDF scheme.

The processes used to constrain the photon in the fit consisted of QED corrections to DIS (in which the photon enters as an initiating parton, which subsequently radiates a quark to reproduce the LO DIS diagram for quark-photon scattering, where the latter photon is the internal line between the quark and the lepton probe) and Drell-Yan, which as briefly described above (and elaborated on in Chapter 9) is one of the processes sensitive to photon initiated processes.

Although unbiased (since its ansatz assumed no theoretical prior on the photon's production at input), the low sensitivity of both of these processes were only able to weakly constrain the $x\gamma(x,Q^2)$, with the fit subsequently generating large uncertainties, particularly at input and at low Q^2 ($\mathcal{O}(100\%)$). At higher Q^2 scales, $x\gamma(x,Q^2)$ also displayed systematic differences from those of MRST04QED and CTEQ14QED, particularly at low x as shown in Fig 5.3, which was in large part found to be due to the manner in which the DGLAP evolution was performed (in the Mellin space convolution). For the initial NNPDF2.3QED set, the QCD and QED anomalous dimensions being applied successively to the PDF distributions, $\sim e^{\gamma_{ij}^{(QED)}} e^{\gamma_{ij}^{(QCD)}} f_j(N,Q^2)$, rather than jointly $e^{\gamma_{ij}^{(QED)}+\gamma_{ij}^{(QCD)}} f_j(N,Q^2)$, leading to $\mathcal{O}(\alpha\alpha_S)$ differences.

A similar approach based on constraining $x\gamma(x,Q^2)$ from data was also undertaken by the xFitter group [15]. In their analysis, a photon PDF was fit to high-mass Drell-Yan di-lepton production data from ATLAS ($\sqrt{s} = 8$ TeV) [23], using the

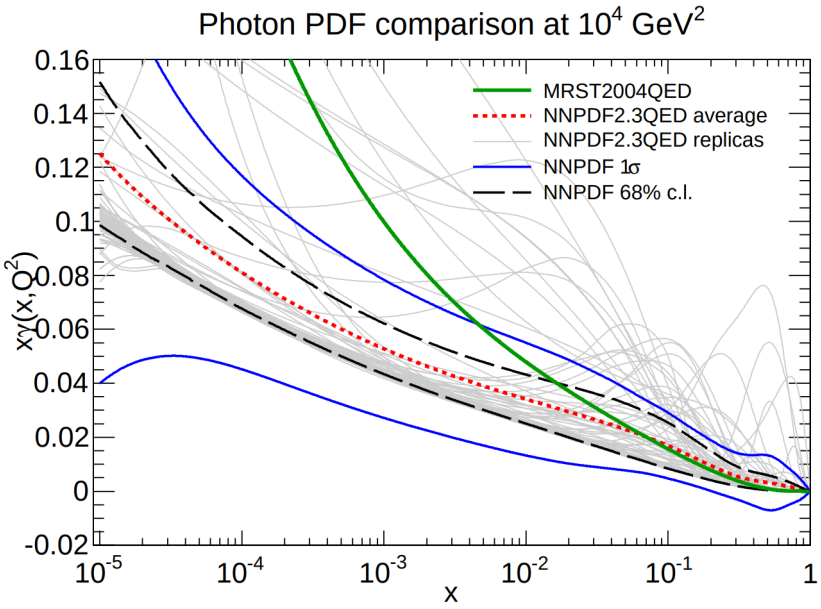

Figure 5.3: A comparison of the NNPDF2.3QED $x\gamma(x,Q^2)$ with that of MRST04QED at $Q^2 = 10^4$ GeV^2, adapted from [14].

following ansatz:

$$x\gamma(x,Q_0^2) = A_\gamma x^{B_\gamma}(1-x)^{C_\gamma}(1+D_\gamma x+E_\gamma x^2), \tag{5.4}$$

for $Q_0^2 = 7.5$ GeV^2. Errors were produced with a Monte-Carlo approach and validated by comparison to a Hessian approach with $\Delta\chi^2 = 1$ uncertainty bands. Though the uncertainties were found to be somewhat smaller than that of NNPDF2.3QED, they were still found to be large relative to the other partons, ($\sim 30\%$ for $0.02 \leq x \leq 0.1$).

In general, attempts to fit solely to photon initiated corrections to processes such as Drell-Yan at hadron hadron colliders are susceptible to large uncertainties due to the relatively modest contributions to the overall cross section, as well as an absence of the sufficiently high experimental precision. However, in recent years, another approach has been used that relies on fitting to experimental measurements of a distinctly different category. Specifically, a new theoretical underpinning was developed that associated $x\gamma(x,Q^2)$ with the internal photon line of DIS scattering processes used in the measurement of nuclear form factors.

Since the form factors themselves are experimentally well determined, photon PDFs based on this approach have achieved at least a tenfold improvement in accuracy compared to approaches such as those of NNPDF2.3QED and the xFitter collaboration. These approaches will be the focus for the remainder of this chapter and will provide the foundation for the $x\gamma(x,Q^2)$ developed in this thesis.

5.4 Approaches based on Nuclear Form Factors/LUX Determination

As described at the beginning of this chapter, the most general form of determination for the photon PDF comes from considering how the equivalent photon density arises from the charge weighted structure of the proton, from the equivalent photon approximation.

Building on this approach, Glück et al [98] proposed a means of determining the photon PDF based on measurements of nuclear structure, in a manner that separated the $\gamma^{(el)}$ and $\gamma^{(inel)}$ components. This approach is predicated on the realisation that the internal photon line in lepton-nucleon scattering (as shown in the central portion of Fig. 3.1) is in essence the same as the photon PDF (the momentum density of the photon flux that contributes to scattering processes).

This is justifiable from the fact that the factorisation theorem, which we have previously stated is used to utilise the universality of nucleon scattering events in order to better determine the same PDFs from disparate scattering process, also applies to QED. In the following discussion, we shall generalise to consider both the proton and neutron as the nucleon undergoing scattering.

While the $x\gamma^{(inel)}(x,Q^2)$ in [98] was driven solely from quark radiation from the partons, as in previous approaches, they considered an elastic contribution of the following form:

$$-\frac{\alpha}{2\pi}\int_{t_{min}}^{t_{max}}\frac{dt}{t}\left\{\left[2\left(\frac{1}{y}-1\right)+\frac{2m^2y}{t}\right]\frac{G_E^2(t)+\tau G_M^2(t)}{1+\tau}+yG_M^2(t)\right\}, \qquad (5.5)$$

where $t=-Q^2$ and $\tau=-t/4m^2$. In this way, the two components of $x\gamma(x,Q^2)$ were

defined independently.

It should also be noted that the CTEQ14QED set also defined grids that differentiated the $\gamma^{(inel)}$ from the total (which in turn could allow one to determine the coherent component from subtraction). However, since the entire photon PDF was fit from momentum normalisation to the ZEUS data, instead of phenomenologically defining different forms for the inelastic and elastic components, they estimated the inelastic component by imposing cuts on the ZEUS data to define the contribution solely to $\gamma^{(inel)}$, $10^{-3} < x < 2\times10^{-2}$ for $16 < Q^2 < 300\,\mathrm{GeV}^2$, with the $\gamma^{(inel)}$ being found to carry 0.14% of the proton's total momentum.

Martin and Ryskin [16] proposed the following form[2] which more closely resembled the nuclear form factor approach adopted by [98] for $x\gamma^{(el)}(x,Q^2)$:

$$\gamma^{(el)}(x,Q_0^2) = \frac{\alpha}{2\pi}\frac{[1+(1-x)^2]}{x}\int_0^{|t|<Q_0^2} dq_t^2 \frac{q_t^2}{(q_t^2+x^2m_p^2)^2}F_1^2(t), \tag{5.6}$$

where q_t is the transverse momentum carried by the photon and

$$t = \frac{q_t^2 + x^2m_p^2}{1-x}. \tag{5.7}$$

F_1 corresponds to the electromagnetic form factor for the nucleon under consideration, though for the neutron the entirety of $\gamma_{(n)}^{(el)}$ is taken to be 0. This is anticipated since the neutron carries net 0 charge and therefore the net flux of electric field across a surface encapsulating a neutron is also 0. In Chapter 7 we shall show that although the net charge of the neutron is 0, its small electric and magnetic dipole moments produce a contribution to $\gamma_{(n)}^{(el)}$, though substantially smaller than that of $\gamma_{(n)}^{(inel)}$.

In essence, Eq. (5.6) is essentially the product of a convolution of the $P_{\gamma q}$ kernel with the charge distribution of the proton in elastic scattering. The inelastic component meanwhile, similar to that of [98], $x\gamma^{(inel)}(x,Q^2)$, is adapted from the phenomenological model of MRST04QED, but with an additional factor $(1-F_1^2)$

[2]Note that in their original paper, the terminology adopted is that of the coherent and incoherent contributions.

to express that the quark-generated contribution of the photon PDF is only relevant in inelastic scattering processes:

$$\gamma^{(inel)}(x,Q_0^2) = \frac{\alpha}{2\pi}\int_x^1 \frac{dz}{z}\left[\frac{4}{9}u_V(\frac{x}{z},Q_0^2)+\frac{1}{9}d_V(\frac{x}{z},Q_0^2)\right]\frac{1+(1-z)^2}{z}\times \int_{|t_{min}|}^{Q_0^2}\frac{dt}{t-m_q^2}(1-F_1^2(t)), \tag{5.8}$$

where

$$t_{min} = \frac{x}{(1-x)}(m_\Delta^2-(1-x)m_N^2), \tag{5.9}$$

which accounts for the fact that the lowest energy possible nucleon excitation is to the Δ baryon isobar state. Since the lower bound of the dt integral induces a convolution of the valence quark distributions below the starting scales, a scheme is developed to linearly interpolate between the point-like quark approximation at the lowest energy scales (e.g. $u_V(x) = u_{V,non-rel} = 2\delta(x-1/3)$) and the standard valence input distribution, with a dependence on the effective mass of the quarks. The full details may be found in [16], and one notes that in this scheme, $\gamma^{(inel)}$ still involves a dependency on a phenomenological model based on radiative quark emission.

Though this model was further developed in some respects (such as changing the dependence on $(1-F_1^2(t))$ to $(1-G_E^2(Q^2))$, where G_E is the Sachs electric form factor, which better models the probability for coherent photon emission in elastic scattering), in subsequent papers [17] detailing the HKR photon set (as it came to be known), the combination of theoretical and experimental uncertainties (carried forward from nuclear form factor measurements), led to a $\sim 10-15\%$ uncertainty on the total photon PDF at input, reducing to $\sim 5\%$ at higher scales.

The final removal of dependency on phenomenological modelling of radiative emission from the quarks came with the LUXqed [19] formulation of $x\gamma(x,Q^2)$. In their paper, they drew a more direct relationship between the internal photon line in ep scattering processes and the photon PDF. Since the $x\gamma(x,Q^2)$ and subsequent delineation into the $\gamma^{(el)}$ and $\gamma^{(inel)}$ components developed in this thesis are strongly dependent on the form of this input, we reserve a more detailed discussion of this

for the next chapter, where we discuss the LUXqed input distribution $x\gamma(x,Q_0^2)$ and its contributions.

To close this chapter, we outline how their expression for $x\gamma(x,Q_0^2)$ is obtained. In essence, they note that ep scattering may be equivalently considered as a scattering process, with a subprocess consisting of $e\gamma$, where the γ is precisely the photon PDF of the nucleon under consideration. To make this more readily apparent, they consider a fictitious lepton scattering process $l+p\to L+p$, where the lepton probe (massless) transforms to a massive ($M_L >> m_l \simeq 0$) probe at the lepton vertex of the standard DIS diagram. The details of such a process serve only as a framework from which to use the factorisation theorem to draw the equivalency between the photon line in a lepton probe scattering and the photon PDF.

In particular, they show that the cross section (based on definitions of the hadron tensor of DIS phenomenology as discussed in Section 3) for this fictitious heavy lepton production process is as follows:

$$\begin{aligned}\sigma = \frac{c_0}{2\pi}\int_x^{1-\frac{2xm_p}{M}}\frac{dz}{z}\int_{Q^2_{min}}^{Q^2_{max}}\frac{dQ^2}{Q^2}\alpha(-Q^2)\\ \left[\left(2-2z+z^2+\frac{2x^2m_p^2}{Q^2}+\frac{z^2Q^2}{M_L^2}-\frac{2zQ^2}{M_L^2}-\frac{2x^2Q^2m_p^2}{M_L^4}\right)F_2(x/z,Q^2)\right.\\ \left.+\left(-z^2-\frac{z^2Q^2}{2M_L^2}+\frac{z^2Q^4}{2M_L^4}\right)F_L(x/z,Q^2)\right],\end{aligned} \tag{5.10}$$

where $c_0 = 16\pi^2/\Lambda^2$ and $Q^2_{min} = x^2m_p^2/(1-z)$ and $Q^2_{max} = M_L^2(1-z)/z$. The F_2 and F_L are the proton form factors described in Chapter 3, that are measured from DIS and other nucleon scattering experiments.

As mentioned above, this may equivalently be considered as a scattering event between the photon PDF of the nucleon and the lepton vertex of the probe. In this framework, the same cross section may be expressed as:

$$\sigma = c_0\int_x^1\frac{dz}{z}\hat{\sigma}_\gamma(z,Q^2)\times\frac{M_L^2}{zs}\times\gamma\left(\frac{M_L^2}{zs},Q^2\right), \tag{5.11}$$

where we have assumed that the dominant contributing parton to this pro-

cess is the photon and denote the $l\gamma$ scattering sub-process as $\hat{\sigma}_\gamma$. By expanding $\hat{\sigma}_\gamma$, neglecting terms of $\mathcal{O}(\alpha^3 \ln(Q^2/m_p^2)(\alpha_S \ln(Q^2/m_p^2))^n)$ and $\mathcal{O}(\alpha^2 \alpha_S \ln(Q^2/m_p^2)(\alpha_S \ln(Q^2/m_p^2))^n)$ and requiring an equivalence between Eqs. (5.10) and (5.11), they obtain an expression for the photon PDF in terms of the proton structure functions:

$$x\gamma(x,Q_0^2) = \frac{1}{2\pi\alpha(Q_0^2)} \int_x^1 \frac{dz}{z} \Big\{ \int_{\frac{x^2 m_p^2}{1-z}}^{\frac{Q_0^2}{1-z}} \frac{dQ^2}{Q^2} \alpha^2(Q^2) \Big[\Big(z p_{\gamma,q}(z) + \frac{2x^2 m_p^2}{Q^2} \Big) F_2(x/z, Q^2) - z^2 F_L(x/z, Q^2) \Big] - \alpha^2(Q_0^2) z^2 F_2(x/z, Q_0^2) \Big\}. \tag{5.12}$$

Details of this expression are given in the next chapter.

This particular form for the photon, when considering the experimental sources that constitute $F_{2,L}$ in particular kinematic regions of the integral, is seen to be very well experimentally constrained, with $\mathcal{O}(2\%)$ errors over a broad range of x and Q^2 in the corresponding $\gamma(x,Q^2)$. This arises as a natural result of the well constrained nature of the nuclear form factors from various DIS experiments, whose exact contributions are detailed in Chapter 8.

With a well determined input distribution, and a framework for incorporating QED splitting kernels to determine their evolution, for the remainder of this thesis, we outline how a combination of these efforts have been used to incorporate a fully coupled DGLAP evolution of all the partons in the MMHT framework, and explore the consequences of the resulting set. Furthermore, after outlining the relevant procedures for the proton in the next chapter we shall detail in Chapter 7 how certain adaptations and approximations are made to extend this framework to a QED corrected neutron set.

Chapter 6

MMHTqed

The primary modification required of the existing MMHT framework was the incorporation of QED splitting kernels in DGLAP evolution and the form we take for the input distribution of the photon at the starting scale, taken as $Q_0^2 = 1$ GeV^2. Additionally, the calculation of structure functions F_2, F_3 and F_L from the partons, which are used to include DIS data in the fitting procedure, were amended to include leading order QED contributions. Here, we outline how those inclusions were performed and their effect on the final set of partons and corresponding uncertainties. Furthermore, much of the discussion will pertain to our development of the QED corrected Neutron PDFs, in Section 7.1.

6.1 QCD Basis of Comparison

Throughout this thesis, in order to meaningfully interpret the effects of including QED in the evolution, the photon PDF and the effects of subsequent refitting, we will compare the new partons to a baseline set of PDFs evolved and fit solely with QCD kernels (where, unless explicitly stated, the kernels used are at NNLO in QCD). However, it is necessary to distinguish that this set differs from the most recent public release of partons, MMHT2014 [78].

The basis of comparison used in this thesis more closely corresponds to the set described in reference [89], where the HERA run I + II combined cross section data [96] has been additionally included in the fit to constrain the partons. Furthermore, we now include some additional data on $t\bar{t}$ production ($\sigma(t\bar{t})$) from the ATLAS and

CMS collaborations in the fit.

Another minor improvement has been to the procedure for initiating the charm and bottom distributions in the evolution at the appropriate energy thresholds. At NNLO, the distributions appeared to be brought in one step in the evolution prematurely, creating a very small discontinuity in the interpolation between the Q^2 points used in the Gaussian-Legendre integration, an issue that was highlighted in adapting the procedure for the QED code. This has now been corrected.

Finally, small amendments have been made to the NLO and NNLO QCD kernels in the evolution, which are detailed in Section 6.3. In combination, these changes distinguish the reference "QCD" set used in this thesis against those outlined in MMHT2014 and all comparisons of the partons with and without the effects are QED in the following sections are made against the set described here.

6.2 Photon Input Distribution

To generate the partons from QED corrected DGLAP evolution (detailed in Section 6.3), requires an input distribution for the photon at some starting scale, $x\gamma(x, Q_0^2 = 1$ GeV^2), from which the PDFs may be evolved to higher scales.

As discussed in the last chapter, recently developed formulations of the photon PDF in terms of proton structure functions allows one to directly produce an input based on existing fits for the nuclear structure functions, in particular F_2 and F_L. In the following discussion, since the necessary relations (Eqs. (3-6) in [19]) for relating $F_{2,L}$ to $x\gamma(x, Q_0^2)$ are only valid when the internal line between the lepton probe and the relevant hadron in the scattering process is a photon, we will implicitly be referring to the Neutral Current (NC) structure functions wherever mentioned (i.e. $F_2 \equiv F_2^{NC}$, $F_L \equiv F_L^{NC}$). Since, at the scales concerned $Q_0^2 = 1\text{GeV}^2 \ll M_Z^2$, we can safely neglect any contributions from Weak NC scattering processes and related interference terms.

As mentioned in the previous chapter, the input expression used in MMHTqed is derived from that of LUXqed with some modification. From Eq. (6) of [19] (and also given in Eq. (3.26) of [99]), the standard form for their photon PDF (at a given

input scale, $\mu^2 = Q_0^2$) is given as:

$$x\gamma(x,Q_0^2) = \frac{1}{2\pi\alpha(Q_0^2)}\int_x^1 \frac{dz}{z}\Big\{\int_{\frac{x^2m_p^2}{1-z}}^{\frac{Q_0^2}{1-z}} \frac{dQ^2}{Q^2}\alpha^2(Q^2)\Big[\Big(zP_{\gamma,q}(z)+\frac{2x^2m_p^2}{Q^2}\Big)F_2(x/z,Q^2) - z^2F_L(x/z,Q^2)\Big] - \alpha^2(Q_0^2)z^2F_2(x/z,Q_0^2)\Big\}, \tag{6.1}$$

where $P_{\gamma,q}(z)$ corresponds to the $\mathscr{O}(\alpha)$ DGLAP splitting kernel given by:

$$P_{\gamma,q}(z) = \frac{1+(1-z)^2}{z}. \tag{6.2}$$

Note that the upper limit of the Q^2 integral, $\frac{Q_0^2}{1-z}$, introduces a dependency on terms at scales higher than the input scale. It is more convenient to eliminate this dependency in Eq. (6.1) such that one has a photon input purely dependent on contributions from scales $Q^2 < Q_0^2$, with all $Q^2 > Q_0^2$ dependency in the partons driven by DGLAP evolution (discussed in Section 6.3). Therefore, one separates this integral into two, with the limits $[\frac{x^2m_p^2}{1-z}, Q_0^2]$, $[Q_0^2, \frac{Q_0^2}{1-z}]$:

$$x\gamma(x,Q_0^2) = \frac{1}{2\pi\alpha(Q_0^2)}\int_x^1 \frac{dz}{z}\Big\{\int_{\frac{x^2m_p^2}{1-z}}^{Q_0^2} \frac{dQ^2}{Q^2}\alpha^2(Q^2)\Big[\Big(zP_{\gamma,q}(z)+\frac{2x^2m_p^2}{Q^2}\Big)F_2(x/z,Q^2) - z^2F_L(x/z,Q^2)\Big] + \int_{Q_0^2}^{\frac{Q_0^2}{1-z}} \frac{dQ^2}{Q^2}\alpha^2(Q^2)\Big[\Big(zP_{\gamma,q}(z)+\frac{2x^2m_p^2}{Q^2}\Big)F_2(x/z,Q^2)\Big] - \alpha^2(Q_0^2)z^2F_2(x/z,Q_0^2)\Big\}, \tag{6.3}$$

where we have dropped the F_L term in the second Q^2 integrand for simplicity (this is heuristically justifiable on the grounds that $F_L \ll F_2$ and also by consideration of the fact that $F_L \sim \mathscr{O}(\alpha_S)$ in the parton model, and the expression given in Eq. (5.12) is formally only accurate to $\mathscr{O}(\alpha\alpha_S, \alpha^2)$, a more thorough discussion of which is given in Section 3 of [99]).

By taking note of the fact that the scale variation of $F_2(Q^2)$ and $\alpha(Q^2)$ may be treated as stationary at the order at which we are calculating ($\partial F_2/\partial Q^2$, $\partial\alpha/\partial Q^2 \sim 0$ since the evolution of the structure functions occurs logarithmically as $\mathcal{O}(\alpha_S)$ corrections), we move both terms outside of the integral and evaluate it to yield the final expression for our input:

$$x\gamma(x,Q_0^2) = \frac{1}{2\pi\alpha(Q_0^2)}\int_x^1 \frac{dz}{z}\Big\{\int_{\frac{x^2m_p^2}{1-z}}^{Q_0^2}\frac{dQ^2}{Q^2}\alpha^2(Q^2)\Big[\Big(zP_{\gamma,q}(z)+\frac{2x^2m_p^2}{Q^2}\Big)F_2(x/z,Q^2) \\ -z^2F_L(x/z,Q^2)\Big] - \alpha^2(Q_0^2)\Big(z^2+\ln(1-z)zP_{\gamma,q}(z)-\frac{2x^2m_p^2z}{Q_0^2}\Big)F_2(x/z,Q_0^2)\Big\}. \tag{6.4}$$

This corresponds to an analogous expression derived in Eq. (4.10) of [99], where a similar approach is taken for the purpose of deriving the photon PDF's evolution. We note however that in our expression, the term of order $\mathcal{O}(m_p^2/Q_0^2)$ has been retained, since it is more significant at the input scale adopted in MMHTqed (Q_0^2 =1 GeV^2, as compared with Q_0^2 =10 GeV^2 in LUXqed). Finally then, Eq. (6.4) represents the form of the photon PDF input adopted in the MMHTqed framework, and for the remainder of this thesis when our photon input is referred to, it is understood as referencing this distribution.

In order to provide an understanding of how Eq. (6.4) is evaluated, here we elaborate on the composition of $F_{2,L}$ and how each source contributes to our expression for $x\gamma(x,Q_0^2)$. Firstly, as mentioned in the previous section, we note that $F_{2,L}$ receive contributions from both elastic and inelastic scattering processes, where the terms refers to the subsequent survival or disintegration of the proton being probed respectively, as shown in Fig. 6.1. In other words:

$$F_{2,L} = F_{2,L}^{(el)} + F_{2,L}^{(inel)}. \tag{6.5}$$

This distinction, as we shall see, plays an important role in the separation of γ into $\gamma^{(el)}$ and $\gamma^{(inel)}$ (as described in Section 6.4), where the former is a PDF contri-

bution that exists in elastic proton-proton scattering. The contributions to $F_{2,L}$ in the integrand are taken from fits to data. For the proton we adopt the same fits as those of LUXqed [99], as detailed below. Many of the uncertainties associated with these fits are also treated in an identical way (as discussed in Section 8.3), although we adopt several modifications to these fits, particularly when relating them for the photon PDF of the neutron (see Section 7.3).

For $F_{2,L}^{(el)}$ in the integrand of Eq. (6.4) we use data provided by the A1 collaboration fit [100] to elastic scattering data, where it is provided in terms of the Sachs electric and magnetic form factors for the proton:

$$\begin{aligned} F_2^{(el)}(x,Q^2) &= \frac{[G_E(Q^2)]^2 + \tau[G_M(Q^2)]^2}{1+\tau}\delta\Big(1-x\Big), \\ F_L^{(el)}(x,Q^2) &= \frac{[G_E(Q^2)]^2}{\tau}\delta\Big(1-x\Big), \end{aligned} \tag{6.6}$$

and $\tau = Q^2/(4m_p^2)$. Noteworthy, is the fact that the fits from A1 show an apparent divergence from the widely used dipole approximation ($G_E(Q^2) = G_M(Q^2)/\mu = (1+Q^2/0.71)^{-2}$, where $\mu = 2.79$ is the proton magnetic moment and the expression for both Sachs factors is obtained from empircal measurements, fitting to the form obtained by expanding the plane wave scattering cross section form to $\mathscr{O}(1/Q^2)$). The fits differ from the dipole model by about 10% at $x \sim 0.5$ (where as $x \to 1$, the divergence is seen to increase but has little effect due to the effective kinematic cut at high x, discussed below). However, as discussed in [19], the dipole model's reasonably good ($\mathscr{O}(5\%)$) correspondence to the data at low x makes it useful in interpreting the scaling behaviour in this region ($\gamma^{(el)}(x) \sim \alpha\ln(1/x)$).

We anticipate the discussion of the purely elastic photon contribution in Section 6.4 by providing an explicit formula for $\gamma^{(el)}$ from the direct substitution of Eq. (6.6) into Eq. (6.4) to obtain:

$$\begin{aligned} x\gamma^{(el)}(x,\mu^2) = \frac{1}{2\pi\alpha(\mu^2)x}\int_{\frac{x^2m_p^2}{1-z}}^{\mu^2}\frac{dQ^2}{Q^2}\alpha^2(Q^2)\Bigg[\Bigg(xP_{\gamma,q}(x) + \frac{2x^2m_p^2}{Q^2}\Bigg)\times \\ \frac{[G_E(Q^2)]^2 + \tau[G_M(Q^2)]^2}{1+\tau} - x^2\frac{[G_E(Q^2)]^2}{\tau}\Bigg]. \end{aligned} \tag{6.7}$$

We also make note of the $1/\alpha(\mu^2)$ term outside of the integral and observe that when expanding the left hand side of Eq. (6.7) in terms of $\alpha(Q^2)^2/\alpha(\mu^2)$, the scaling behaviour that arises from the leading order $P_{\gamma\gamma}$ splitting kernel in the evolution is contained within this expression.

For $F_{2,L}^{(inel)}$, further considerations must be made with regards to its contribution in Eq. (6.4). In particular, it is known from DIS experiments that as a function of the total momenta of the outgoing hadronic products (denoted with the standard DIS variable $W^2 = (Q^2(1-x)/x) + m_p^2$), $F_{2,L}^{(inel)}$ displays two distinct modes of behaviour. For $W^2 \gtrsim 4$ GeV^2 (denoted as the "continuum" region), $F_2^{(inel)}(W^2)$ is seen to be relatively smooth at various observed values of Q^2. At $W^2 \lesssim 3$ GeV^2 (denoted as the "resonance" region) meanwhile, $F_2^{(inel)}(W^2)$ is seen to display various Breit-Wigner type resonances due to hadronic excited states (such as the Δ and associated modes). To fit to both of these regions, two different fits are used above and below a threshold of $W_{cut}^2 = 3.5$ GeV^2. For the continuum region ($W^2 \geq W_{cut}^2$) contributions to $F_{2,L}$ are modelled from data from the HERMES GD11-P [101] fit, while the resonance region ($W^2 < W_{cut}^2$) is modelled using data from the CLAS collaboration [102].

The HERMES collaboration provides data for F_L by relating it to the available data for F_2. In particular, by considering the parameter $R = \sigma_L/\sigma_T$, the ratio of the longitudinal and transverse polarisation cross sections, the two structure functions are related in the following manner:

$$F_L(x,Q^2) = \left(1 + \frac{4m_p^2x^2}{Q^2}\right)\frac{R(x,Q^2)}{1+R(x,Q^2)}F_2(x,Q^2), \tag{6.8}$$

where the function $R(x,Q^2)$, following the approach taken by HERMES [101], is adapted from the E143 collaboration fit, R_{1999} [103]. Although only F_2 data is provided by the CLAS fit, F_L is estimated in the resonance region by using Eq. (6.8), with the same form of $R(x,Q^2)$ provided by HERMES.

As discussed in Section 8.3, a comparison is made to the Cristy-Bosted [104] fit for F_2 in the resonance region and the difference with CLAS is taken as a model for the uncertainty due to this contribution. Similarly, since there is an inherent ambi-

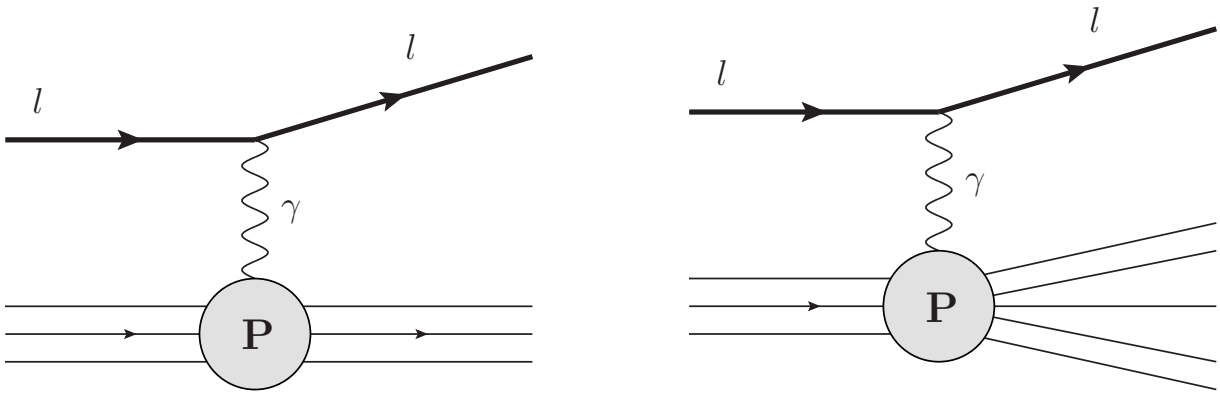

Figure 6.1: Leading order representations of elastic (left) and inelastic (right) Neutral Current DIS processes. In the former, the proton is seen to remain in tact post scattering, while in the latter it dissociates (and undergoes hadronisation) and one interprets the lower vertex with the hadronic tensor $W_{\mu\nu}(p,q)$, which may be reformulated in the context of the parton model (see [19][99] for a more detailed discussion). As demonstrated by LUXqed, the photon (γ) lines on the left and right, which serve as probes of $F_{2,L}^{(el)}$, $F_{2,L}^{(inel)}$ respectively, may be interpreted as the $\mathcal{O}(\alpha)$ representation of $\gamma^{(el)}$, $\gamma^{(inel)}$, as discussed in Section 6.4.

guity in the W^2_{cut} value above and below which resonance and continuum behaviour is chosen to be characterised by the two data sets, rather than perform a smoothing operation (such as in Eqs. 8.10 of [99]), we vary W^2_{cut} and take the resulting change as an independent source of uncertainty (discussed in Section 8.3).

Since the structure functions themselves exhibit enhanced sensitivity to particular effects at lower starting scales (1 GeV in the MMHT framework, in comparison to 10 GeV adopted by LUXqed) such as proton mass corrections $\mathcal{O}(\frac{m_p^2}{Q^2})$ and higher twist terms, modifications are made to the evolution to account for these during the evolution, as discussed in Section 6.3.

Finally, we note that the lower bound of the Q^2 integral, $\frac{x^2 m_p^2}{1-z}$, introduces an effective cut on all photon contributions above a certain point in x. In particular, by noting that the integral in z is bounded by x, at the limits of the integral the following inequality is imposed:

$$Q^2 \geq \frac{x^2 m_p^2}{1-x}, \tag{6.9}$$

which may be rearranged to express an effective upper limit on x for $x\gamma(x,Q^2)$:

$$x \leq \frac{-Q^2 + Q\sqrt{Q^2+4m_p^2}}{2m_p^2} \equiv x_{cut}, \tag{6.10}$$

such that all contributions above this point in x are kinematically invalid and are therefore identically 0 for $x > x_{cut}$. Note that since the expression at input, Eq. (6.4) is valid at all scales (Q^2), we have generalised the discussion to consider all stages of the evolution. As $Q \to \infty$, $x_{cut} \to 1$ and this constraint disappears (e.g at $Q^2 = 10$ GeV^2, $x_{cut} = 0.918$). However, at our starting scale, which as noted involves a parameterisation at scales lower than that of other contemporary photon PDFs, $x\gamma(x,Q_0^2)$ has an effective cut imposed on it at $x_{cut} \simeq 0.62$, eliminating all high x contributions.

In particular, the cut described in Eq. (6.10) is applied during the evolution. As discussed in Section 6.3, this has the effect of dampening not only the leading twist DGLAP contributions, but also the effects of other terms relevant to the photon evolution at high x, such as higher twist and target mass corrections, which are most prevalent at low Q^2. Finally, we make note of the fact that the effect of this cut is another independent source of momentum violation, as discussed in Section 6.5.

6.3 Modifications to DGLAP Evolution

In this section we outline the changes made to our evolution procedure to accommodate the effects of QED. As done previously, in the MMHT framework the QED supplemented evolution of the partons is unidirectional in Q^2 from a starting scale of $Q = 1$ GeV, with the convolution for the partons at each step performed in the standard Bjorken x space. This is in contrast to that of NNPDF3.1luxQED which adopts an iterative process in its fit. The DGLAP evolution of the partons is reversed from $Q = 100$ GeV for a photon produced from the partons at high scales (with an elastic contribution whose expression is adopted from that of LUXqed) for the fit to converge on a consistent starting scale photon, subject to the momentum sum rule

constraint for the partons modified to include the photon (γ):

$$\int_0^1 x(\Sigma(x,Q_0^2)+g(x,Q_0^2)+\gamma(x,Q_0^2))=1, \tag{6.11}$$

where Σ is the total singlet for the quarks. In practice, as shown in section 4, the resulting photon distributions from either approach are in agreement, differing only by a magnitude on the order of the uncertainties. However, due to certain higher twist effects and the procedure adopted for the treatment of our elastic photon distribution, $\gamma^{(el)}$, Eq. (6.11) is not strictly obeyed during the evolution, as discussed further in Section 6.5.

6.3.1 PDF Basis

While Eqs. (4.6)-(4.8) in Section 4.3 reflect the input distribution parameterisations, a different and distinct linear combination of the partons are involved in the evolution procedure itself. Previously in the MMHT framework, the pure QCD DGLAP evolution of the partons, at all orders, was performed in a basis that was chosen to be computationally efficient for performing convolutions. This involved a decoupling of the partons into a singlet (consisting of the gluon and flavour combinations of quark and antiquark distributions) and non-singlet distributions which are evolved separately.

The linearly independent combinations of partons that were evolved consisted of the following singlet (in the space of quark flavours) combinations:

$$\Sigma_L = u+\bar{u}+d+\bar{d}+s+\bar{s}, \tag{6.12}$$

$$c+\bar{c}, \qquad\qquad b+\bar{b}, \tag{6.13}$$

$$g \tag{6.14}$$

and the following non-singlet combinations:

$$u_V+d_V = u-\bar{u}+d-\bar{d}, \tag{6.15}$$

$$u+\bar{u}-\frac{\Sigma_L}{3}, \qquad -(s+\bar{s})+\frac{\Sigma_L}{3}, \tag{6.16}$$

$$\frac{d_V-u_V}{2}, \qquad (s-\bar{s})-\frac{u_V+d_V}{2}, \qquad (c-\bar{c})-\frac{u_V+d_V}{2}, \qquad (b-\bar{b})-\frac{u_V+d_V}{2}. \tag{6.17}$$

The subscript L in Σ_L denotes the fact that the singlet consists only of the light quarks. The charm and bottom singlet distributions (Eq. (6.13)) are evolved separately since they only become non-zero near the relevant mass thresholds for production ($2m_c, 2m_b > Q_0$). When considering QCD in isolation, the $SU(n_f)$ flavour invariance of the splitting kernels allows such distributions to be evolved consistently.

As described below, the introduction of QED splitting kernels, $P_{ij}^{(QED)}$, in DGLAP evolution necessarily prohibits such combinations from being used. As mentioned in Chapter 3, in general the splitting kernels are calculated perturbatively in field theory for the relevant gauge group, such as:

$$P_{ij}^{(QCD)} = \frac{\alpha_S}{2\pi}P_{ij}^{(1,0)} + (\frac{\alpha_S}{2\pi})^2 P_{ij}^{(2,0)} + (\frac{\alpha_S}{2\pi})^3 P_{ij}^{(3,0)} + ... \tag{6.18}$$

where the first superscript denotes the perturbative order in field theory at which the splittings are calculated. Recent theoretical developments [20][21] enable the terms

$$P_{ij}^{(QED)} = \frac{\alpha}{2\pi}P_{ij}^{(0,1)} + \frac{\alpha\alpha_S}{(2\pi)^2}P_{ij}^{(1,1)} + (\frac{\alpha}{2\pi})^2 P_{ij}^{(0,2)} + ... \tag{6.19}$$

to be used in the QED supplemented evolution. Here, the first and second superscript indices denote the order in QCD and QED respectively, and the second term in this expansion reflects mixed order splitting kernels.

Since the non-abelian nature of QCD does not manifest at leading order in quark interactions, the majority of the splitting functions in QCD and QED are simply related at this order:

$$P_{qq}^{(0,1)} = \frac{e_q^2}{C_F}P_{qq}^{(1,0)}, \qquad P_{q\gamma}^{(0,1)} = \frac{e_q^2}{T_F}P_{qg}^{(1,0)} \tag{6.20}$$

$$P_{\gamma q}^{(0,1)} = \frac{e_q^2}{C_F} P_{gq}^{(1,0)}, \qquad P_{\gamma\gamma} = -\frac{2}{3}\sum_i e_i^2 \delta(1-y), \tag{6.21}$$

where $C_F = \frac{4}{3}$ and the $T_F = T_R n_F = \frac{1}{2} n_F$ are the colour and trace factors from the $SU(3)$ algebra of QCD. The exception is $P_{\gamma\gamma}$, which accounts for splittings of the form $\gamma \to q\bar{q}$, and differs considerably from the expression for P_{gg}, which as well as $q\bar{q}$ production also includes processes of the form $g \to gg(g)$ at $\mathscr{O}(\alpha_S)$ in QCD.

A further caveat regarding $P_{\gamma\gamma}$ concerns lepton PDFs, which in principle enter amongst the partons discussed so far, due to splittings of the form $\gamma \to l\bar{l}$. More specifically, the limit of the sum n_F denotes the number of active quark flavours available during the evolution. However, technically at any scale $Q^2 > m_l^2$, lepton splittings should also be incorporated into $P_{\gamma\gamma}$, such that the sum over quarks is modified to include the leptons:

$$\sum_i e_i^2 = N_C \sum_q^{n_F} e_q^2 + \sum_l^{n_L} e_l^2. \tag{6.22}$$

In our framework, we neglect the latter term which accounts for leptonic contributions to $P_{\gamma\gamma}$, since the contribution of the photon itself enters as an $\mathscr{O}(\alpha)$ correction to the PDFs, with the lepton contributions at $\mathscr{O}(\alpha^2)$, implying they are extremely suppressed. This was studied more extensively in [105, 106] where it was found that the magnitude of the lepton distributions were many orders of magnitude below those of $x\gamma(x,Q^2)$, with negligible effects on the PDFs at the scales considered in this paper.

However, it should be noted that the LUXqed PDF set [99], to which a comparison is made in Section 8.2, does include this contribution in the DGLAP evolution used to develop their $x\gamma(x,Q^2)$ (though they do not develop distributions for the leptons themselves). Since the right hand side of Eq. (6.21) is a $\delta(1-x)$ term multiplied by a negative coefficient, the extra contributions from the lepton splitting terms in DGLAP are anticipated to slightly reduce the magnitude of a photon whose evolution accounts for them (as one anticipates from the process $\gamma \to l\bar{l}$). We investigate the effect of such a term on the $x\gamma(x,Q^2)$ developed in this thesis in Section 8.2.

Upon inspection of Eqs. (6.20)-(6.21), even at leading order it becomes apparent that the distributions in Eqs. (6.12)-(6.17) cannot be used since QED couplings no longer support flavour symmetry, due to the charge separation of up and down type quarks ($e_u \neq e_d$). Furthermore, one anticipates based on this observation the breaking of isospin symmetry when comparing the valence distributons of the proton and neutron, as discussed in Section 7.2. To accommodate the requirement of charge sensitivity, the partons are now evolved in the following basis, which are separable by charge:

$$q_i^{\pm} = q_i \pm \bar{q}_i, \quad g, \quad \gamma^{(el)}, \quad \gamma^{(inel)}. \tag{6.23}$$

In the following discussion the subscript i denotes any active ($Q > 2m_q$) flavour: $i = u,d,s,c,b$ and the +/- superscript denotes the singlet and non-singlet quark distributions respectively. The gluon and photon components, g, $\gamma^{(el)}$ and $\gamma^{(inel)}$ are then evolved individually in the flavour space of the partons.

Although the basis given in Eq. (6.23) is compatible with a joint evolution in QCD and QED, they require some modification to the form of DGLAP splitting kernels used. Adopting the notation introduced in Chapters 3 and 4, $t = \ln\left(Q^2\right)$ and $(f \otimes g)(x) = \int_x^1 \frac{dy}{y} f\left(\frac{x}{y}\right) g(y)$, the non-singlet distributions described in Eqs. (6.15) - (6.17) may be evolved in the following way in pure QCD:

$$\frac{\partial q_i^{NS}}{\partial t} = P_{q_i}^{-} \otimes q_i^{NS}, \tag{6.24}$$

where the expression for $P_{q_i}^{-}$ may be found in Eqs. (4.94) to (4.108) of [108]. The simplicity of this equation arises from the fact that symmetry allows for evolution of the q_i^{NS} distributions to be diagonal in quark flavour space, such that only the term $P_{q_i}^{-}$, which describes the diagonal elements of the quark-quark and quark-antiquark splitting functions, is required.

The evolution for the q_i^{-} requires an additional component since although they are also non-singlet functions of the quarks, the non-diagonal elements in flavour space become necessary to the evolution:

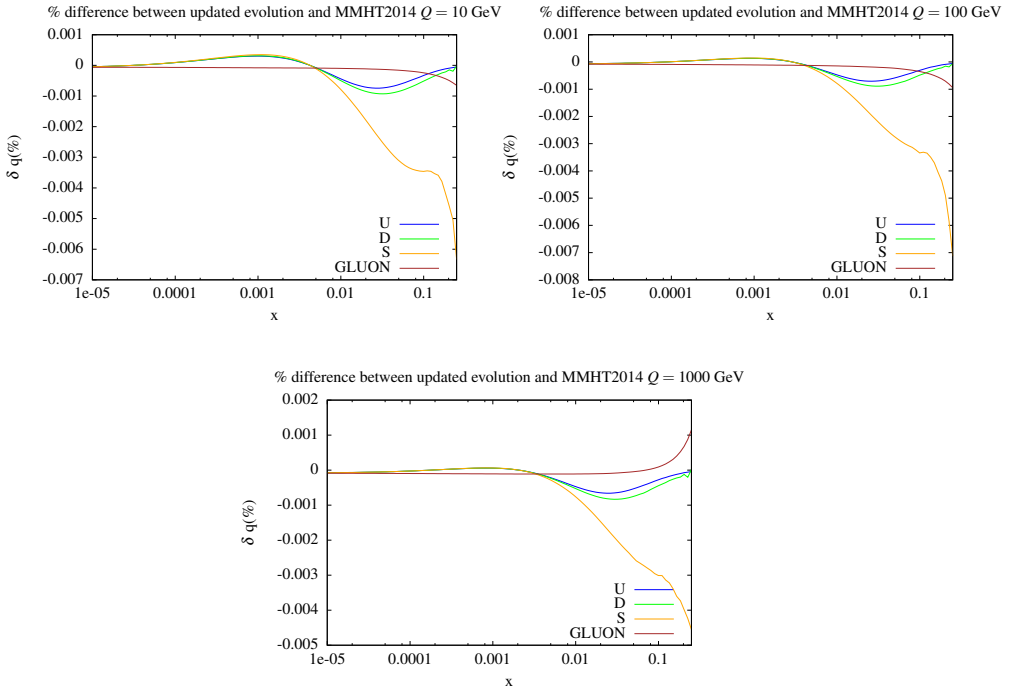

Figure 6.2: The percentage changes between the updated pure QCD NNLO partons (with the ΔP^S term shown in Eq. (6.25) and corrections to the evolution at the heavy quark mass thresholds) and the MMHT2014 partons.

$$\frac{\partial q_i^-}{\partial t} = P_{q_i}^- \otimes q_i^- + \sum_{j=1}^{n_F} \Delta P^S \otimes q_j^- , \tag{6.25}$$

where ΔP^S becomes non-zero at NNLO ($\mathcal{O}(\alpha^3)$) in QCD and n_F is the number of active quarks in the evolution.

Note that this sum over valence-like non-singlet distributions corresponded to Eq. (6.15) in the original MMHT framework, which neglected the strange, charm and bottom distributions due to their small relative size. With the release of the set described in this thesis, the contribution from these off-diagonal splittings for all flavours are now included, which represent minor changes, $\mathcal{O}(10^{-5})$, in a like-for-like comparison with the original MMHT partons purely in QCD (as discussed in Section 6.1), as shown in Fig. 6.2.

Also included in this figure are minor improvements that were made to the procedure for adding in the charm and bottom distributions to the evolution at the appropriate energy thresholds. At NNLO, the distributions appeared to be brought in

slightly prematurely creating a small inaccuracy when interpolating between the Q^2 points used in the Gaussian-Legendre integration, an issue that was highlighted in adapting the procedure for the QED code. In general, as seen in Fig. 6.2, the overall corrections to the evolution procedure result in changes of less than $\sim 0.01\%$ over a broad range in x, with the largest magnitude of change being at high x where the relative uncertainties on the partons are large. Though of little practical significance (as indicated in Fig. 6.2) this has now been corrected.

6.3.2 Target Mass and Higher Twist Corrections

As previously noted, MMHTqed differs in its production of a photon PDF from other contemporary sets in adopting a straightforward evolution in Q^2 space, from a starting scale of $Q_0 = 1$ GeV. However, at low scales such as these, target mass corrections, which account for the finite mass of the proton, and higher twist[1] terms have non-negligible contributions to $F_{2,L}$. Above Q_0, the $F_2^{(inel)}$ contributions to $\gamma^{(inel)}$, as in Eq. (6.4), are modelled by the parton splittings in DGLAP, which require some modification to capture the relevant behaviour at high x.

The target mass corrections for the proton are well known, modifying the $\mathcal{O}(\alpha)$ quark to photon splitting in an identical manner to the first term in the integrand of Eq. (6.4):

$$P_{\gamma,q}^{(0,1)}(z) \to P_{\gamma,q}^{(0,1)}(z) + \frac{2x^2 m_p^2}{zQ^2}. \tag{6.26}$$

Further modifications are also required for higher twist terms which lead to discrepancies between F_2 as calculated from the partons and experimental measurements for $F_2^{(inel)}$, due to non-perturbative effects at high x and low Q^2. To eliminate this concern when comparing to DIS data in a global fit to constrain the parton parameters, kinematic cuts of $W^2 > 15$ GeV^2 (and $W^2 > 20$ GeV^2 at LO) are normally imposed on the data to exclude such regions [109] (as discussed in section 5.1 of

[1]Here, higher twist refers to the fact that when using the factorisation theorem to separate the short and long scale physics of QCD and to develop the parton model, strictly speaking we neglect further contributions to the proton scattering cross section beyond those of single parton interactions, suppressed by factors of λ/Q where $\lambda \sim \Lambda_{QCD}$. Higher twist terms, $\mathcal{O}(\lambda^2/Q^2)$ and above, represent low scale corrections to the parton model, where details of this expansion may be found in [107].

[79]). For reasons discussed below those data sets relating to $\nu(\bar{\nu})N$ experiments to measure xF_3 have a more stringent cut of $W^2 > 25$ GeV^2 imposed.

For the evolution of $\gamma^{(inel)}$ in DGLAP, which is sensitive to $F_2^{(inel)}$ in the region discussed, a phenomenological model must be adopted to compensate for this difference. For our purposes, we employ that of Dasgupta and Webber [110], who provide non-perturbative power corrections to the structure functions in powers of $\frac{1}{Q^2}$ by characterising the associated infrared divergences in field theory with a "renormalon". In this thesis we shall use the term renormalon synonymous with higher twist corrections of this type. In [110], they provide at $\mathcal{O}(\frac{1}{Q^2})$ a modification to F_2 that accounts for the change due to renormalon calculations at high x, seen to give a better description of data from DIS experiments [111].

In lieu of $F_2^{(inel)}$, during the evolution the contributions to $\gamma^{(inel)}$ are essentially handled by the quark splittings ($q \to q\gamma$), where the total charge-weighted quark singlet Σ (the sum of Eqs. (6.12)-(6.13)) plays the role of F_2 in Eq. (6.4). Therefore, to approximate renormalon effects during the evolution, these modification are instead made to the quarks, as passed to the splitting functions at all orders for $P_{\gamma,q}^{(QED)}$, in the following way:

$$q(x,Q^2) \to q(x,Q^2)\Big(1 + \frac{A_2'}{Q^2}\int_x^1 \frac{dz}{z} C_2(z) q(\frac{x}{z},Q^2)\Big), \tag{6.27}$$

where A_2' is a parameter not given a priori by the theory and $C_2(z)$ is defined in Eq. 4.1 of [110], and conserves the flavour number properties of the various $q(\frac{x}{z},Q^2)$. As such, higher twist contributions to F_2 do not contribute to the Adler sum rule, i.e. $\int_0^1 dx\ F_2^{HT}(x,Q^2) = 0$, which enforces sensible behaviour as $x \to 0$. However no such restriction applies to F_3, and renormalon calculations [114] imply that they become large, necessitating the need for the more stringent cut on F_3 data used in the fit (from the CHORUS collaboration [145]) that extend into this region.

This is of interest because the parameter A_2' is not well determined, and in [110], is fit loosely to structure function data to yield a value of $A_2' = -0.2$ GeV^2. As discussed above, data sensitive to renormalon contributions are typically excluded in the fit due to the inability to model them accurately from the partons.

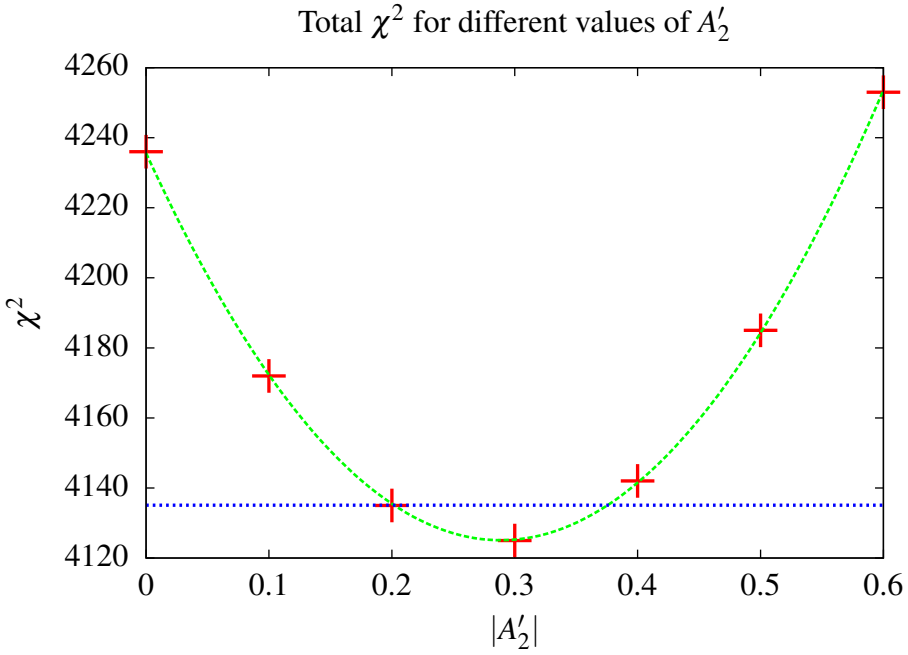

Figure 6.3: The χ^2 values obtained in a global fit, with kinematic constraints on DIS data lowered to $W^2 = 5$ GeV^2, with different values of A_2' in the renormalon calculations for F_2 and F_3. The dashed blue line represents a $\Delta\chi^2 = 10$ variation from the minimum to establish an uncertainty band on A_2'.

However, for the purpose of determining a value of A_2' to use in Eq. (6.27), we relaxed these constraints, lowering the threshold to $W^2 > 5$ GeV^2 and modified F_2 and F_3 as calculated in the global fit to data, to include the relevant renormalon contributions at $\mathcal{O}(\frac{1}{Q^2})$, as outlined in [110] (i.e. with modifications of the form shown in Eq. (6.27)). We then tested a variety of different values as shown in Fig. 6.3 and compared each value with the fit quality to determine a value for A_2'. Our central value is taken as $A_2' = -0.3^{+0.1}_{-0.1}$ GeV^2, with uncertainties determined from a generous $\Delta\chi^2 = \pm 10$ variation in the fit (to one significant figure). This is motivated by the dynamical tolerance scheme used in our framework, as outlined in Section 6 of [79] and described in Section 4.2 in Chapter 5, where it was found that in order to provide reasonable uncertainties when fitting to many disparate data sets in tension with one another, one typically required tolerances $T = \sqrt{\Delta\chi^2_{global}} \sim 3$ to provide sufficient variation in the generation of 68% C.L. uncertainty bands, rather than the $T = 1$ one would obtain from a standard "parameter-fitting" criterion. This motivates our decision for $\Delta\chi^2 = \pm 10$, which also corresponds to the fixed tolerance

uncertainty schemes adopted by early CTEQ sets [112]. The uncertainty on this is then propagated as an independent source of uncertainty for the photon, as discussed in Section 8.3. This represents a slightly larger renormalon contribution than predicted from [110], though the data are unable to provide significant constraints in either case.

As seen in Fig. 6.4, the target mass corrections lead to a $\sim 3\%$ increase in the photon at high x, while the renormalon contributions, which provide an increasingly positive contribution to F_2 at high x, correspondingly enhances the photon at moderate to high x. Note that the turn around at $x \simeq 0.5$ occurs due to the previously mentioned effective kinematic cut on all photon contributions at high x at low Q^2 (Eq. (6.10)), due to the lower bound of the integral in Eq. (6.4), as discussed in Section 6.2. This itself is also a function of the proton mass m_p, though for our purposes we consider the kinematic cut imposed due to the target mass (i.e. the cut in x) as independent from the term introduced in the evolution and it is seen that the two effects have opposite impacts on the high x photon, with the kinematic cut ultimately dominating. Furthermore, the relative magnitude of both effects is slightly diminished at high Q^2 scales during the evolution due to the $\sim 1/Q^2$ scaling of both effects, as seen in the difference between the curves in Fig 6.4. We note that both the proton mass term and the modification to the quarks in Eq. (6.27) introduce small, independent sources of momentum violation in the evolution, as discussed in Section 6.5.

6.4 Production of separate $\gamma^{(el)}$, $\gamma^{(inel)}$ PDFs

As noted in Section 6.2, the photon PDF actually comprises of two component distributions, $\gamma(x,Q^2) = \gamma^{(el)}(x,Q^2) + \gamma^{(inel)}(x,Q^2)$, which represent photon contributions from elastic and inelastic proton scattering events, respectively. Separating $\gamma^{(el)}$ and $\gamma^{(inel)}$ from one another while consistently performing the evolution for all the partons required certain changes to be made from the standard procedure for performing DGLAP, due to the fact that the generation of $\gamma^{(el)}$ in the evolution is independent of parton splittings, as detailed below.

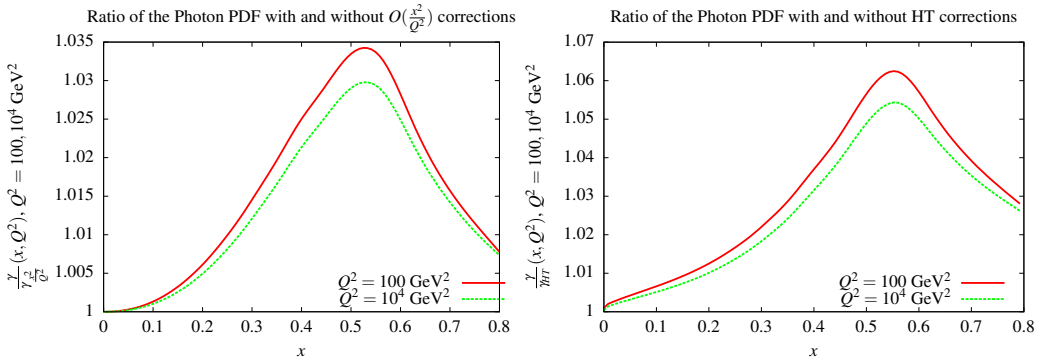

Figure 6.4: (Left) A ratio of the photon PDF with ($\gamma(x,Q^2)$) and without ($\gamma_{x^2/Q^2}(x,Q^2)$) target mass corrections, which when included are seen to increase the photon at high x before the kinematic cut dominates as $x \to 1$. Furthermore, these effects diminish at higher scales, where the corrections become less prevalent in the evolution. A similar but larger effect is seen (Right) in the photon when accounting for the Highter Twist (renormalon) corrections to the quark distributions described above (Eq. (6.27)) which have a tendency to increase the photon PDF upon their inclusion in the photon's evolution.

For $\gamma^{(inel)}$, the evolution is analogous to that of the other partons. The contributions from the HERMES (continuum) and CLAS (resonance) data for $F_2^{(inel)}$ are present only at input, above which the evolution is performed using the splitting kernels. We emphasise that all photon contributions that arise from the splitting of other partons (the quarks, antiquarks and both photon components themselves, but also the gluon at $\mathcal{O}(\alpha\alpha_S)$) in DGLAP are absorbed into the definition of $\gamma^{(inel)}$ (using the notation of the previous section):

$$\frac{d\gamma^{(inel)}}{dt} = \sum_j^{n_F} P_{\gamma q_j} \otimes q_j + \sum_j^{n_F} P_{\gamma \bar{q}_j} \otimes \bar{q}_j + P_{\gamma g} \otimes g + P_{\gamma\gamma} \otimes \gamma^{(inel)}. \tag{6.28}$$

This reflects the fact that scattering processes that are sensitive to the partons are themselves inelastic and that therefore any photon contributions that arise from their evolution in DGLAP are necessarily inelastic contributions.

While $\gamma^{(el)}$ is included at input and passed to the other partons during evolution, its own evolution requires consideration of the contributions it receives above Q_0 from $F_2^{(el)}$, since our expression for $\gamma^{(el)}$ given in Section 6.2, Eq. (6.7), holds generally above the input scale. Incorporating this and splittings of the form $\gamma \to q\bar{q}$

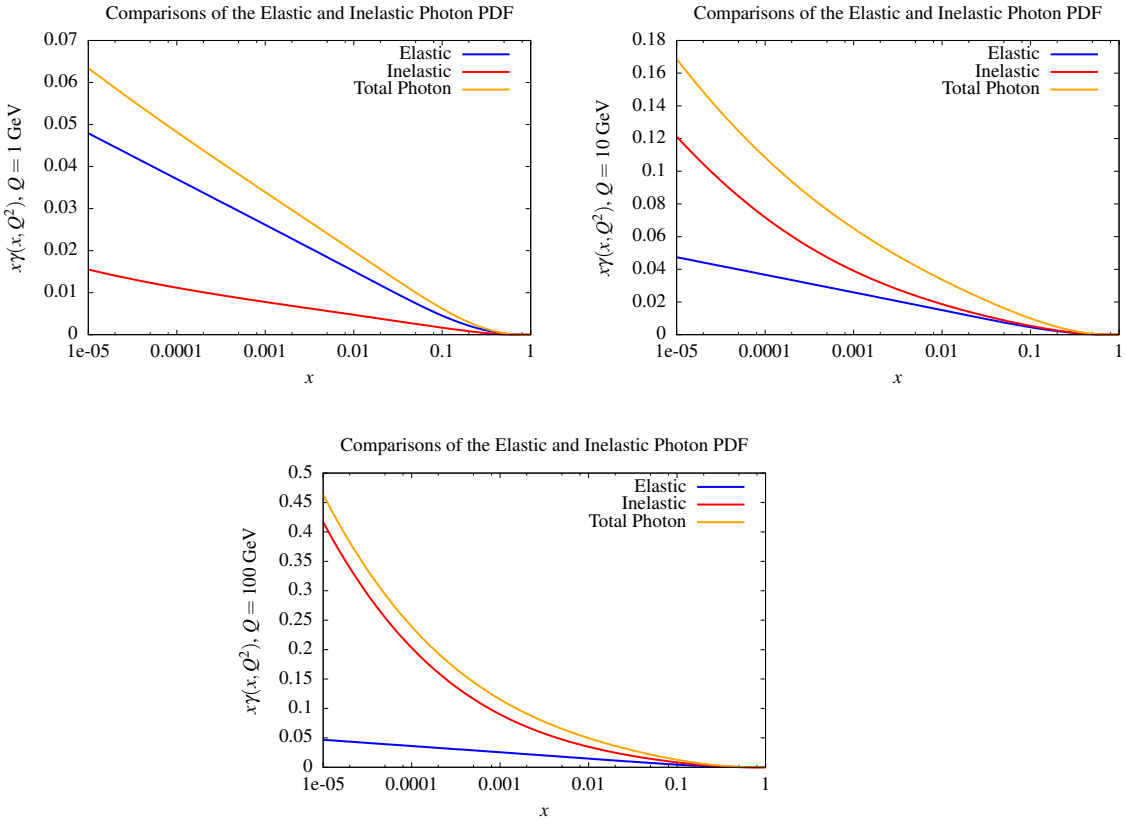

Figure 6.5: The Elastic and Inelastic Photon components at different values of Q. Top left: $Q = 1$ GeV, top right: $Q = 10$ GeV, bottom: $Q = 100$ GeV.

and $\gamma \to q\bar{q}g$ at $\mathcal{O}(\alpha\alpha_S)$, the evolution for $\gamma^{(el)}$ is given as:

$$\frac{d\gamma^{(el)}}{dt} = P_{\gamma\gamma} \otimes \gamma^{(el)} + \delta x\gamma^{(el)}. \tag{6.29}$$

The expression for $\delta x\gamma^{(el)}$ is given by taking the derivative of the expression for the elastic photon, Eq. (6.7), w.r.t Q^2:

$$\delta x\gamma^{(el)}(x,Q^2) = \frac{\alpha(Q^2)}{2\pi}\frac{1}{x}\left[\left(xp_{\gamma,q}(x) + \frac{2x^2m_p^2}{Q^2}\right)\frac{[G_E(Q^2)]^2 + \tau[G_M(Q^2)]^2}{1+\tau} - x^2\frac{[G_E(Q^2)]^2}{\tau}\right]. \tag{6.30}$$

As mentioned previously, the data for $G_E(Q^2)$, $G_M(Q^2)$ are taken from the A1 collaboration fits to data from, which as noted in [19] shows noticeable discrepancy

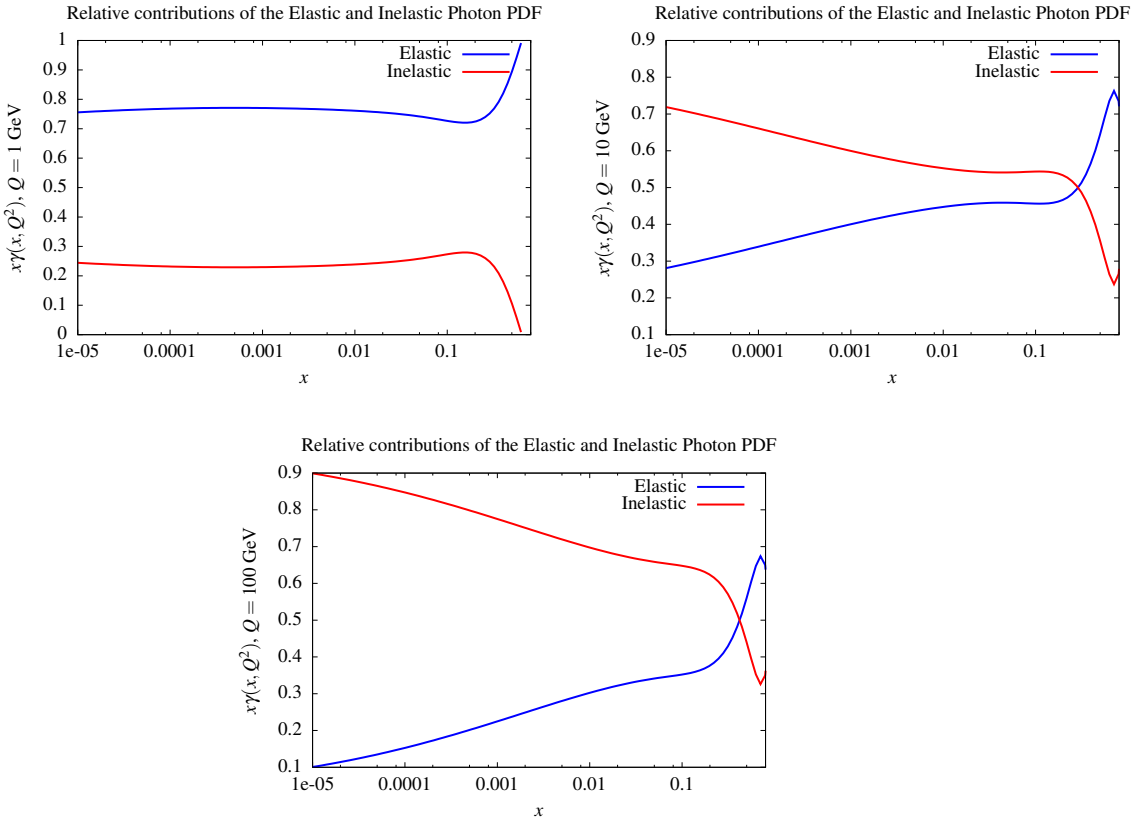

Figure 6.6: The relative contributions of the Elastic and Inelastic Photon components at different values of Q, as fractions of the total $x\gamma$ momentum. Top left: $Q = 1$ GeV, top right: $Q = 10$ GeV, bottom: $Q = 100$ GeV.

from widely used dipole approximation for these functions. As discussed in the next section, including the term introduced in Eq. (6.30) as an external contribution (not generated from parton splittings but added into the evolution from $F_2^{(el)}$ data) introduces a small amount of momentum violation, as do subsequent splittings of the form $\gamma^{(el)} \to q\bar{q}$.

Although the provisions outlined above are needed for the evolutions of $\gamma^{(el)}$ and $\gamma^{(inel)}$, i.e. those contributions from splitting functions of the form $P_{\gamma\{q,\bar{q},g,\gamma\}}$, the treatment for the rest of the partons remains broadly unchanged.

Since the quark, antiquark and gluon contributions from $P_{\{q,\bar{q},g,\gamma\}\gamma}$ splittings do not distinguish between $\gamma^{(el)}$ and $\gamma^{(inel)}$, the entire photon contribution, $\gamma(x,Q^2) = \gamma^{(el)}(x,Q^2) + \gamma^{(inel)}(x,Q^2)$, is passed to the relevant splitting kernels during evolution. Note that for the development of a neutron photon PDF, which is approximated

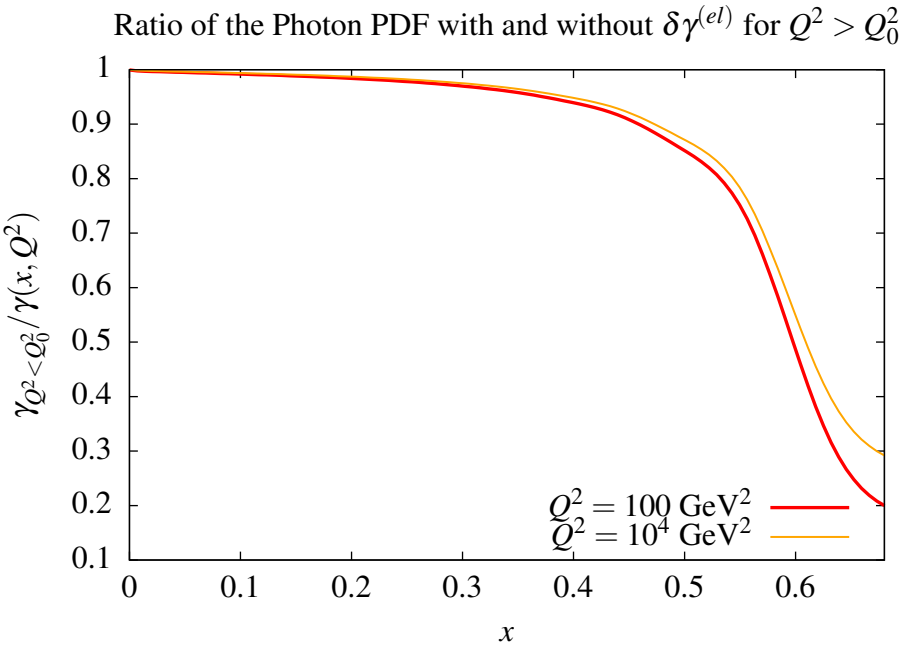

Figure 6.7: The ratio of the $x\gamma(x,Q^2)$ distribution without $\delta x\gamma^{(el)}$ contributions for $Q^2 > Q_0^2$

from the evolution of that in the proton, $\gamma_{(p)}^{(inel)}(x,Q^2)$ is further subdivided in the MMHT framework into components that distinguish between photon contributions that arise from $u,\bar{u} \to u,\bar{u}\gamma$ splittings and $d,\bar{d} \to d,\bar{d}\gamma$ during the evolution. Such bookkeeping will prove to be useful when approximating the effect of the change in flavour content of the neutron's partons on the resultant photon PDF (detailed in Section 7.3).

Since $\gamma^{(el)}$ and $\gamma^{(inel)}$ distinguish between the photon in two distinct categories of scattering processes, there is a phenomenological interest in comparing the two. At input, the elastic contribution dominates over that of the inelastic, as $F_2^{(el)} > F_2^{(inel)}$ in the region $Q \lesssim 1$ GeV, seen in Fig. 6.5. However, evolution quickly enhances the contributions of $\gamma^{(inel)}$, particularly at low x, predominantly due to quark splittings, as shown in Fig. 6.6.

As discussed above, the only contributions $\gamma^{(el)}$ receives during the evolution are those of Eq. (6.30). Since $G_{E,M}(Q^2)$ are known to diminish with increasing Q^2 and $1/\tau \sim 1/Q^2$, an inspection of the form of Eq. (6.30) reveals that it will be of diminishing importance in a significant range of x. In fact, investigating the effects of leaving out this term in Eq. (6.29) entirely yields a $\gamma^{(el)}$ with differences of just

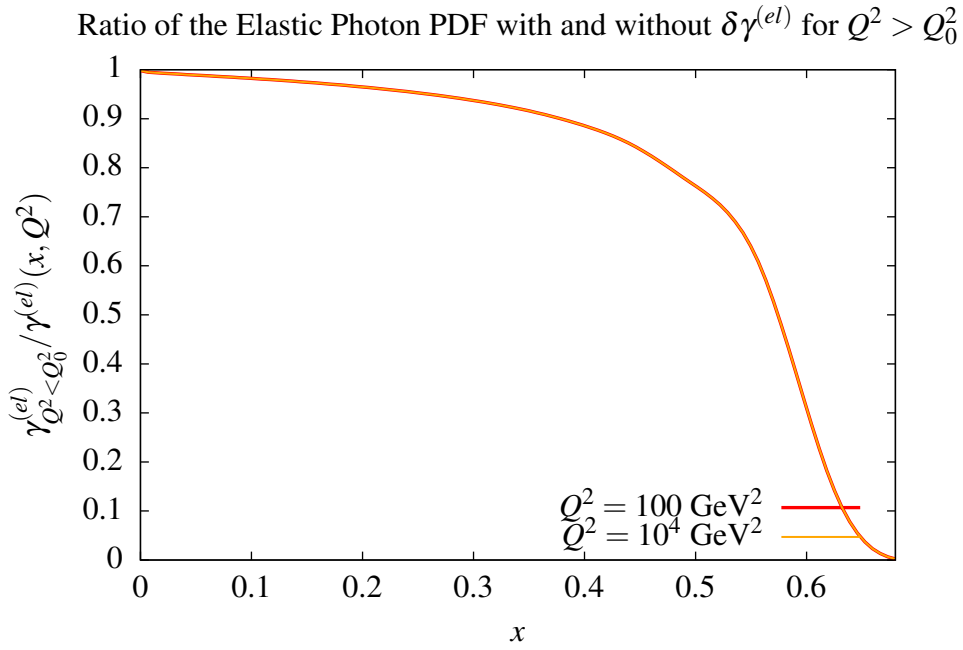

Figure 6.8: The ratio of the $x\gamma^{(el)}(x,Q^2)$ distribution without $\delta x\gamma^{(el)}$ contributions for $Q^2 > Q_0^2$

$\mathcal{O}(10^{-3})$ at low x from the form with the contributions included. One corollary to this is that the elastic distribution's contribution to the overall photon at input is proportionally large at high x, and remains true even at $Q^2 > Q_0^2$ (Fig. 6.6). This is seen in Figs. 6.7 and 6.8, where we investigate the effect of removing the elastic component's contribution during the evolution (leading to significant changes in high x).

However as $\lim_{x\to 1}\gamma^{(el)}, \gamma^{(inel)} \to 0$ and as discussed in Section 8.3, uncertainties are large in this region (see Section 8.3). This makes it difficult to make very strong predictive statements about either distribution in this region.

6.5 Momentum Conservation

In Eq. (6.11), we gave the momentum sum rule, a statement of momentum conservation of the proton's entirety, carried by the partons. The inclusion of QED necessitated that the photon be included in this equation, which naturally leads to a redistribution of momentum in the other partons (explored in Section 8.2) in order to obey Eq. (6.11) at input. However, due to the procedure adopted for the inclusion

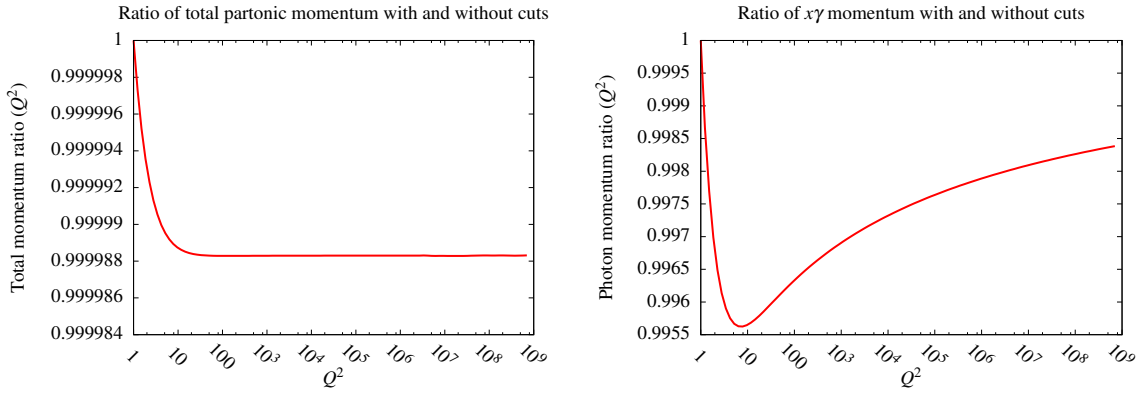

Figure 6.9: (Left) A plot showing the ratio between the total momentum carried by all the partons, at a given point in Q^2 of the evolution with the kinematic cut $Q^2 \geq x^2 m_p^2/(1-x)$ applied to $x\gamma(x,Q^2)$ and without. Since this is effectively a cut on high x contributions, it naturally leads to a reduction in the total momenta carried by the partons. The right plot shows an identical plot but focusing solely on the proportional difference in momenta caused by the photon, where the effects on the evolution are seen to peak at $Q^2 \sim 10$ GeV^2.

of $\gamma^{(el)}$, outlined in the previous section, as well as higher twist terms, this equation is not strictly obeyed during the evolution. This reflects the discrepancy between effects of non-perturbative corrections, such as that of target masses, and the parton model. In this section we outline the consequences of such changes.

First we discuss the effect of a kinematic cut on the photon, as introduced by the lower limit of the integral in Q^2 in the expression for $x\gamma(x,Q^2)$ (Eq. (6.4)), which as discussed in Section 6.2 has the effect of introducing an effective cut on the photon PDF at high x during the evolution. In essence, this removal of photon contributions at high x is a target mass correction (since the cut has a dependence on m_p^2), which is not required to obey the momentum conservation of the partons ordinarily found in DGLAP evolution and therefore introduces small amounts of violation (in the form of a reduction of total momentum carried by the partons) into Eq. (6.11) of $\mathcal{O}(10^{-3}\%)$. This is seen on the left hand side of Fig. 6.9, where we display the ratio of the total momentum of the partons between two versions of the evolution with and without this cut applied.

In particular, the right side of Fig. 6.9 indicates that the reduction to the total momentum carried by the photon ($\int_0^1 x\gamma(x,Q^2)$) is, as anticipated, most strongly

affected by the kinematic cut at low scales until $Q^2 \sim 10$ GeV^2 (with total changes of less than 1%). Since the overall momentum carried by the photon is small during the early stages evolution ($\sim 2-3\times10^{-3}$), where momentum violating effects are most prevalent, this leads to the minuscule amount of change observed in the total momentum of the partons.

Unlike sources of momentum violation concerned in the rest of this section, the cut on the photon entirely eliminates a region of the phase space in which other effects during the evolution may have an effect (since $x\gamma(x,Q^2)=0$ for $x > x_{cut}$). Therefore in the following discussion, when other effects are considered, the magnitude of change they induce to the momentum of the partons is understood as the change in comparison to the evolution in which the cut in x, discussed above, has already been applied, i.e. the basis of comparison assumes that the kinematic cut is active for the remainder of this section (and throughout the thesis, unless mentioned otherwise).

We conclude this chapter with a description of other effects during the evolution which contribute to momentum conservation being obeyed somewhat differently from that of Eq. (6.11). We note that both the inelastic and elastic photons are considered when imposing the momentum sum rule for the parameterisation of the quarks, as in Eq. (6.11), to initialise the PDFs. However, since the elastic photon distribution, $\gamma^{(el)}$, is in some sense external to the proton (it may be probed without the proton's disintegration), its contributions at scales $Q^2 > Q_0^2$, as described in Eq. 6.30, are added independently of the momentum sum rule constraint during evolution since this contribution is not part of the DGLAP evolution.

Although $x\gamma^{(el)}(x,Q^2)$ is included at input when momentum conservation is imposed, contributions to $\gamma^{(el)}$ above input are added independently (as discussed in Section 6.3) at every step in Q^2 during DGLAP evolution. This does not decouple $\gamma^{(el)}$ from the evolution of the quarks, since $\gamma^{(el)} \to q\bar{q}$ splitting are still permissible. However, any γ contribution from the quarks during evolution, e.g. $q \to q+\gamma$ is absorbed into the definition of $\gamma^{(inel)}$. This procedure leads to a small amount of momentum violation during the DGLAP evolution in our framework. In practice,

this effect is negligible, with momentum violating effects of $O(10^{-4})$ observed in the total momentum of the proton during evolution, and in fact stabilises at higher Q^2 where the elastic contribution is less significant, as seen in Fig. 6.10.

Similarly, the proton mass term given in Eq. (6.26) naturally breaks the form of momentum conservation usually obeyed between splitting functions of this type, implied by the equation

$$\int_0^1 x\left[P_{q,q}^{(0,1)}(x)+P_{\gamma,q}^{(0,1)}(x)\right]=0. \tag{6.31}$$

In essence, the proton mass term invalidates this relationship, though in rapidly diminishing amounts as $1/Q^2 \to 0$, leading to changes of $\mathscr{O}(10^{-5})$ in the total momentum carried by the partons.

Likewise, other higher twist terms included in the evolution for the purposes of QED lead to small amounts of momentum violation. Since the quark distributions, $q_i(x,Q^2)$, passed to both $P_{q,q}^{(0,1)}(x)$ and $P_{\gamma,q}^{(0,1)}(x)$ differ due to the inclusion of renormalon corrections for the latter but not the former, this aspect of the evolution also invalidates momentum violation to a small degree, also shown in Fig. 6.10, creating a small amount of violation of $\mathscr{O}(2\times 10^{-5})$.

Overall, even in conjunction, the combined magnitude of momentum violation (the difference between the sum of the parton momenta and the value of 1 suggested by Eq. (6.11)) is still less than 10^{-4}. In practice, this total effect is less than the momentum violation coming from the "leakage" of the partons that occurs due to the fact that the integration range during DGLAP does not strictly begin at 0 for the convolutions of $xf(x/z,Q^2)$ with the splitting functions, which are instead defined in the MMHT framework only to a finite level of precision (defined at a lower bound of $x\sim 10^{-12}$), and is already considered to be of little practical significance. Therefore, we do not consider any of the effects described above as serious invalidations of the parton model, even with the full spectrum of effects due to QED included.

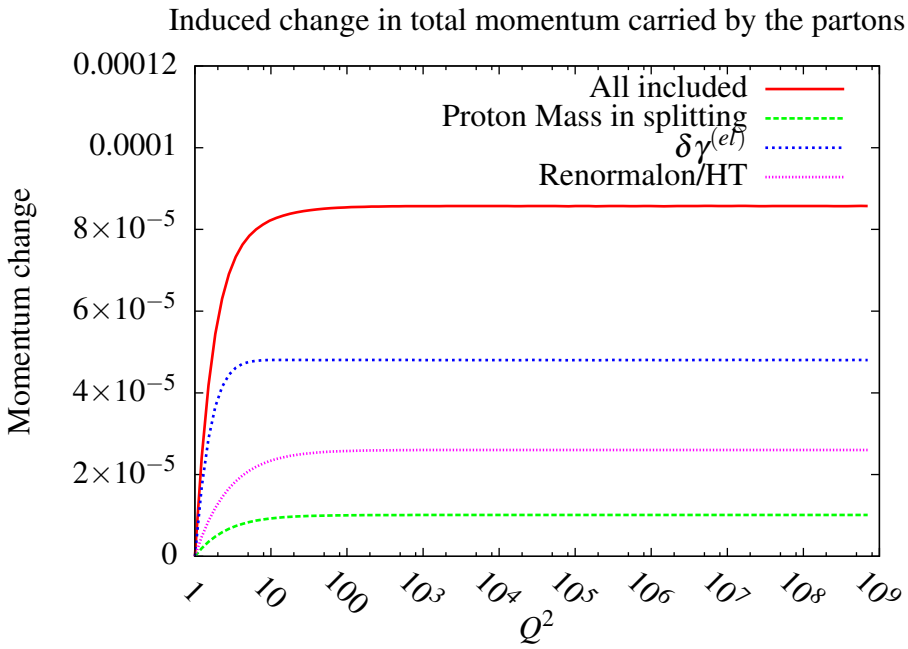

Figure 6.10: The absolute change induced in the total momentum carried by the partons due to the target mass corrections, $\mathcal{O}(m_p^2/Q^2)$, the inclusion of $\delta\gamma^{(el)}$ in Eq. (6.29) (elastic contributions above input) and Highter Twist/Renormalon contributions to $\gamma^{(inel)}$. Note that the magnitude of the change displayed above considers each effect in isolation, with all other momentum violating effects turned off, with the exception of the kinematic cut in the photon at high x, which is considered the baseline of comparison for the change in momentum.

Chapter 7

Neutron

7.1 QED Neutron PDFs

Analogous to that of the proton, the neutron itself is also modelled by its Parton Distribution Functions in DIS experiments and high energy hadron-hadron collisions. When modified by the necessary nuclear correction factors such PDFs are necessary for interpreting the results of deuterium scattering experiments, sensitive to both that of the proton and neutron PDFs, which are used widely in PDF fits for that of the proton.

Since neutron specific data is not as abundantly available at the required precision to constrain the partons, unlike the case of the proton, rather than freely parameterising the input distributions for the neutron and conducting a parallel analysis with an independent DGLAP evolution, the standard practice is to approximate the PDF set of the neutron by relating them to that of the proton. This is much more feasible, since doubling the number of free parameters for the PDFs would leads to considerably difficulty in constraining them from existing data.

The most widely adopted approach is to assume isospin symmetry between hadrons in the valence and sea distributions:

$$u_{V,(p)}(x,Q^2) = u_{(p)}(x,Q^2) - \bar{u}_{(p)}(x,Q^2) = d_{V,(n)}(x,Q^2) = d_{(n)}(x,Q^2) - \bar{d}_{(n)}(x,Q^2), \tag{7.1}$$

$$d_{V,(p)}(x,Q^2) = d_{(p)}(x,Q^2) - \bar{d}_{(p)}(x,Q^2) = u_{V,(n)}(x,Q^2) = u_{(n)}(x,Q^2) - \bar{u}_{(n)}(x,Q^2), \tag{7.2}$$

$$\bar{d}_{(p)}(x,Q^2) = \bar{u}_{(n)}(x,Q^2), \qquad \bar{u}_{(p)}(x,Q^2) = \bar{d}_{(n)}(x,Q^2), \tag{7.3}$$

where the subscripts {(p),(n)} denote the proton and neutron respectively. Furthermore, the $q^{\pm}(x,Q^2)$ as defined in Eq. (6.23) for the s,c and b flavour distributions are assumed to be identical between the proton and neutron. In practice, this is seen to produce a good agreement with the observed data and is well motivated by the $SU(n_f)$ flavour symmetry of QCD as well as the fact that the evolution treats both quark flavours as essentially massless ($m_u^2/Q^2, m_d^2/Q^2 \sim 0$ for $Q > 1$ GeV). However, as discussed in Section 6.3, QED splitting kernels such as those in Eqs. (6.20), (6.21) no longer uphold this symmetry and are expected to generate $\mathcal{O}(\alpha)$ violations in Eq. (7.1).

Therefore, to relate the distributions of the proton to those of the neutron in a manner consistent with QED evolution, one needs to carefully account for the effects of the relevant quark charges e_u, e_d in the evolution and to allow for small amounts of isospin violation to be introduced.

7.2 Adapting DGLAP Evolution for Isospin Violating Hadrons

The primary assumption adopted in MMHTqed is that terms relating to the violation of isospin arise from the introduction of QED splitting kernels, $P_{i,j}^{(QED)}$. By violation, it is meant that at a given x and Q^2 point, the valence distributions can no longer be related to one another by Eqs. (7.1)-(7.3). Any modification to these relations must still preserve the flavour quantum numbers of the proton and neutron upon summation of the relevant valence distribution, reproduced here for convenience:

$$\begin{aligned} \int_0^1 u_{V,(p)}(x)\mathrm{d}x &= \int_0^1 d_{V,(n)}(x)\mathrm{d}x = 2, \\ \int_0^1 d_{V,(p)}(x)\mathrm{d}x &= \int_0^1 u_{V,(n)}(x)\mathrm{d}x = 1. \end{aligned} \tag{7.4}$$

Above input, one can in principle keep track of all contributions to the quarks from splittings generated from QED. In the case of the valence distributions, the evolution is governed by Eq. (6.24), where the splitting kernels are separable as $P_{i,j} = P_{i,j}^{(QCD)} + P_{i,j}^{(QED)}$. Therefore, one can distinguish between two contributions to the valence distributions in the proton, (u_V, d_V, which will be referred to generically as q_V in the following discussion):

$$q_V(x,Q^2) = q_V^{(QCD)}(x,Q^2) + q_V^{(QED)}(x,Q^2), \tag{7.5}$$

where $q_V^{(QED)}$ is defined as:

$$q_V^{(QED)}(x,Q^2) = \int_{Q_0^2}^{Q^2} \frac{\alpha(\mu^2)}{2\pi} \frac{d\mu^2}{\mu^2} \Big(P_{q_i}^{-(QED)} \otimes q_V\big(\frac{x}{z}, \mu^2\big) \Big), \tag{7.6}$$

and the integrand bears resemblance to Eq. (6.24), essentially containing all QED splitting contributions for the valence distributions. In order to achieve this, two distinct columns are separated in the evolution to distinguish between the contributions in Eq. (7.5), which are only evolved by the relevant splitting functions. However, analogous to the total photon distribution in Section 6.4, wherever needed, the entire distribution in Eq. (7.5) is passed within the evolution.

An implicit total proportionality to the QED flavour charge of the quark, $e_{q_i}^2$, is contained in $P_{q_i}^{-(QED)}$. To parameterise the isospin violating components that must be related between the proton and the neutron, we define:

$$\begin{aligned} \Delta d_{V,(n)}(x,Q^2) &= d_{V,(n)}(x,Q^2) - u_{V,(p)}(x,Q^2), \\ \Delta u_{V,(n)}(x,Q^2) &= u_{V,(n)}(x,Q^2) - d_{V,(p)}(x,Q^2), \end{aligned} \tag{7.7}$$

where naïve pointwise isospin would lead both these expressions to evaluate to 0. In the QED framework for the neutron, it is assumed:

$$\Delta d_{V,(n)}(x,Q^2) \propto u_{V,(p)}^{(QED)}(x,Q^2), \qquad \Delta u_{V,(n)}(x,Q^2) \propto d_{V,(p)}^{(QED)}(x,Q^2). \tag{7.8}$$

In particular, it is assumed that provided that the quantum number and mo-

mentum conservation rules (Eqs. (6.11), (3.22)) are obeyed by the constant of proportionality, the only further step needed in relating the valence distributions of the proton to that of the neutron is the charge re-weighting of the relevant $q_{V,(p)}^{(QED)}$, to correct for charge proportional terms in the evolution. Then, we may rewrite Eq. (7.7) in the form of the following equations:

$$\Delta d_{V,(n)}(x,Q_0^2) = \varepsilon\Big(1-\frac{e_d^2}{e_u^2}\Big)u_{V,(p)}^{(QED)}(x,Q_0^2), \tag{7.9}$$

$$\Delta u_{V,(n)}(x,Q_0^2) = \varepsilon\Big(1-\frac{e_u^2}{e_d^2}\Big)d_{V,(p)}^{(QED)}(x,Q_0^2), \tag{7.10}$$

where ε is fixed to conserve momentum at input.

Since the separation of $q_V^{(QCD)}$ and $q_V^{(QED)}$ is only practically possible above the evolution scale, the contribution at input is extrapolated backwards from the first step of the evolution. In order to satisfy momentum conservation, Eq. (6.11), at input for the neutron, one needs the neutron photon distribution at input, which is described in Section 7.3. Once given, the constant of proportionality, ε, is given by:

$$\varepsilon = \frac{\int_0^1 dx x(\gamma_{(p)}(x)-\gamma_{(n)}(x))}{\int_0^1 dx x(\frac{3}{4}u_{V,(p)}^{(QED)}(x)-3d_{V,(p)}^{(QED)}(x))}, \tag{7.11}$$

where all the distributions are evaluated at $Q_0^2 = 1$ GeV^2. This follows a procedure similar to that adopted in [12].

This expression implicitly depends on the assumption that the remaining partons are then related to one another in the standard manner, assuming that the anti-quark (or sea) distributions are still well approximated by

$$(\bar{u})_{(n)}(x,Q_0^2) = (\bar{d})_{(p)}(x,Q_0^2), \qquad (\bar{d})_{(n)}(x,Q_0^2) = (\bar{u})_{(p)}(x,Q_0^2), \tag{7.12}$$

and all other quark flavours and the gluon being related identically between hadrons.

Using Eqs. (7.9) and (7.10) the u and d singlet distributions are then related to one another between hadrons by:

$$(d+\bar{d})_{(n)}(x,Q^2) = (u+\bar{u})_{(p)}(x,Q^2) + \Delta d_{V,(n)}(x,Q^2), \tag{7.13}$$

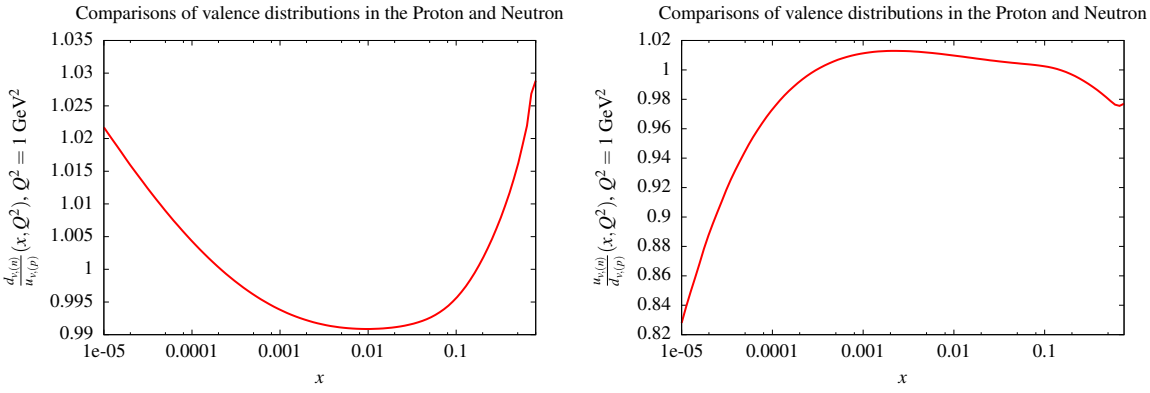

Figure 7.1: The ratio of valence quarks, related to one another by isospin, of the neutron to that of the proton at the input scale $Q_0^2 = 1$ GeV^2. On the left is $u_{V,(n)}/d_{V,(p)}$, and on the right is $d_{V,(n)}/u_{V,(p)}$, both as functions of x.

$$(u+\bar{u})_{(n)}(x,Q^2) = (d+\bar{d})_{(p)}(x,Q^2) + \Delta u_{V,(n)}(x,Q^2), \tag{7.14}$$

where $\Delta\{d,u\}_{V,(n)}$ are as defined above. Though of less apparent interest, these relations pertain to the discussion in Section 7.3, where the neutron photon PDF is considered as primarily sensitive to distributions of the type $q+\bar{q}$ during the evolution. In anticipation of this, we note that $\Delta\{d,u\}_{V,(n)}$ lead to differences between the isospin related u and d singlet distributions between hadrons of only $\mathscr{O}(1\%)$ (since the Δq_V terms are proportional to the contributions to the valence quarks that arise solely from QED evolution, which are $\mathscr{O}(\alpha)$ suppressed). In practice, relating these distributions to one another by isospin still remains a good approximation, which will underpin our development of a photon PDF of the neutron in the next section.

For the valence distributions, in practice, the magnitude of isospin violation is seen to be a few percent, becoming significant especially at low and high x, where all distributions tend towards 0, as shown in Fig. 7.1. Of note is the fact that the discrepancy between the predicted ratio of valence quarks and the naïve isospin assumption remains at the $\sim 1\%$ level, even for the peak of the valence distributions (at $x \sim \frac{1}{3}$, $x \sim \frac{2}{3}$)). This effect is seen to increase during the evolution, with differences of $\sim 5\%$ at $Q = 100$ GeV^2.

Although the primary interest in this thesis for the development of QED corrected neutron PDFs is to provide a manner of relating the PDFs to deuterium scat-

tering experiments used to constrain the partons, we also wish to highlight the potential relevance of this set in the determination of nuclear PDFs. In particular, the assumption made in modern determination of nuclear PDFs (such as those of EPPS [115] and nCTEQ [116]) when fitting to data is precisely that the u and d quark type distributions in the neutron and proton may be related to one another by assumption of isospin.

With the development of this set, we propose that this assumption need not be applied strictly and that with the introduction of QED in scale dependence, the small amounts of isospin violation shown in Fig. 7.1 may be of relevance when the determination of nuclear PDFs reach the $\mathcal{O}(5\%)$ level. While current determinations do not reach this level of precision, a QED corrected relationship between proton and neutron PDFs may provide better fits to the available data, and is of recent interest given that recent work has begin to adopt quark flavour dependence in fits [117].

7.3 Neutron Photon PDF

In considering the effects of QED on the PDFs of the neutron, one can also consider the appearance of its corresponding photon, $\gamma_{(n)}(x,Q^2)$. At input, the expression for the neutron in the MMHT framework is adapted from that of the proton, Eq. (6.4), with all occurrences of the proton mass, m_p, substituted with that of the neutron and the relevant form factors substituted or approximated in the manner discussed below.

As in the case of the proton, one can consider the contributions to the input as coming from both the inelastic and elastic contributions of the form factors, i.e. the separation of $F_{2,(n)} = F_{2,(n)}^{(el)} + F_{2,(p)}^{(inel)}$ in Eq. (6.4), analogous to the discussion in Section 6.4.

For $\gamma_{(n)}^{(el)}$ at input the Sachs form factors of the neutron $G_{E,(n)}, G_{M,(n)}$ must be adapted from elsewhere, since the form factors, $G_{E,(p)}, G_{M,(p)}$ in Eq. (6.7), provided by the A1 collaboration are provided solely for the proton. Instead, we adopt separate models for $G_{E,(n)}$ and $G_{M,(n)}$. For the former, a phenomenological model

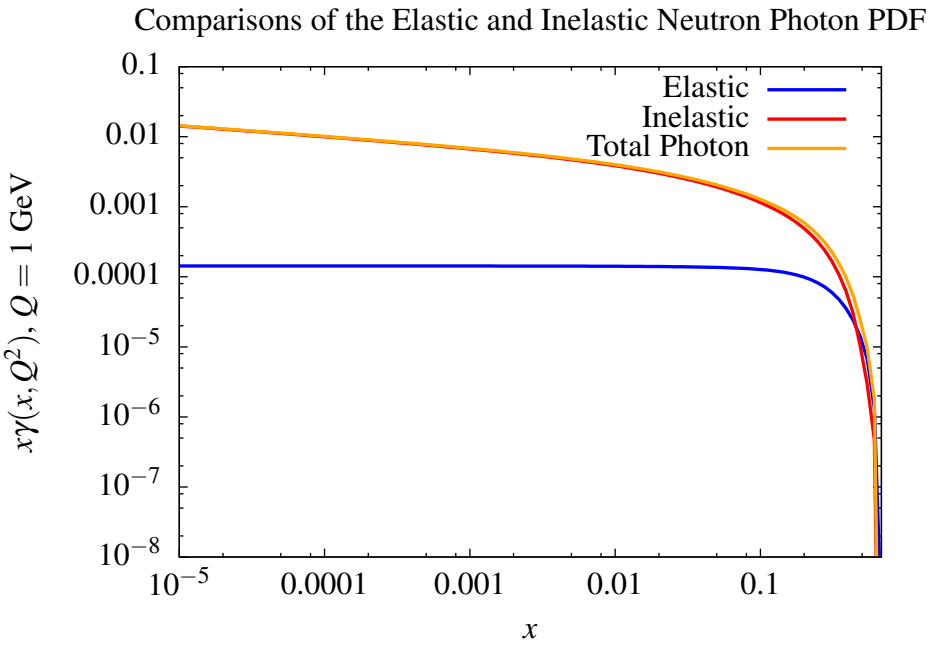

Figure 7.2: The Elastic and Inelastic Photon components at $Q_0^2 = 1$ GeV^2

known as the Galster parameterisation [118] is used:

$$G_{E,(n)} = \frac{A\tau}{1+B\tau} G_D(Q^2), \tag{7.15}$$

where $\tau = Q^2/4m_n^2$ and $G_D(Q^2)$ is the dipole form factor for hadrons (in the form commonly used to approximate $G_{E,(p)}$ when multiplied by the proton's magnetic moment, $G_{E,(p)} = \mu_p G_D(Q^2)$):

$$G_D(Q^2) = \frac{1}{(1+\frac{Q^2}{\Lambda^2})^2}, \tag{7.16}$$

with $\Lambda^2 = 0.71$ GeV^2. Values for A and B are obtained from a fit to data from deuterium and ^3He scattering experiments (e.g. polarised $\vec{D}(\vec{e}e'p)n$ and deuterium quadrupole F_{C2} data), provided by Kelly [119]:

$$A = 1.70 \pm 0.04, \qquad B = 3.30 \pm 0.32. \tag{7.17}$$

For $G_{M,(n)}$ meanwhile, a simple dipole approximation of the form:

$$G_{M,(n)} = \mu_n G_D(Q^2) \tag{7.18}$$

is used. For $Q_0^2 = 1$ GeV^2, Figs. 10 and 13 in a review of nucleon form factors [120] shows this to provide a reasonably good fit ($\mathcal{O}(10\%)$ discrepancy with the data) to data provided from similar deuterium scattering experiments.

Due to the net neutral charge of the neutron, both form factors are significantly smaller in magnitude than those of the proton and one expects that the relevant elastic contribution to $\gamma_{(n)}$ at input to be significantly smaller. In fact, as seen in Figs. 7.2 and 7.3 it is seen to scarcely contribute at all, comprising $\mathcal{O}(1\%)$ of the total over a large range in x, becoming a significant proportion of $x\gamma_{(n)}(x,Q^2)$ only at $x \sim 0.5$, where the magnitude of the PDF itself is of vanishing importance. Therefore, given the uncertainties associated with both models adopted for both the $G_{E,(p)}$ and $G_{M,(p)}$, $\gamma_{(n)}^{(el)}$ may reasonably be omitted for phenomenological purposes. This is even more readily apparent for contributions to $\gamma_{(n)}^{(el)}$ for $Q^2 > Q_0^2$, since the elastic contribution is attenuated as $1/Q^2 \to 0$ such that $\gamma_{(n)}^{(el)}/\gamma_{(n)} \to 0$.

We recall that, following the procedure adopted by LUXqed, $F_2^{(inel)}$ is separated in its contributions to the photon via Eq. (6.4) by two regions separated in the variable $W^2 = (Q^2(1-x)/x) + m_p^2$ with a cut at $W_{cut}^2 = 3.5$ GeV^2. Below this cut, the resonance region, the fit provided by CLAS for $F_2^{(inel)}$ is also given for the neutron, making the resonant region, $W^2 < W_{cut}^2$, trivial to adapt for the purposes of the neutron photon PDF. For the continuum region however, much like the elastic form factors provided by the A1 collaboration, the HERMES fit for F_2 is provided solely for the proton. Therefore, the $F_{2,(n)}^{(inel)}$ is approximated from the expression of that of the proton by relating terms between the PDFs for the neutron and proton. In particular, we re-weight this contribution according to

$$F_{2,(n)}^{(inel)} = r_{F_2} \times F_{2,(p)}^{(inel)}, \tag{7.19}$$

where r_{F_2} is the ratio of the charge weighted singlet of partons Σ, at input for the

Proportions of the Elastic and Inelastic Neutron Photon PDF contributions

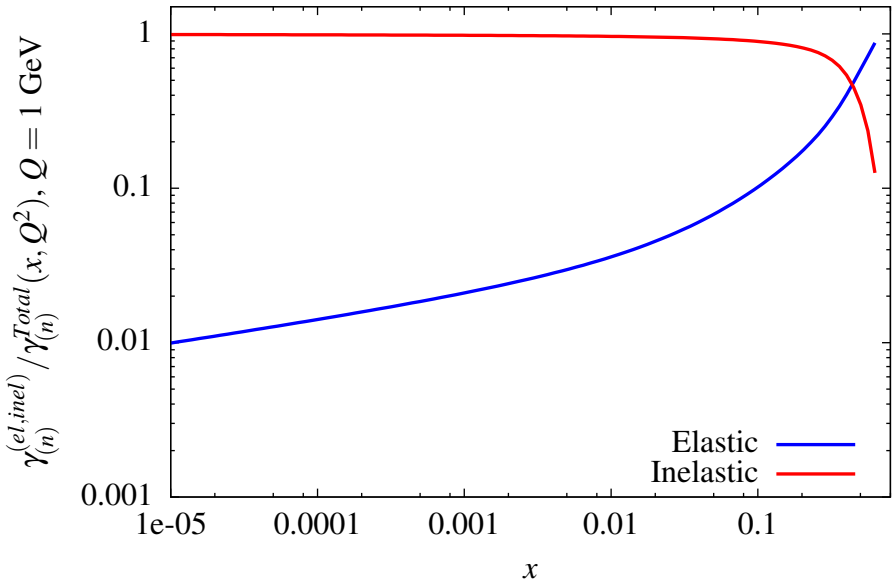

Figure 7.3: The relative proportions of the Elastic and Inelastic Photon component contributions to the total Neutron Photon PDF at $Q_0^2 = 1$ GeV^2

.

neutron to that of the proton:

$$r_{F_2} = \frac{4(d+\bar{d})+(u+\bar{u})+(s+\bar{s})}{4(u+\bar{u})+(d+\bar{d})+(s+\bar{s})}. \tag{7.20}$$

It should be noted that in the expression above, all the distributions refer to those of the proton, where we have used the assumption (which as discussed in the previous section holds to a high degree of accuracy) that $(u+\bar{u})_{(n)} = (d+\bar{d})_{(p)}$, $(d+\bar{d})_{(n)} = (u+\bar{u})_{(p)}$. Note that an attempt to improve the accuracy of the expression in Eq. (7.20) by using Eqs. (7.13), (7.14) would not be feasible in the current framework since those equations depend on the parameter ε from the previous section, which in turn is determined from $\gamma_{(n)}^{(inel)}$ itself.

By approximating the ratio of structure functions between the hadrons by their respective quark singlets, the form of $F_{2,(n)}^{(inel)}$ substituted in Eq. (6.4) for $\gamma_{(n)}^{(inel)}$ in the continuum region at input is simply given as $F_{2,(n)}^{(inel)} = r_{F_2} \times F_{2,(p)}^{(inel)}$. In Fig. 7.4, one sees a broad correspondence between the $r_{F_2}(x)$ and the ratio $\gamma_{(n)}^{(inel)}/\gamma_{(p)}^{(inel)}(x,Q_0^2)$, particularly as $x \to 0$. Some discrepancy between the two plots exists due to the

presence of the resonance region contribution, which as stated above is reformulated based on available neutron data, rather than being re-scaled by r_{F_2}. The general similarity, however, persists because at low x, the behaviour of the light quark singlets is dominated by the sea quarks, and $u \simeq \bar{u} \simeq d \simeq \bar{d}$, such that the effect of swapping flavours via isospin leaves the PDFs roughly invariant in this region.

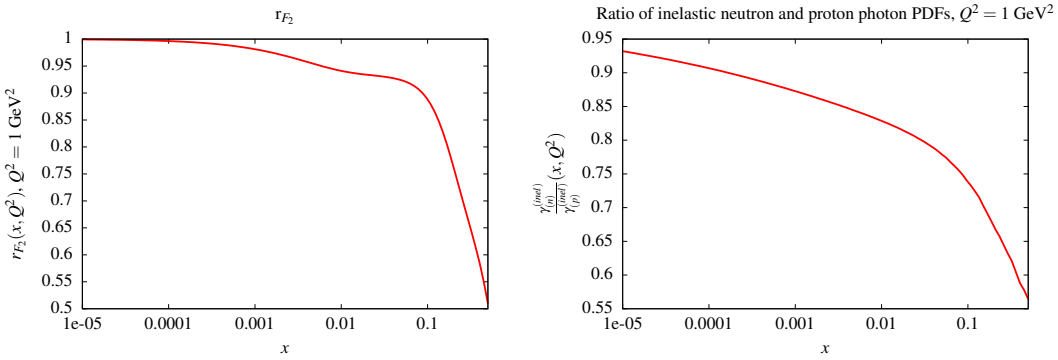

Figure 7.4: (Left) the ratio of the charge weighted light quark singlets between the neutron and proton. (Right) the ratio of $x\gamma^{(inel)}$ between the neutron and proton, for comparison. At low x the behaviour of r_{F_2} dominates the behaviour of $x\gamma_{(n)}^{(inel)}$ as the continuum region is of greater importance.

Above input, $\gamma_{(n)}$ is approximated from the evolution of $\gamma_{(p)}$ in a manner analogous to that of the quarks as described in Section 7.2. Similarly, following the manner in which the photon contributions from inelastic and elastic components are made distinct, as described in Section 6.4, we distinguish between the flavour of quark whose splitting leads to the evolution of the photon. In particular, the majority of the contributions to γ during the evolution occur from splittings of the form $q \to q + \gamma$ or $\bar{q} \to \bar{q} + \gamma$.

One can label the contributions to γ from the originating quark or antiquark flavour to obtain γ_q, given by the following expression:

$$\gamma(x,\mu^2)_q = \int_{Q_0^2}^{\mu^2} \frac{\alpha(Q^2)}{2\pi} \frac{dQ^2}{Q^2} \int_x^1 \frac{dz}{z} \Big(P_{\gamma,q}(z) q^+(\frac{x}{z}, Q^2) \Big). \tag{7.21}$$

where the $+$ superscript once again denotes singlet type distributions of the form $q + \bar{q}$.

Assuming isospin symmetry, which as shown in the previous section holds to a

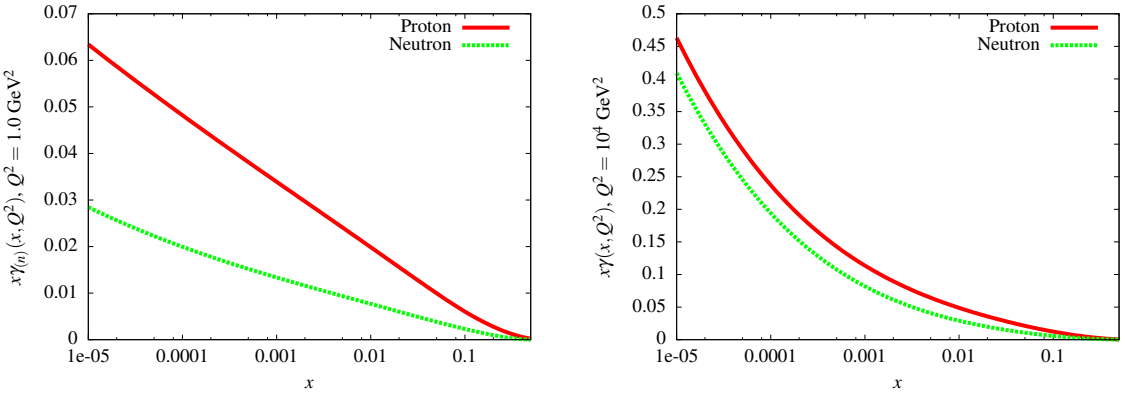

Figure 7.5: A comparison of the total Neutron and Photon PDFs at $Q = 1$ GeV (left) and $Q = 100$ GeV (right).

good approximation, one can make assumptions based on the predicted splittings in the neutron evolution to re-weight the contributions of each γ_q of the proton, based on the scheme laid out in Eq. (7.12) to obtain:

$$\gamma(x,Q^2)^{(inel)}_{(n)} = \frac{e_d^2}{e_u^2}\gamma_{u,(p)}(x,Q^2) + \frac{e_u^2}{e_d^2}\gamma_{d,(p)}(x,Q^2) + \gamma_{\{s,c,b,g\},(p)}(x,Q^2), \qquad (7.22)$$

where the final term accounts for all other flavours, whose contributions are assumed to be identical for the neutron and proton.

At the level of approximation adopted, the expression given above is expected to be accurate to $\mathcal{O}(\alpha)$, with errors of $\mathcal{O}(\alpha\alpha_S + \alpha^2)$. Anticipating results from the next section, it is seen that these higher orders induce changes in the resultant photon of $\sim 3\%$ at high x, while the uncertainties on the CLAS fit and the PDFs themselves each introduce $\sim 1\%$ uncertainty on the photon PDF at low and high x respectively. Therefore, one could conservatively estimate the uncertainty of the photon of the neutron PDF to be $\mathcal{O}(5\%)$ at high x and $\mathcal{O}(2-3\%)$ at low x where the PDF and higher order uncertainties dominate (where any considerations of the uncertainty due to the elastic distribution is neglected).

As seen in Fig. 7.5, although substantially smaller than that of the proton at the input scale, at the electroweak scale, $Q = 100^2$ GeV^2, the photon of the neutron is seen to be comparable in magnitude to that of the proton. This is anticipated

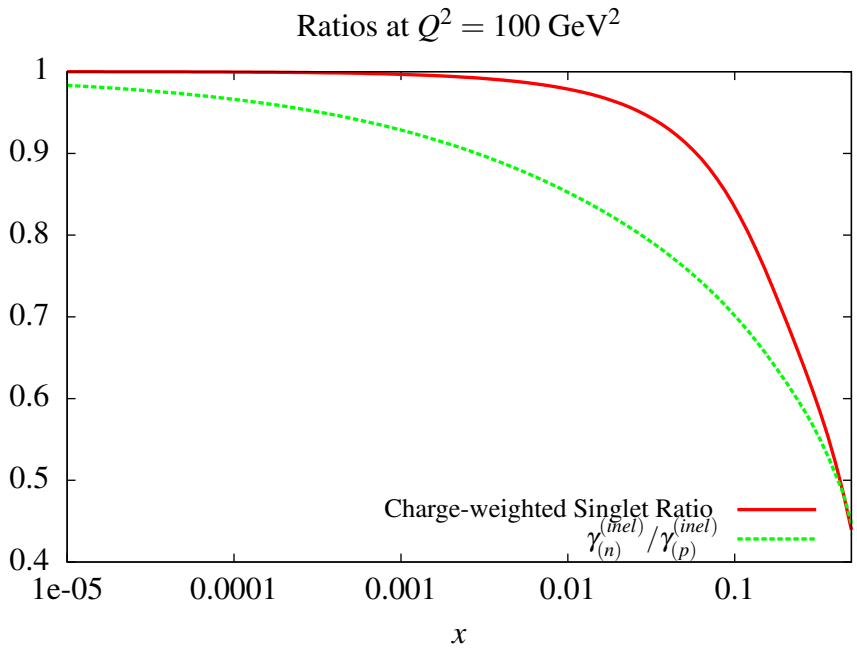

Figure 7.6: (Red, upper curve) The ratio of $\sum_i e_{q_i}^2(q_i + \bar{q}_i)$, that is the charge weighted sum of quark singlets, in the neutron to that of the proton. (Green, lower curve) The ratio of inelastic photon PDFs between the neutron and photon. At low x, these are both seen to tend towards unity as the flavour invariance of the sea (which obeys isospin symmetry maximally) dominates.

since the ratio of charges used to re-weight the proton contributions are $\mathcal{O}(1)$, and as $\gamma_{(p)}^{(el)}$ becomes less significant in the evolution, as seen in Fig. 6.5, the inelastic contribution dominates.

This is seen in Fig. 7.6, which is analogous to Fig. 7.4 at a higher scale, showing the ratio of the charged-weighted quark singlets (Σ_C) between the proton and neutron, and the ratio of $\gamma_{(n)}^{(inel)}/\gamma_{(p)}^{(inel)}(x,Q^2)$ at the same scale. As shown above for the input, the isospin invariance demonstrated at low x in the sea quarks means that the valence properties of the hadrons are less relevant at higher scales, leading to a neutron photon PDF comparable with that of the proton.

Chapter 8

Results

In this chapter a comparison of the photon outlined in this thesis with that of other contemporary sets is presented, as well as the effects that arise incorporating QED splitting kernels and the changes to the structure functions during the fit. We also show the effects of re-fitting to existing data with the modified evolution and the comparison of the photon at NLO and NNLO in QCD. We also investigate how the inclusion of QED affects the fit value of α_S when it is fit from data and discuss in detail the uncertainty on the photon PDF and its contributing sources.

8.1 Effects on the Partons due to QED Corrected DGLAP Evolution

Here we show the parton distributions that are produced as a result of the changes given in the preceding sections (primarly those related to the inclusion of QED effects in the DGLAP scale evolution of the partons). In doing so, we draw a comparison to the evolution of the partons without these effects, but re-emphasise that the basis of comparison is that described in Section 6.1, fit with additional data, rather than the publicly available MMHT2014 partons. Furthermore, we note that in the following discussion, the inclusion of QED splitting kernels is understood to include those at $\mathcal{O}(\alpha)$, $\mathcal{O}(\alpha\alpha_S)$ and $\mathcal{O}(\alpha^2)$, unless otherwise mentioned.

The effect of QED evolution on the quarks, prior to refitting, is relatively modest, as expected due to the $\mathcal{O}(\alpha/\alpha_S)$ relevance of the QED splitting kernels in comparison to those of QCD. On the left hand side of Fig. 8.1 we present the percentage

change in the u, d and s distributions, as well as the gluon, when QED kernels are included, against a default of pure QCD kernels at NNLO.

Although the change appears to become large at low x, this is in fact an artifact of the PDF parameterisation of the gluon, the expression for which is reproduced here for convenience:

$$xg(x,Q_0^2) = A_g(1-x)^{\eta_g}x^{\delta_g}\left(\sum_{i=1}^{2} a_{g,i}T_i^{Ch}(y(x))\right) + A_{g'}(1-x)^{\eta_{g'}}x^{\delta_{g'}}. \tag{8.1}$$

Recall that the η's, δ's, a_i's and A's (with one exception, discussed below) represent free parameters within the fit. Of note is the fact that two competing contributions to this expression dominate the form of the input distribution (and therefore subsequent effects in the evolution of the sea) at low x. The final term, $A_{g'}(1-x)^{\eta_{g'}}x^{\delta_{g'}}$, is provided to give the gluon greater flexibility in its parameterisation and as discussed briefly in Section 4.3, is generally seen to improve the fit quality.

As discussed in Section 4.3, there is a strong correlation between the parameter A_g of this term and the parameter $A_{g'}$ which also determines the magnitude of the low x gluon at input. In particular the former term, with $A_g > 0$, generally leads to an increase in the gluon at low x, while the latter term with $A_{g'} < 0$ is generally a negative contribution in this range. During a fit to data a delicate balance and cancellation between these effects is seen to provide the best fit quality.

However, unlike the other parameters in this expression, A_g is determined solely from the requirement of conservation of momentum, as described in Eq. (6.11). If all other parameter values are taken from a fit using purely QCD kernels (as described in Section 6.1), the extra momentum provided by $x\gamma(x,Q_0^2)$ at input is compensated for by a reduction of A_g, which diminishes the gluon contribution at low x. Such an effect disrupts the delicate cancellation between the terms described above.

This is seen to reduce the overall gluon momentum during the evolution, as well as that of the quark singlet distributions, since the latter at low x are primarily driven by splittings of the form $g \to q + \bar{q}$. Therefore, a reduction in g is expected

and observed to have a knock-on effect in the same region, as shown on the left hand side of Fig. 8.1.

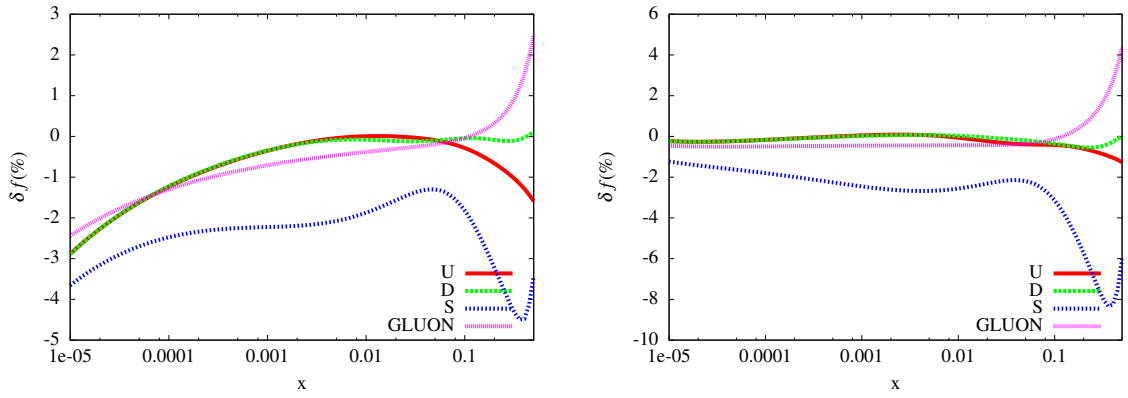

Figure 8.1: The percentage change in the u, d, s, g partons at $Q = 100$ GeV due to QED evolution with (right) and without (left) refitting to data.

In anticipation of Section 8.2, we note that the right hand plot of Fig. 8.1 shows the effects on the quarks after refitting, where it is seen that the exaggerated effects of the evolution at low x are compensated by the other parameters of the gluon, as discussed above.

However, the behaviour of the partons at high x, which shows a small reduction in the singlet distributions are interpreted as genuine effects pertaining to the inclusion of the QED contribution to P_{qq} outlined in Section 6.3. In particular, this reduction is primarily a natural consequence of the inclusion of P_{qq} in QED, which accounts for $q \to q + \gamma$ type processes in addition to the $q \to q + g$ previously included due to QCD. At high x, this has the effect of reducing the quark singlet momenta, with corresponding increases in $x\gamma(x, Q^2)$.

We also make note that although it is seen that the s distribution experiences a larger magnitude of change due to QED than that of the other partons, this effect is better understood as a consequence of the $s + \bar{s}$ distribution being most sensitive to the effects of refitting due to being less well constrained by the data, rather than having an enhanced sensitivity to the effects of QED. More generally, one can see that the singlet $(q + \bar{q})$ and gluon PDFs, upon refitting with the effects of QED, all lie within the uncertainty ranges established by a pure QCD fit. As seen in Figs.

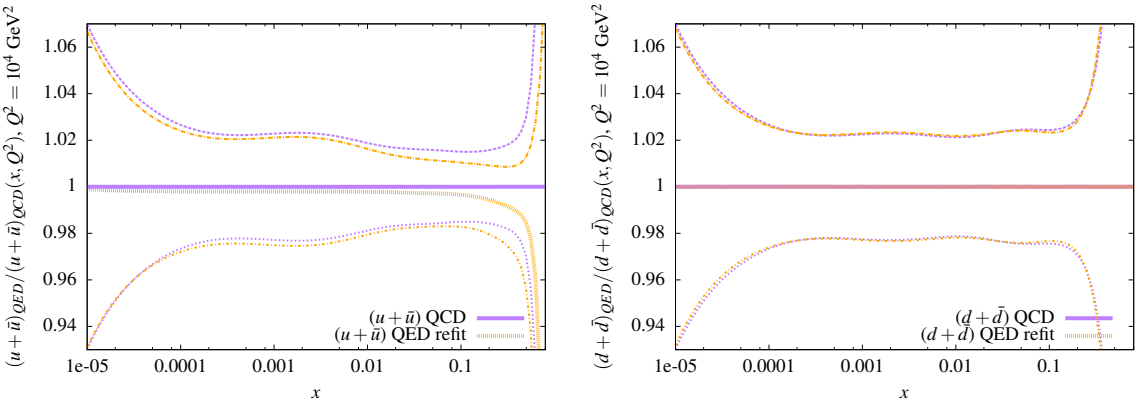

Figure 8.2: The ratio of the $(u+\bar{u})$, $(d+\bar{d})$ distributions (with uncertainties) fit with and without the effects of QED in the evolution (both at NNLO in QCD) at $Q = 100$ GeV.

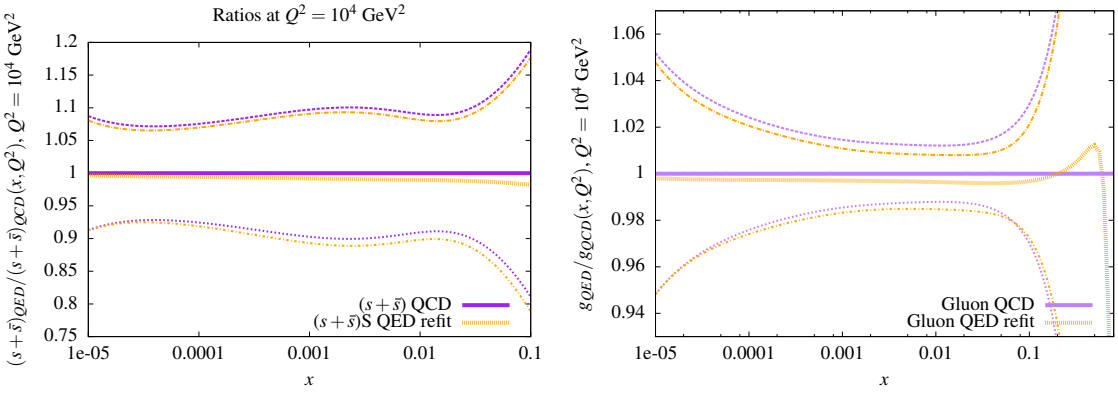

Figure 8.3: The ratio of the $(s+\bar{s})$, g distributions (with uncertainties) fit with and without the effects of QED in the evolution (both at NNLO in QCD) at $Q = 100$ GeV.

8.2 - 8.4, the central values and uncertainties remain only modestly affected, with $\mathcal{O}(2\%)$ reduction for the $s+\bar{s}$ distribution, (with a slight increase in the reduction at high x, due to the effect of QED splittings mentioned above).

Most sensitive to the effects of refitting are the up valence quarks, u_V, and to a lesser extent the down, d_V, which experience a greater magnitude of change at low x in their central values $\mathcal{O}(2-5\%)$. Once again it is noted that this effect is marginal given the large uncertainties ($\sim 20\%$) in the valence quark PDFs in this region.

In Fig. 8.5 the fractional momenta carried by the singlet distributions (separated by flavour), the gluon and photon is given as a function of Q^2, for both the

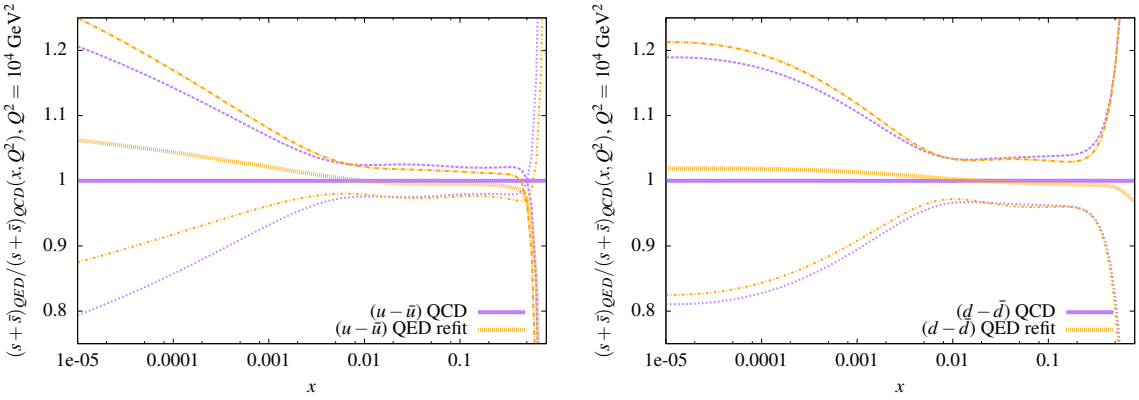

Figure 8.4: The ratio of the $(u-\bar{u})$, $(d-\bar{d})$ distributions (with uncertainties) fit with and without the effects of QED in the evolution (both at NNLO in QCD) at $Q = 100$ GeV.

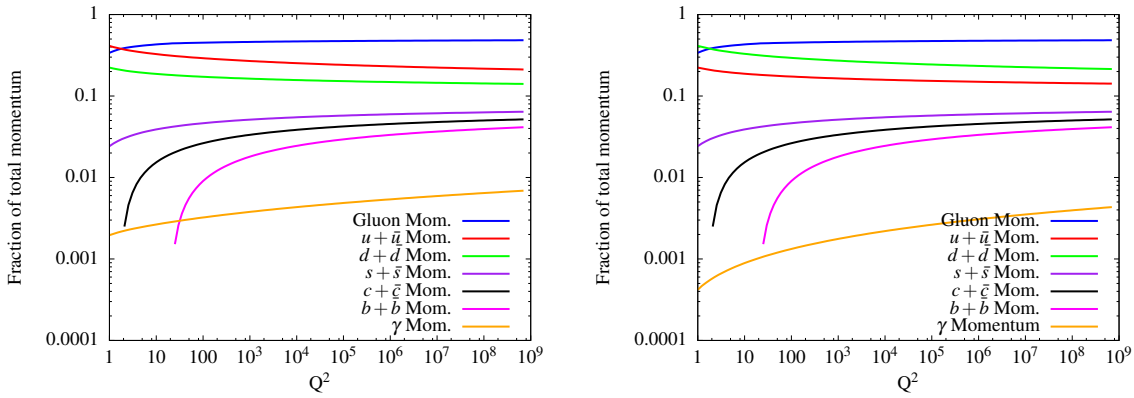

Figure 8.5: The fraction of total hadron momentum carried by the partons for the proton (left) and neutron (right) QED corrected PDF sets laid out in this thesis.

proton and neutron. At input, $\gamma_{(p)}$ is seen to carry 0.196% of the proton's total momentum and at very high scales it carries $\mathcal{O}(1\%)$ (0.7%) of the proton's whole. As anticipated from the previous chapter, the $\gamma_{(n)}$ is seen to carry substantially less, carrying 0.03%, with a somewhat lower rate of increase in the total momentum carried due to the relative charged parton differences between the hadrons during evolution, as described in the previous chapter.

Although the photon itself only appears in the evolution with the inclusion of splitting kernels at $\mathcal{O}(\alpha)$, one is able to investigate the effects of higher and mixed orders in QED calculations on $x\gamma(x,Q^2)$. In Fig. 8.6, we observe that the

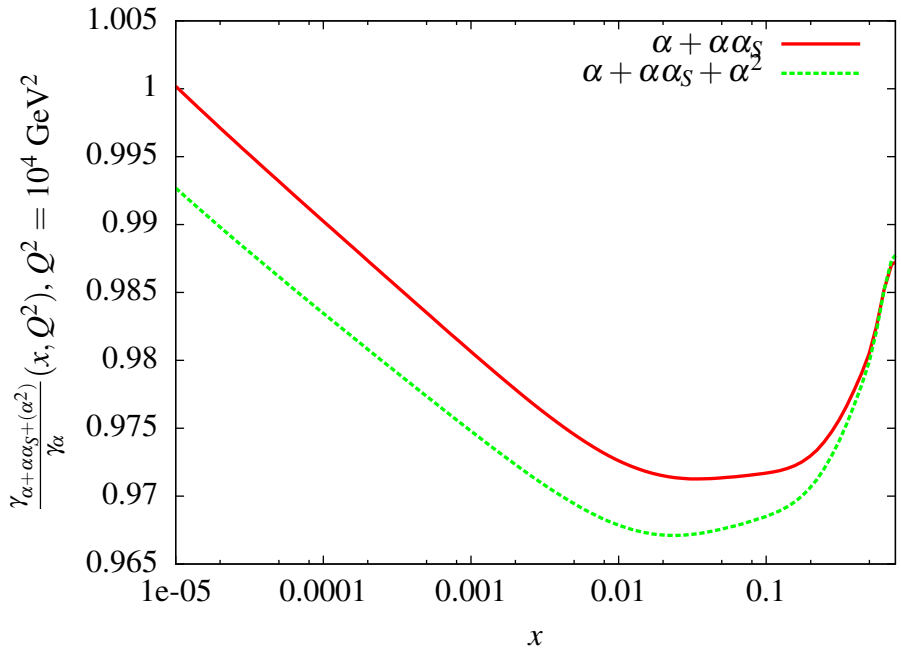

Figure 8.6: Ratio of the Photon PDF with and without $\mathscr{O}(\alpha\alpha_S)$,$\mathscr{O}(\alpha^2)$ corrections, at $Q^2 = 10^4$ GeV^2.

$\mathscr{O}(\alpha\alpha_S)$ and $\mathscr{O}(\alpha^2)$ kernels are seen to reduce the photon distribution during the evolution, by $\sim 1-3\%$, particularly at high x. We also note that the effect induced by the $\mathscr{O}(\alpha^2)$ kernels is of $\mathscr{O}(0.5-1\%)$ and that uncertainties associated with the exclusion of yet higher orders in perturbation theory are expected to be even smaller.

It is not thought that such scale uncertainties will be significant for the photon at the level of accuracy being discussed in this thesis, since it is smaller than other contributions to the uncertainty, discussed in Section 8.3, where a few large sources are seen to dominate the overall uncertainty on the photon distribution.

Similarly, the order in QCD at which the underlying evolution in DGLAP is performed is seen to have a modest effect on the resultant photon PDF produced at higher scales, as seen in Fig. 8.7. In this instance, the photon at NNLO experiences a slight reduction for intermediate values of x, $\mathscr{O}(1-2\%)$ with a slight increase at high and low x. This is largely due to differences in the underlying quark singlet, which as previously noted, have a strong role in influencing the form of $x\gamma(x,Q^2)$ at higher scales.

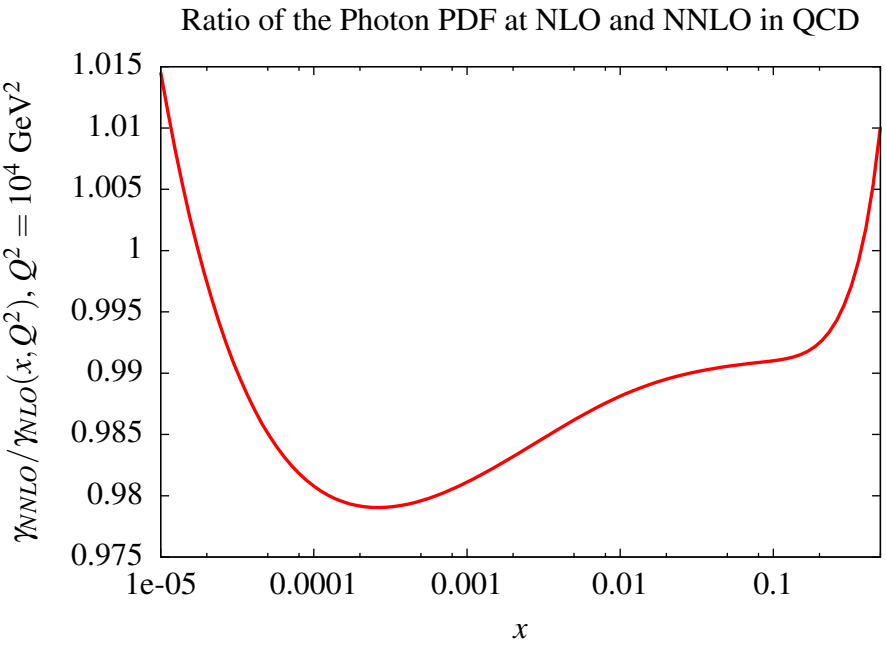

Figure 8.7: Ratio of the Photon PDF at NLO and NNLO in QCD during DGLAP evolution, at $Q^2 = 10^4$ GeV^2.

8.2 Results of a Global Fit with QED Corrections

The fitting procedure used in determining the new parton parameters is broadly similar to that of MMHT 2014, minimising the total χ^2 with respect to the available data (3276 data points), with the exception of changes to the structure function fits as detailed below, and the inclusion of new data sets, as described in Section 6.1. In Chapter 9 we detail the results of an alternative fit that also includes high mass Drell-Yan data, which is seen to have some sensitivity to the inclusion of QED effects.

8.2.1 Fit Quality

In Table 8.1, we provide the change in the total χ^2 in the fit to all data after the inclusion of all QED effects at NLO and NNLO, before and after refitting the partons. In the former case, the best fit values from a pure QCD fit are used for the input partons and fixed while the effects of the QED are applied solely to the evolution. A full breakdown of the χ^2 for each data set is given in Appendix A.

The change in fit quality due to both the changes in the evolution and $\mathcal{O}(\alpha)$

Change in χ^2 due to QED evolution compared to MMHT14+HERA I+II			
NLO before fit	NLO after fit	NNLO before fit	NNLO after fit
4180 (+41)	4151(+12)	3574 (+42)	3539 (+7)

Table 8.1: The total χ^2 for partons with the effects of QED, both prior to and after refitting the parton parameters, at NLO and NNLO. Before the fit, the parameters derived from the QCD fits described in Section 6.1 are used. The NLO fit contains 3609 data points, while the NNLO contains a total of 3276. The numbers in the parentheses indicate the magnitude of the change from the MMHT14+HERA set.

corrections to the structure functions detailed below are modest, as demonstrated in table. While the effects purely driven by the evolution naturally lead to an increase in χ^2 (where the pure QCD fit parameters are used), this is somewhat reduced after refitting the partons to data with the full QED effects included. However, some increase is still observed after refitting, found primarily to be due to tension with the BCDMS F_2 and ZEUS CC data, as given in Appendix A, where the former is responsible for a $\sim +6$ increase in the total χ^2 and the latter $\sim +2$. This is somewhat compensated for by a ~ -2 reduction from a slightly improved fit to F_2 and F_3 data from the NuTeV experiment, which see a mild improvement to the fit.

It should be noted that other changes such as the addition of new data and, to a much smaller degree, modifications such as the inclusion of the second term in Eq. (6.25) generate a set of distributions with a fit quality ($\chi^2_{QCD}/n_{data} = 3532/3276$) that differs from that of MMHT 2014 [78], even in the pure QCD case.

8.2.2 Comparison of $x\gamma(x,Q^2)$ Distributions

As seen in Fig. 8.8 the resulting photon PDF is seen to have relatively good agreement with those of LUXqed and NNPDF3.1luxQED, with agreement to within $\sim 2\%$ over a broad range of x, and more diverging predictions at high x where uncertainties are seen to be large and overlapping. In particular the photon developed in this work displays a very slight tendency to be somewhat larger in the intermediate range of x and predicts a somewhat smaller photon at lower x.

This is, to an extent, expected when one considers that during the evolution, the charge-weighted singlet ($\sum_i e_{q_i}^2(q+\bar{q})$) differs between MMHT and those of PDF4LHC15_nnlo_100 [71] (which are the underlying partons used for LUXqed

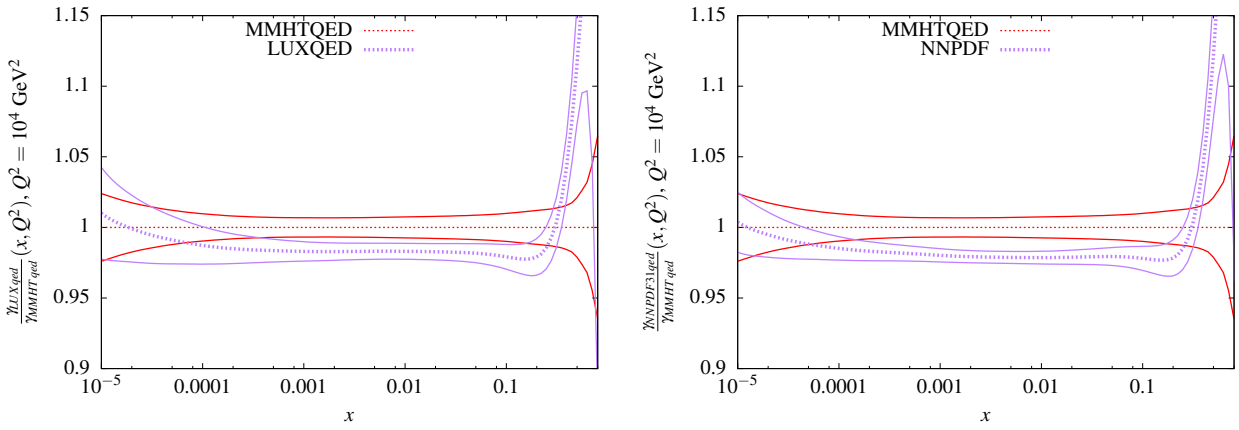

Figure 8.8: The ratio of Photon PDFs between the LUXqed and NNPDF3.1luxQED sets with that of MMHT, at $Q^2 = 10^4$ GeV^2.

in the higher Q^2 representation of $F_{2,L}$) and NNPDF3.1 [90] as seen in Fig. 8.9. Indeed, even in the absence of QED effects during the evolution, the baseline for the singlet distribution of quarks in MMHT was somewhat increased after fitting to the HERA I+II data when compared to that of MMHT2014. This $\sim 3-4\%$ reduction of the charge weighted singlet between the sets as compared with ours in the range $10^{-4} < x < 10^{-1}$ is naturally expected to manifest as a reduction in the relevant photon PDF ratios, since the evolution of $x\gamma(x,Q^2)$ is sensitive to this combination of partons, as discussed in Section 7.3. Indeed, a comparison of Figs. 8.8 and 8.9 indicates that the photon and the charged singlets for both the LUXqed and NNPDF sets appear to become greater than the equivalent distributions developed in this thesis at approximately the same value at high x, $x \simeq 0.5$.

Another reason why we anticipate that the $x\gamma(x,Q^2)$ as outlined in this work may be somewhat greater in value, in an intermediate range in x, compared to that of LUXqed is due to the exclusion of lepton splitting contributions in our DGLAP evolution, which are included in the evolution used to develop the LUXqed set. In Section 6.3 we explicitly neglected the sum over lepton charges in Eq. 6.22. In general, since $\gamma \to l\bar{l}$ splittings should reduce the photon distribution, one expects that excluding this term should lead to a somewhat increased photon. To estimate the effect of including this term, in Fig. 8.10 we draw a comparison to a $x\gamma(x,Q^2)$

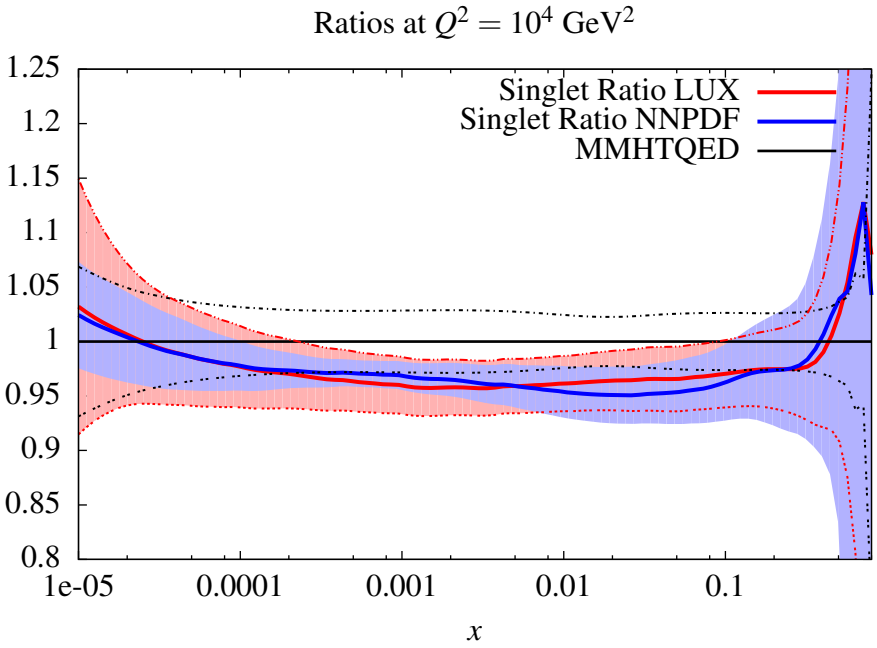

Figure 8.9: The ratios of the charged singlet, $\sum_i e_{q_i}^2 (q + \bar{q})$, between the LUXqed (which in turn adopts the quark and antiquark PDFs of PDF4LHC15) and NNPDF3.1LUXqed, against that of our set.

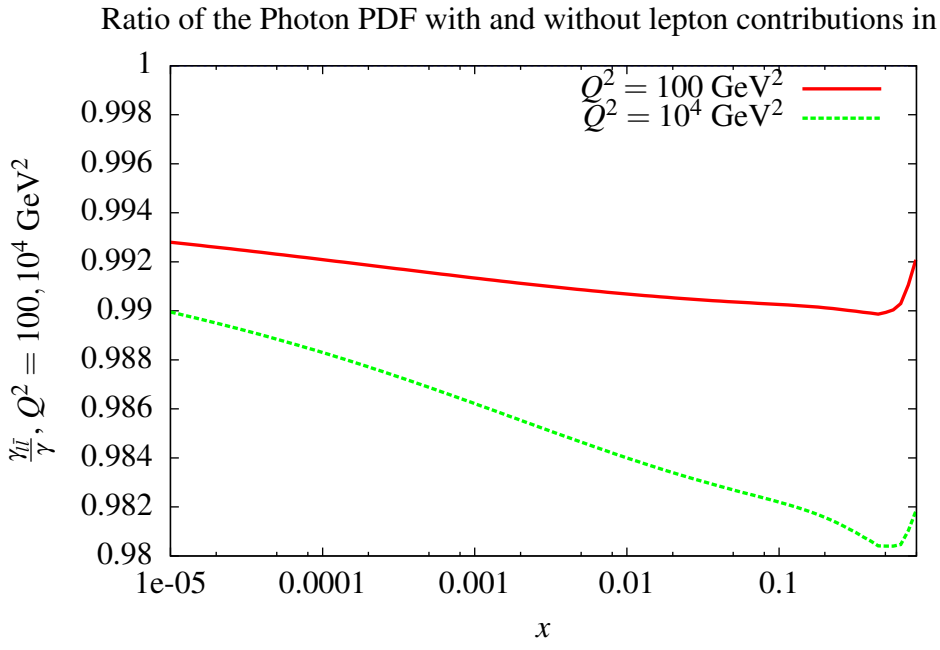

Figure 8.10: The ratios of photon with and without the sum over lepton charge, $\sum e_l^2$ contribution (the right hand side of Eq. 6.22) in the $\mathcal{O}(\alpha)$ contributions to $P_{\gamma\gamma}$.

evolved with $\mathcal{O}(\alpha)$ lepton splittings included in evolution and as anticipated find that this term does lead to a $\mathcal{O}(1-2\%)$ reduction, which becomes more pronounced at higher Q^2. Along with the ratio of the charged singlet used in the evolution, the neglecting of lepton splittings[1] leads to an independent source of enhancement for our $x\gamma(x,Q^2)$, further accounting for the difference seen in Fig. 8.8.

Finally, common to all the sets are errors of $\mathcal{O}(1\%)$, displaying the remarkable improvements in accuracy seen in photon PDFs developed on the strategy outlined in this thesis and that of [17] and [19], in comparison to that of older sets. A full breakdown of the contributing sources of error are explored in subsection 8.3.

8.2.3 QED Corrected Structure Functions

During the fit, in order to make a comparison of the PDFs to DIS data from scattering experiments, one requires a way of relating the partons to the measured structure functions $F_{2,3,L}$, for example:

$$F_2(x,Q^2) = x\sum_{q,\bar{q}} e_q^2 \int_x^1 \frac{dz}{z} q(z,Q^2)\Big\{\delta(1-\frac{x}{z}) + \frac{\alpha_S}{2\pi}C_q(\frac{x}{z}) + ...\Big\} + x\sum_{q,\bar{q}} e_q^2 \int_x^1 \frac{dz}{z} g(z,Q^2)\Big\{\frac{\alpha_S}{2\pi}C_g(\frac{x}{z}) + ...\Big\}. \tag{8.2}$$

Where $C_{q,g}$ are the coefficient functions which act, in essence, to renormalise the bare quark and gluon distributions and whose expressions may be found in [121]. Analogous to the splitting kernels of DGLAP P_{ij}, these coefficients are calculated at a given order in perturbation theory, for the relevant gauge theory (typically QCD). The introduction of the photon and of QED to the splitting kernels motivates the modification of this expression to include $\mathcal{O}(\alpha)$ corrections to the coefficients C_i, introducing terms of the form $C_\gamma^{(\alpha)} \otimes \gamma(z,Q^2)$ for $F_{2,3,L}$ in both Neutral Current (NC) and Charged Current (CC) processes.

In Fig. 8.11 we show the effect of these changes with and without refitting. Once again, the eccentricity introduced by the gluon parameterisation is seen to

[1] Note that excluding this term is still a reasonable approximation given that a fully consistent treatment with a coupled DGLAP evolution as performed in the remainder of this thesis would require the development of lepton PDF distributions which as discussed in [105] are found to have a negligible impact on the evolution of the PDFs on the whole.

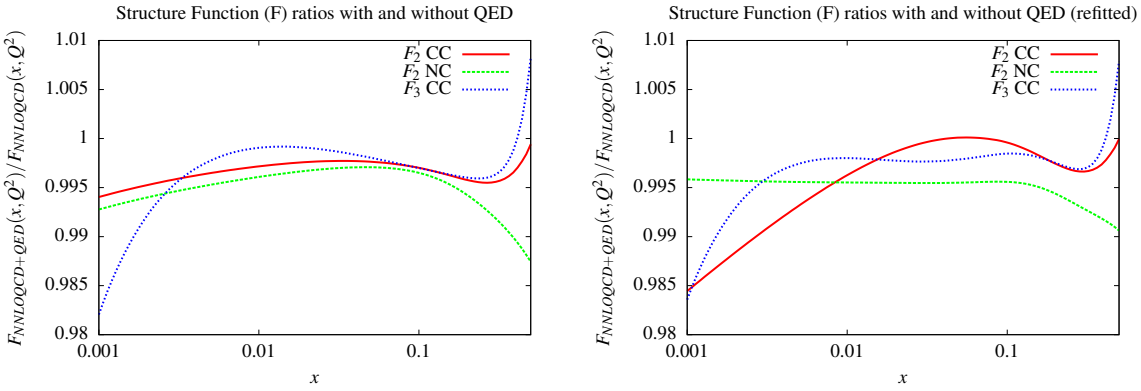

Figure 8.11: The ratio of the Charged and Neutral Current F_2 and Charged Current $xF3$ for the proton, with and without the effects of QED, both at $Q^2 = 10^4$ GeV^2. (Left) the effects of naïve inclusion of QED splitting kernels without the refitting of the partons (in which the artificial reduction in the low x gluon and hence the sea quarks has an enhanced effect, as discussed in the text). (Right) The ratio of Structure Functions after refitting the partons, with modest effects observed in F_2 CC and NC.

have an effect at low x, reducing F_2 and F_3 somewhat, while after fitting, the CC F_2 and F_3 are moderately decreased at low x. For the NC however, F_2 is generally reduced by $\mathcal{O}(0.5\%)$, which is anticipated by the fact that the introduction of QED in the evolution is seen in general to diminish the quark singlet content (as seen in Fig. 8.1 in the previous section).

8.2.4 Effects of QED on α_S Determination in Global PDF Fits

As well as the fit described above, we have also performed a global fit to data with the usual parton parameters left free while simultaneously fitting to a value for the strong coupling constant at the Z mass scale, $\alpha_S(M_Z)$, which fixes the scale for the running of $\alpha_S(Q^2)$ during the evolution. The value typically used during the evolution and the comparison to data is taken as a fixed value $\alpha_S(M_Z) = 0.118$, which reflects a combination of both the best fit value exclusively from our fit to data (which is sensitive to the PDFs), and the independent inclusion of the world average of $\alpha_S(M_Z) = 0.1181 \pm 0.0011$ [38], as discussed in subsection 5.1 of [78].

In principle, one expects that the value of $\alpha_S(M_Z)$ found after refitting with the effects of QED included in the fit will be somewhat less than that found in a pure

QCD fit. This is because at leading order, the effect on the $q+\bar{q}$ distributions during the evolution, particularly at high x, is due to gluon emission, $q \to qg$, which leads to a slight reduction of the singlet. In a pure QCD fit, the parameters that provide the best fit are a combination of both the input distribution and a value of $\alpha_S(M_Z)$ which drives gluon emission at a rate (determined by $P_{qq}^{(QCD)}$) in the evolution such that the PDFs at higher scales are best fit to the data.

In leading order in QED however, the electromagnetic coupling α plays virtually the same role in the evolution of the singlet distributions, diminishing the high x content due to photon emissions $q \to q\gamma$. Therefore at LO, one can consider the inclusion of QED as an enhancement to P_{qq} with an increased effecting coupling:

$$\alpha_S \to \alpha' = \left(\alpha_S + \frac{e_q^2 \alpha}{C_F}\right), \tag{8.3}$$

which may be readily seen from an inspection of Eq. (6.21). In a fit that includes the coupling constants as free parameters, one expects that α', rather than α_S would tend towards a value that best models the loss of the singlet during evolution to emission (whether to a photon or gluon). Since α_S is the only free parameter in the fit (where we adopt the world best measurement value for α [38]), one naturally expects the best fit value for α_S to be reduced to accommodate the modification in Eq. (8.3). Naïvely, one may expect the magnitude of this reduction to compensate for the magnitude of the modification term $e_q^2\alpha/C_F \sim 10^{-3}$. Though small, this is similar to the global fit uncertainty on α_S, and the effects of QED may therefore be significant in its determination.

This was also investigated in the development of the original MRST QED [12], where it was found that despite the considerations mentioned above, between the pure QCD and QCD+QED fit, $\alpha_S(M_Z)$ remained essentially unchanged. The reason found for this perceived lack of change in $\alpha_S(M_Z)$ after refitting is that as well as the propensity for the value to be reduced to the effects mentioned about, is that the fit, (especially the NMC and HERA data) prefers a larger value for the gluon at low x, which is sensitive to $\alpha_S(M_Z)$. This is because the QCD scaling of F_2 goes as $dF_2/d\ln Q^2 \propto \alpha_S P_{qg} \otimes g(x,Q^2)$. In short, the fit to the gluon at low x has

a tendency to fit for a larger value of $\alpha_S(M_Z)$ than would otherwise be obtained. Since, as mentioned above, the inclusion of the photon in the evolution is seen to reduce $g(x,Q^2)$ at low x due to the conservation of momentum constraint applied at input, in order to fit to the correct scaling behaviour for F_2, the tendency is for the fit to require a larger value for $\alpha_S(M_Z)$ to compensate. This pulls in a direction opposite to the reduction of $\alpha_S(M_Z)$ as described above, and reduces the magnitude by which one might anticipate a change after refitting with the effects of QED.

With the updated QED parton framework, we find that $\alpha_S(M_Z)$ experiences a reduction from 0.11808 in the pure NNLO QCD case to 0.11796 in the fit with QED (with a reduction from 0.11991 to 0.11989 ($\Delta\alpha_S(M_Z) = -0.00002$) at NLO in QCD). Although this does represent a small, expected reduction, the difference, $\Delta\alpha_S(M_Z) = -0.00012$, is considered small, and in neither case is seen to improve the total fits by any significant degree ($\Delta\chi^2 < 1$). However, in future global fits, the inclusion of QED effects in the partons may come to be significant as the accuracy of such measurements are improved.

8.2.5 Photon-Photon Luminosity

A sense of the photon PDF's relevance to particle production at colliders such as the LHC may be determined from an inspection of the $\gamma\gamma$ luminosity expected at these energies (14 TeV), shown in Fig. 8.12. This is determined from the equation:

$$\frac{dL_{\gamma\gamma}}{d\ln m^2} = \frac{m^2}{s}\int_{\frac{m^2}{s}}^{1}\frac{dz}{z}\gamma(z,m^2)\gamma\left(\frac{m^2}{zs},m^2\right), \tag{8.4}$$

where m is the total invariant mass of the incoming partons (and subsequent product).

As seen in Fig. 8.8, the correspond toence between our photon and that of other sets based on the LUXqed formulation show good agreement, and therefore our predicted $\gamma\gamma$ luminosity, $dL_{\gamma\gamma}/d\ln m^2$, bears a strong resemblance to others in the literature (e.g. Fig. 19 in [99]). Also shown in Fig. 8.13 is the expected luminosity for a High-Energy LHC proposal with (CoM) energy $\sqrt{s}$ =27 TeV, and a Future Circular Collider with a $\sqrt{s}$ =100 TeV, where the total $\gamma\gamma$ luminosity is

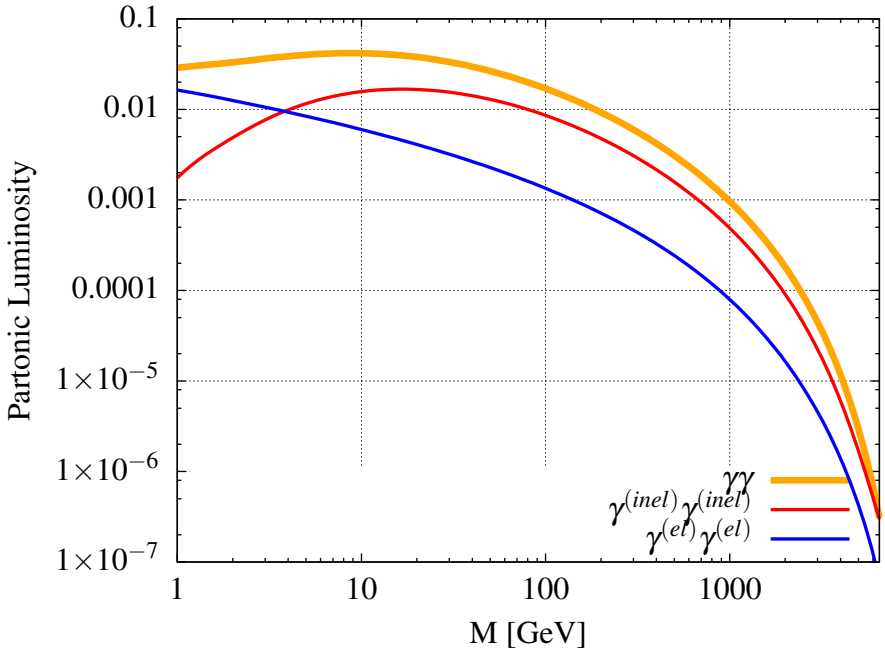

Figure 8.12: $\gamma\gamma$ partonic luminosities as a function of invariant mass at Centre-of-Mass energies of 14 TeV. Note that for the elastic $\gamma^{(el)}\gamma^{(el)}$, the multiparticle interaction (MPI) effects are not included, and their inclusion would reduce (lower) the blue curve to some degree (discussed in text).

comparable to that of $\Sigma_i(q_i\bar{q}_i + \bar{q}_i q_i)$ at present LHC CoM energies (14 TeV).

Furthermore, since our Photon PDF is separable by its elastic and inelastic components, we are able to distinguish between $\gamma^{(inel)}\gamma^{(inel)}$ and $\gamma^{(el)}\gamma^{(el)}$ contributions to the overall luminosity. The latter is of particular interest in the context of exclusive production of particles in coherent photon-photon scattering (as discussed in the latter half of [122]). In these events the protons collide peripherally, exchanging only photons while remaining intact, such that they can be detected and their kinematic properties reconstructed at the end caps of the ATLAS (AFP) [123] and CMS (CT-PPS) [124] detectors. In particular, as discussed in [123] and [124], one can obtain information about the three-momentum parallel to the beam direction, $\mathbf{p}_{\|}$, which allows one to reconstruct the mass of invisible final states.

Previous theoretical work on Central Exclusive Processes (CEP) has often performed calculations with the use of the Equivalent Photon Approximation [94][95], in which the photon flux associated with the colliding beam of charged particles may be expressed in terms of the elastic structure functions $F_{2,L}^{(el)}$, in a manner sim-

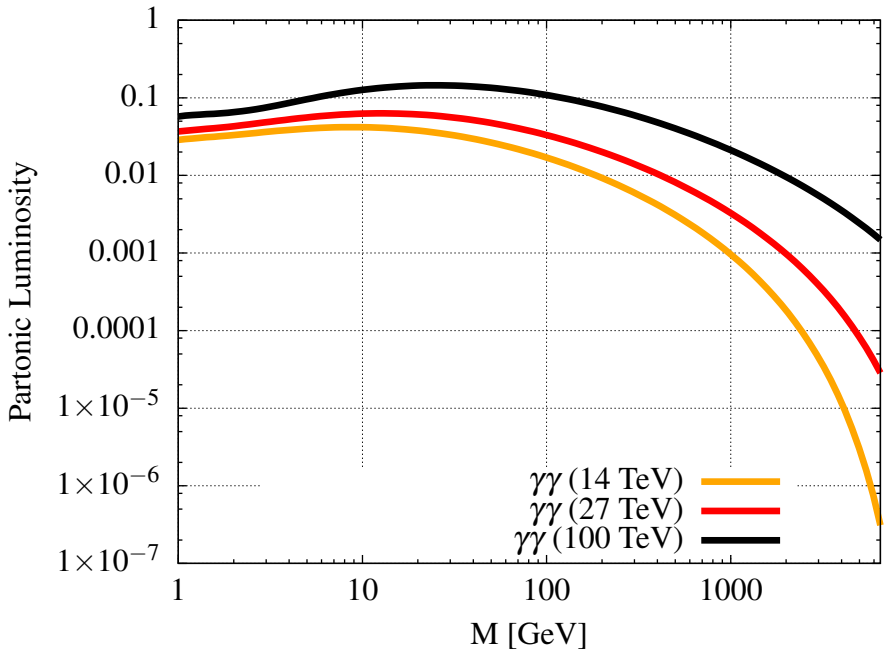

Figure 8.13: $\gamma\gamma$ partonic luminosities as a function of invariant mass at Centre-of-Mass energies of 14, 27 and 100 TeV.

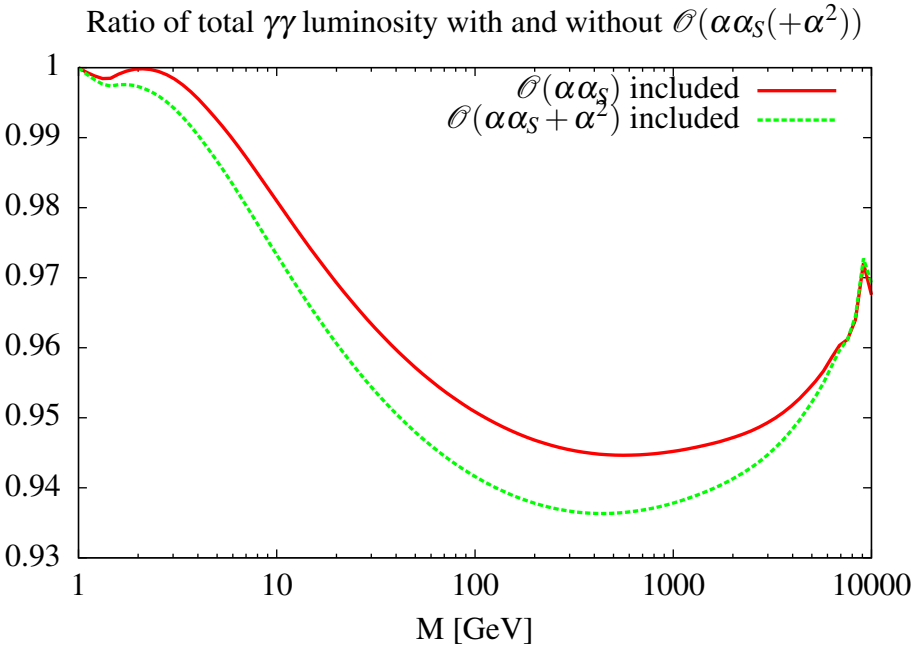

Figure 8.14: Ratio of $\gamma\gamma$ partonic luminosity as calculated from $x\gamma(x,Q^2)$ with and without $\mathcal{O}(\alpha\alpha_S)$ and $\mathcal{O}(\alpha^2)$ DGLAP splitting kernels during evolution as a function of invariant mass, at a proton-proton Centre-of-Mass energy of 13 TeV.

ilar to that considered in this paper. The $\gamma^{(el)}\gamma^{(el)}$ luminosity, represented in Fig. 8.12, corresponds to the luminosity that could be delivered in this approach.

However, this interpretation is qualified with an important caveat, which is that for an exclusive production process, with both protons seen to remain in tact after scattering, one needs to multiply the final result obtained from the naïve use of $\gamma^{(el)}$ as an incoming parton by a "soft survival" factor, that subtracts any contributions from multiparticle interactions (MPI) [125], in order to fully exclude the influence of other effects. Furthermore, the luminosities shown in Fig. 8.12 could not directly be applied to the calculation of cross sections for more exclusive final states, such as when explicit cuts are placed on the presence of additional tracks within the central portion of the detector [9].

We conclude this section with a discussion of the effect of higher and mixed orders of QED, $\mathcal{O}(\alpha\alpha_S)$ and $\mathcal{O}(\alpha^2)$ during the evolution and the significance of their impact on the total luminosity at present CoM energies at the LHC. As previously observed in Fig. 8.6, the inclusion of these higher order splitting functions in the evolution of $x\gamma(x,Q^2)$ have a tendency to reduce its magnitude, particularly at the higher range in x. In Fig. 8.14, the proportional effects of such changes in $dL_{\gamma\gamma}/d\ln m^2$ are seen as a function of the invariant mass of the final state product. In fact, above the electroweak and near TeV scales, the importance of these higher orders become significant, inducing a $\mathcal{O}(5\%)$ reduction in the total $\gamma\gamma$ luminosity.

8.3 Uncertainties on the Photon PDF

Due to the nature of our input distribution, much of the uncertainty contributions to our photon PDF bear strong resemblance to that of LUXqed and in some cases, our treatment of the uncertainty contributions are identical. However, as mentioned in Section 6.3, due to the lower starting scale adopted in our evolution procedure, we also include higher twist corrections in the form of a renormalon model, for which the undetermined coefficient A_2' in Eq. (6.27) is fit to the data, introducing an independent source of uncertainty.

For completeness, a full description of the uncertainty contributions is given

below, where we also direct the reader to Figs. 8.15-8.17 for reference, where one can also observe how the change in scale affects the form of the uncertainty.

- **Elastic:** The uncertainty contributions from the A1 fit for $F_2^{(el)}$ are twofold. In particular, the fits provided by A1 are given in the unpolarised and polarised forms, where the latter accounts for potential two photon exchange (TPE) processes between the lepton probe and the proton in DIS experiments. Following the approach of LUXqed, we use the latter for our estimate precisely because it provides constraints on TPE. As well as the intrinsic uncertainty provided by the A1 collaboration for this fit $\delta(F_2^{(el)})_a$, similarly to LUX, we adopt the symmetrised difference the polarised and unpolarised fit as an independent source of error, $\delta(F_2^{(el)})_b$. The total uncertainty on $F_2^{(el)}$ is then simply the sum of these two contributions in quadrature.

- **R:** The contributions from F_L are modelled in precisely the same manner as that of LUX, using the parameterisation of the form:

$$F_L(x,Q^2) = F_2(x,Q^2)\Big(1+\frac{4m_p^2x^2}{Q^2}\Big)\frac{R_{L/T}(x,Q^2)}{1+R_{L/T}(x,Q^2)}, \tag{8.5}$$

  where $R_{L/T} = \sigma_L(x,Q^2)/\sigma_T(x,Q^2)$ represents the ratio between the absorption cross sections for longitudinal and transversely polarised photons. Our expression for this ratio is provided by the LUX group, who, following the procedure used by the HERMES collaboration [102], in term adapt the expression from the R_{1998} fit [103] provided by the E143 Collaboration to use in low Q^2 regions and assign it a conservative $\pm 50\%$ uncertainty, which we also adopt.

- **W^2:** As mentioned in Section 6.2, since $F_2^{(inel)}$ is not universally well modelled by any given fit in both the "resonant" (where $F_2^{(inel)}$ displays Breit-Wigner type peaks due to hadronic excitations) and "continuum" (where $F_2^{(inel)}$ is seen to be smooth as a function of W^2) regions in phase space, and two distinct fits for $F_2^{(inel)}$ are used above (HERMES [102]) and below

(CLAS[101] and Cristy-Bosted[104]) a threshold of $W^2_{cut} = 3.5$ GeV^2. Since W^2_{cut} is defined somewhat arbitrarily and theoretically induces some small amount of discontinuity in the contributions to $\gamma^{(inel)}$, we treat the cut value as an independent source of uncertainty, varying it the region $3 < W^2_{cut} < 4$ GeV^2. Even with a relatively conservative approach, the uncertainty on W^2_{cut} is seen to be vastly dominated by other sources.

- **Resonance:** The uncertainty of $F_2^{(inel)}$ in the resonance region described above is taken as the symmetrised difference between the CLAS fit, which is used as the standard for our input, and that of the Cristy-Bosted, similar to the procedure used by LUXqed.

- **Continuum:** The uncertainty of $F_2^{(inel)}$ in the continuum region is adapted directly from the uncertainty bands of the GDP-11 fit provided by the HERMES collaboration. Note that this differs from the treatment in LUXqed, where the uncertainty estimate is produced by varying the scale from which the description of F_2 is produced from the GDP-11 fit or the quarks in the evolution. In practice, for both sets, this contribution is only a small contribution to the overall uncertainty.

- **Renormalon:** For the fitting and uncertainty of the coefficient A'_2 in Eq. (6.27), we implemented the original renormalon model of [110] into the calculation of the structure functions themselves, F_2 and F_3, as used in the fit. A'_2 was then varied to induce a $\Delta\chi^2 = \pm 10$ change in the overall fit quality of the partons (as seen in Fig. 6.3 in Section 6.3), creating a generous uncertainty band of $-0.4 < A'_2 < -0.2$, with a best fit value of -0.3. We note that our global fit to the data favours a renormalon contribution $\sim 50\%$ greater than the value used in the original model by Dasgupta and Weber [110]. At high x, this is seen to be a comparable source of uncertainty with that of $\delta(F_2^{(el)})$. Unlike all other terms discussed so far, the uncertainty in A'_2 enters during the evolution, rather than at input.

- **PDFs:** Similarly, since above the input scale $Q^2_0 = 1$ GeV^2, the $\gamma^{(inel)}$ contri-

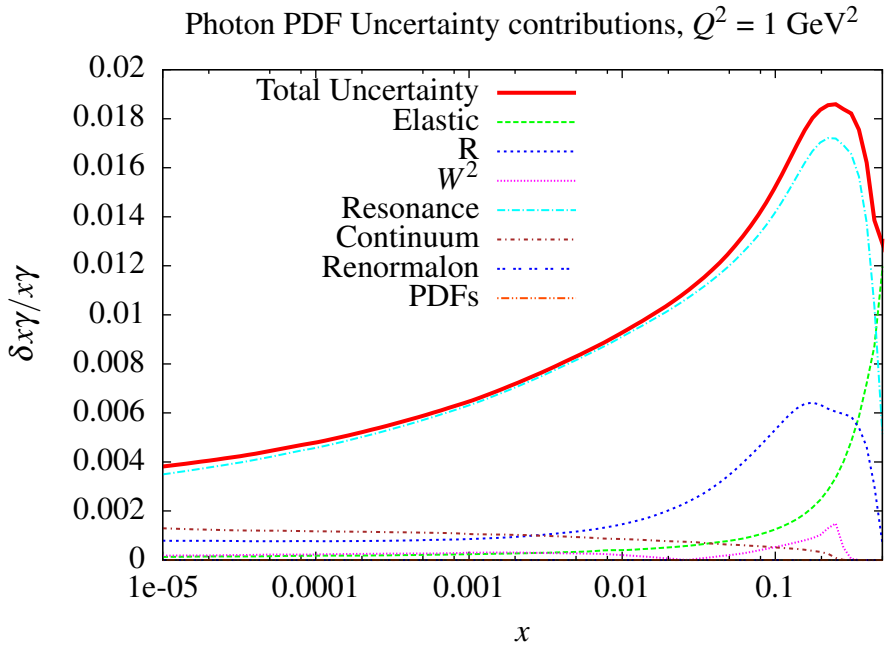

Figure 8.15: Photon PDF Uncertainty contributions (added in quadrature to give the total uncertainty), $Q_0^2 = 1$ GeV^2. Note that the upper x range has been restricted in this plot due to the effect of the kinematic cut given in Eq. (6.10) Section 6.2.

butions are modelled solely from the splittings of other partons during the DGLAP evolution, the intrinsic uncertainty on the other PDFs propagate into the form of the photon PDF as it evolves. This reflects the standard 50 eigenvector uncertainties associated with the fit of the free parameters in the MMHT parameterisation (see Eqs. (4.6) and (4.8)), which generate the uncertainty bands for all flavours of parton $(q, \bar{q}, g)$ and in turn generate uncertainties in the photon during splittings of the form $q \to q\gamma$ and $g \to q\bar{q}\gamma$. At low x, as is the case of LUXqed, this dominates as the primary source of uncertainty.

Since our $\gamma^{(inel)}$ is evolved from a common starting scale and fit consistently alongside the other partons of our set, we are alleviated of the consideration of matching scales between the photon and other partons (though seen to be negligible even when necessary, as shown for (M) in Fig. 15 of [99]). Furthermore, in comparison to that of LUXqed, our set neglects certain contributions to the photon uncertainty. In particular, rather than the Twist-4 uncertainties considered by

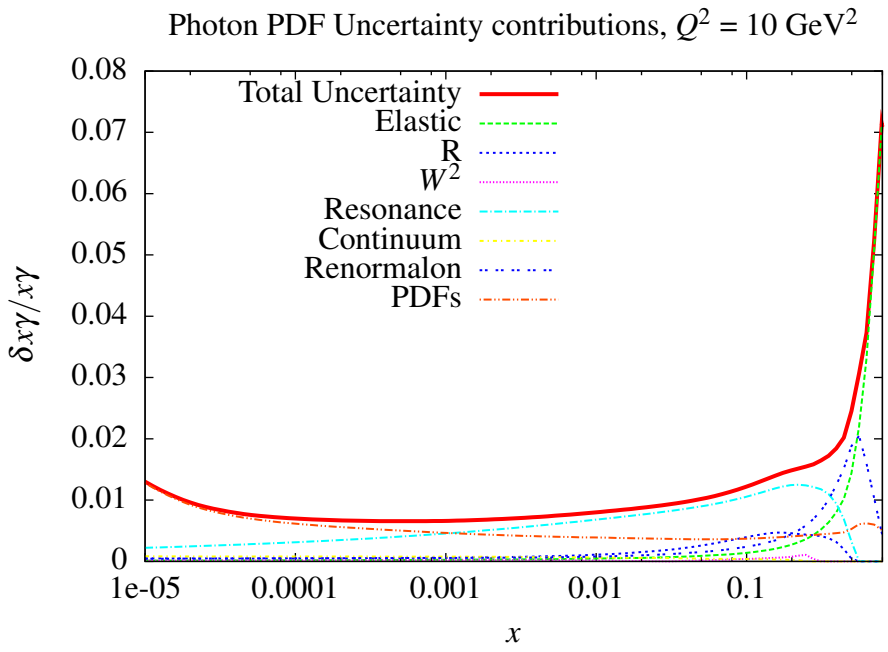

Figure 8.16: Photon PDF Uncertainty contributions (added in quadrature to give the total uncertainty), $Q^2 = 10$ GeV^2.

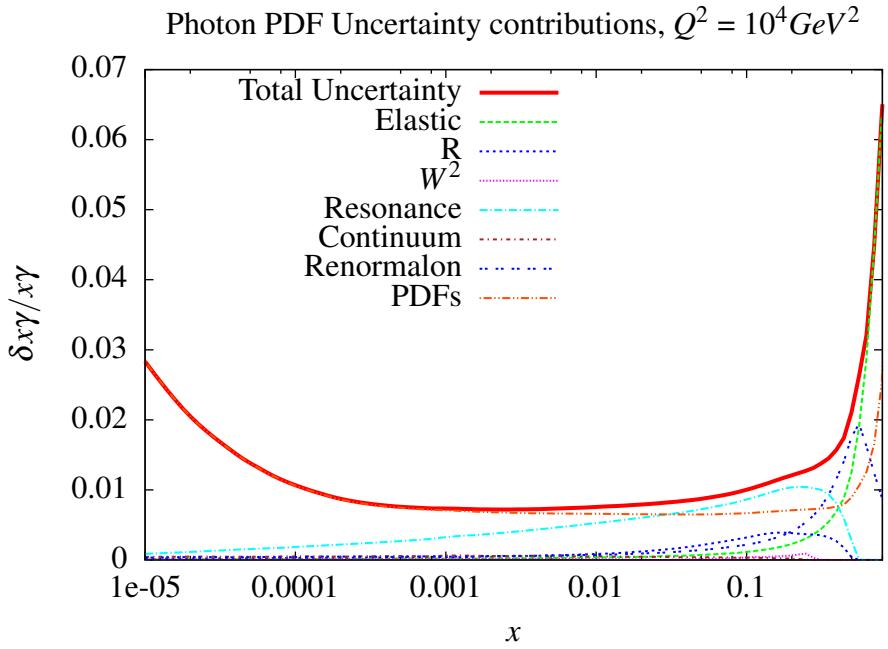

Figure 8.17: Photon PDF Uncertainty contributions (added in quadrature to give the total uncertainty), $Q^2 = 10^4$ GeV^2.

LUXqed for F_L (which an inspection of (T) in Fig. 15 of [99] reveals to be overwhelmingly dominated by other sources), our treatment of the Higher-Twist (HT) corrections to the structure function in the form of the renormalon lead to a more significant uncertainty at high x, consistent with our choice of a lower starting scale for the evolution.

Indeed, since our starting scale is at $Q_0^2 = 1$ GeV, as shown in Fig. 8.15, the uncertainties at input have a markedly different form to the kind that arises during the evolution. Naturally, effects that pertain to the evolution, (the PDF eigenvector uncertainties and the renormalon) are absent at this scale, and the dominating effects are seen to be the uncertainty on the resonance contribution to $F_2^{(inel)}$, the uncertainties on the Sachs form factors provided by the GD-11 fit ($\delta F_2^{(el)}$) and the uncertainty on $R_{L/T}$.

As the evolution occurs however, the PDFs overwhelmingly dominate as the source of uncertainty at low x, and in conjunction with the uncertainty on the renormalon parameter A_2', become significant contributions along with those of the Sachs form factors at higher x.

It is noted that we do not account for the uncertainty that arises from the Higher Order (HO) terms missing from the QCD components of the evolution, as estimated in LUXqed. Although we have given an indication of the magnitude of the change in order from QCD (from NLO to NNLO) in the evolution in Fig. 8.7 of the previous section (which broadly corresponds to the (HO) band in Fig. 15 of [99]), we do not treat this difference as an independent source of uncertainty, since PDFs have typically been provided at both NLO and NNLO in QCD, each with independently derived uncertainty bands. One could therefore symmetrise the difference between the photon PDFs provided at these orders (Fig. 8.7) to estimate the uncertainty of this effect. Despite not being included as a default, recent work [126] has begun to explore the possibility of incorporating such uncertainties into the PDF fitting framework of MMHT in a standard manner.

Overall, we note the similarity between the form of our uncertainty with others, being less than 2% for $10^{-5} < x < 0.5$, demonstrating a drastic improvement with

early photon PDF sets such as MRST2004QED [12] and NNPDF2.3 [14].

As stated at the end of Chapter 4, PDF sets are typically provided as grids in the LHAPDF6 format, with each grid representing either the central value of the PDFs, or the PDFs at a given $\pm$ eigenvector direction in the independent parameter space PDFs. As noted above, as well as the uncertainties that are routinely given in such sets associated with the non-photon PDF parameters, the set that is produced as a result of the work described in this thesis now contains uncertainties associated with the photon parameters at input and the A_2' parameter for the renormalon in the evolution. Details of these grids are provided in Appendix B.

Chapter 9

High Mass Drell-Yan

In order to explore the phenomenological implications of the PDF set outlined in this thesis, we calculate the effects on the double differential cross section for lepton pair (Drell-Yan) production in a hadron-hadron collider. This process is of particular interest, since the effects of QED, especially in the partons, is expected to be of non-negigible significance, particularly due the inclusion of $x\gamma(x, Q^2)$ as a contribution to the cross section.

In particular, we draw a comparison when including the effects of QED for the evolution of the PDFs, as well as the effect of additions to the cross section from photon-initiated (PI) contributions, as shown in Fig. 9.1, where the photon PDF enters as a direct input for the colliding partons.

9.1 QED and Photon Sensitivity in High Mass Drell-Yan

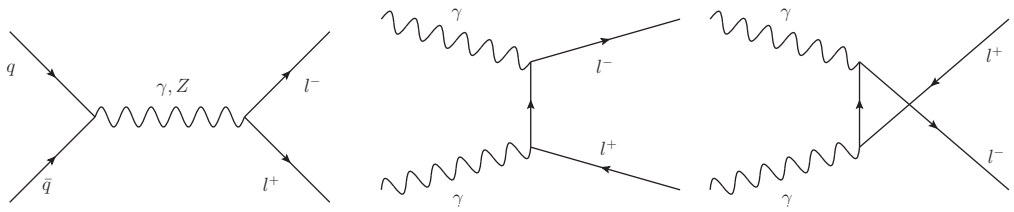

Figure 9.1: Leading order Drell-Yan production (left), with diagrams (centre, right) indicating $\mathcal{O}(\alpha)$ photon-initiated (PI) matrix element contributions to the total cross section.

In order to gauge the magnitude (and phenomenological significance) of these

effects we compare to data provided by the ATLAS collaboration [23] for high mass (116 GeV $< m_{ll} <$ 1500 GeV) Drell-Yan lepton pair production. The focus on production at high mass is chosen in order to reduce the effects of the Z production peak, $Q \sim M_Z = 91$ GeV, since the relative contribution of the PI processes are greater in the regions dominated by the γ channel. Therefore, the effects of PI contributions are anticipated to be more readily observable at low[1], $m_{ll}^2 \ll M_Z^2$, or high, $m_{ll}^2 \gg M_Z^2$, lepton pair invariant masses.

ATLAS provides double differential cross section measurements in 5 bins of lepton pair invariant mass, m_{ll}, and 12 (or 6) pseudo-rapidity bins in η. Figs. 9.2 to 9.6 show a comparison of the predictions using MMHT partons to produce the cross sections for comparison: (a) in the case of the standard QCD fit partons at NNLO as outlined in Section 6.1, (b) with QED modified partons to provide cross section calculations at NNLO in QCD and (c) with QED modified partons and additional contributions to the cross section from $\mathcal{O}(\alpha)$ photon initiated processes as shown in Fig. 9.1.

To calculate cross sections, we use grids provided by the xFitter collaboration [15] at NLO in QCD (generated with MadGraph5_aMC@NLO [128], aMCfast [129] and FEWZ [130]), with NNLO K-factors as well as LO QED corrections (for the inclusion of PI processes). Such grids were developed and used in [15] with the aim of creating a determination of $x\gamma(x,Q^2)$ from the same ATLAS data we aim to draw a comparison with, making them well suited to our purposes. These are then interfaced with a modified version of APPLgrid that has been adapted for the purposes of this work to include $\gamma\gamma$ processes for the final calculation.

In the following analysis it is emphasised that the contributions of PI processes implemented in the comparison to data will be most sensitive to $x\gamma^{(inel)}(x,Q^2)$, due to the prevalence of this contribution at $x\gamma^{(el)}(x,Q^2)$ at higher scales (as was seen in

[1] In fact, such data for low mass Drell-Yan is also available from the ATLAS experiment [127]. However, in releasing the data, they purposefully estimate and remove the expected photon-initiated component of the contributions to the cross section, using estimates produced from the MRST04QED set. Though this removal is likely to be less accurate than could be achieved using a modern $x\gamma(x,Q^2)$ such as the one produced in this thesis which supersedes the MRST set, the corrections are likely to be smaller than the magnitude of the photon-initiated component of the cross section.

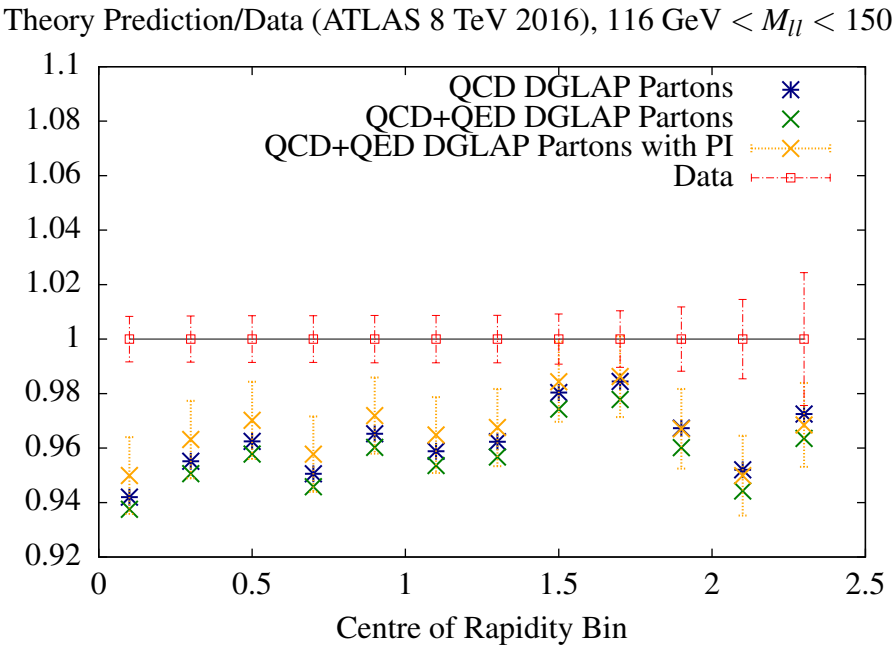

Figure 9.2: The ratio of theory to data of the cross section for Drell-Yan production in the mass bin 116 GeV $< M_{ll} <$ 150 GeV, differential in rapidity, as provided by the ATLAS experiment [23]. The ratios are provided for cross section calculations performed from pure QCD PDFs, QCD PDFs with QED corrections and for the latter including photon-initiated contributions.

the lower part of Fig. 6.6 in Section 6.4).

Firstly, it is observed that the addition of QED in the process of DGLAP leads to a tendency to decrease the $q\bar{q}$ contribution to the cross section, increasingly so at higher rapidity. This is expected since observing Fig. 8.1, one notes that the quarks experience a reduction at high x of $\sim 1\%$ due to $q \to q + \gamma$ type splittings.

Secondly, the inclusion of PI contributions to the cross section is seen, as expected, to lead to an increase in the cross section relative to the QED corrected partons (the orange points in Figs. 9.2 to 9.6 as compared with the green) across all bins, as the inclusion of $x\gamma(x, Q^2)$ opens up new means for lepton pair production, unaccounted for in pure QCD calculations. Since the magnitude of the photon PDF is seen to become larger at low x, particularly at high scales ($Q^2 = 10^4 \sim 10^8$ GeV^2) and $\eta \simeq \frac{1}{2}\ln(x_1/x_2)$ where 1 and 2 denote the incoming photons, the predominance of the photon at low x manifests as an enhanced cross section contribution in the lower and intermediate η bins, an effect seen to hold across all mass bins.

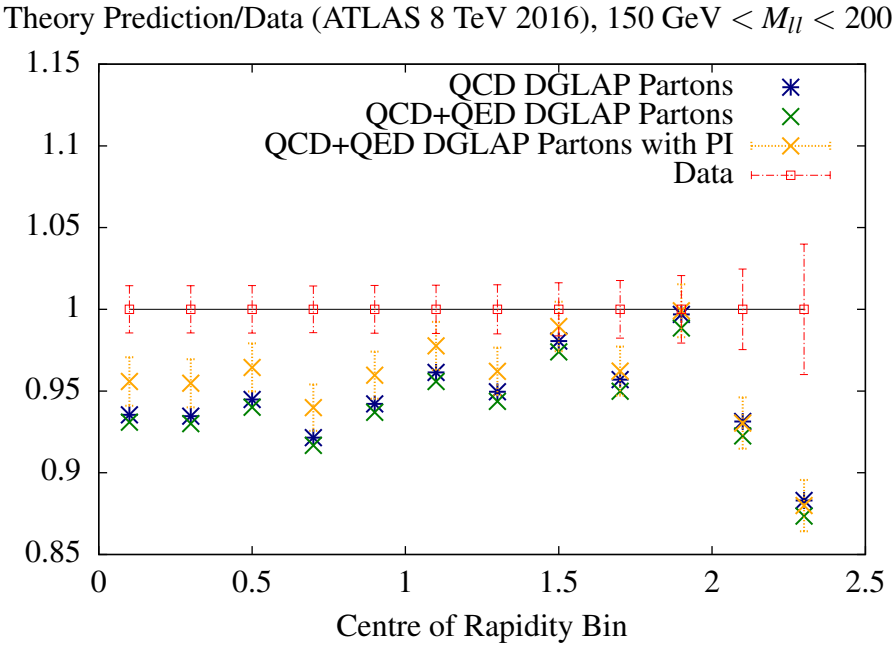

Figure 9.3: As the figure above, for the mass bin 150 GeV $< M_{ll} <$ 200 GeV

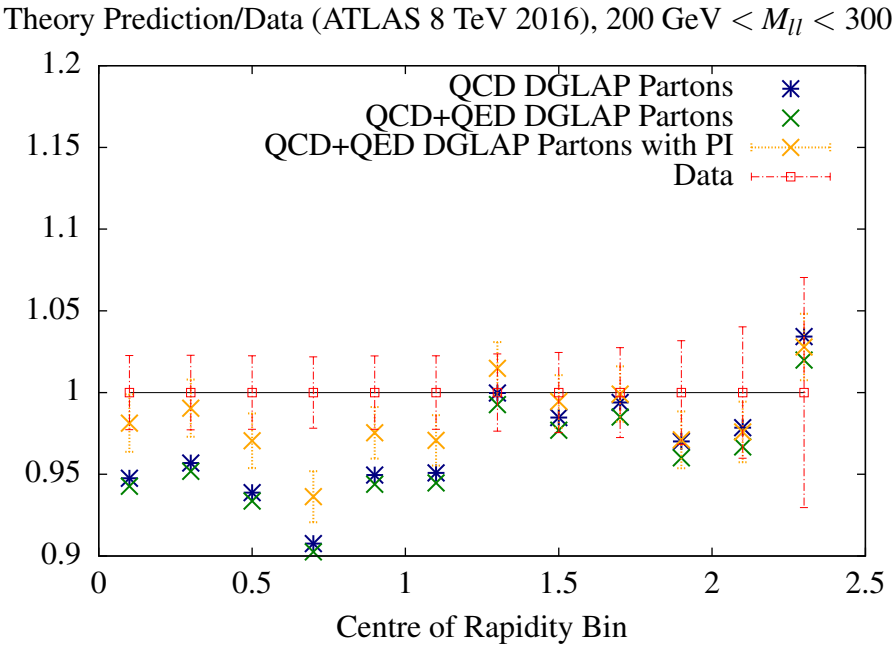

Figure 9.4: As the figure above, for the mass bin 200 GeV $< M_{ll} <$ 300 GeV

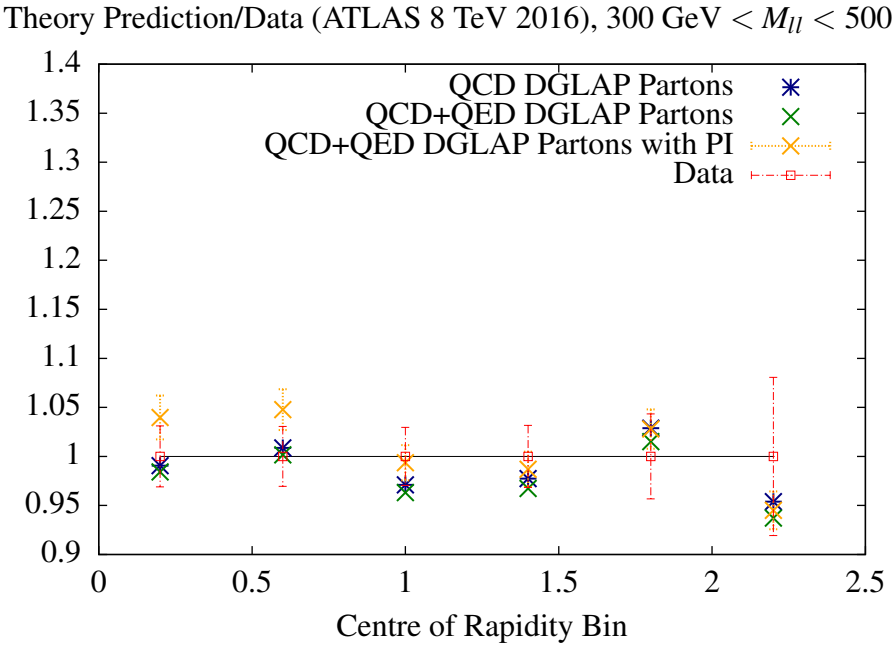

Figure 9.5: As the figure above, for the mass bin 300 GeV $< M_{ll} <$ 500 GeV

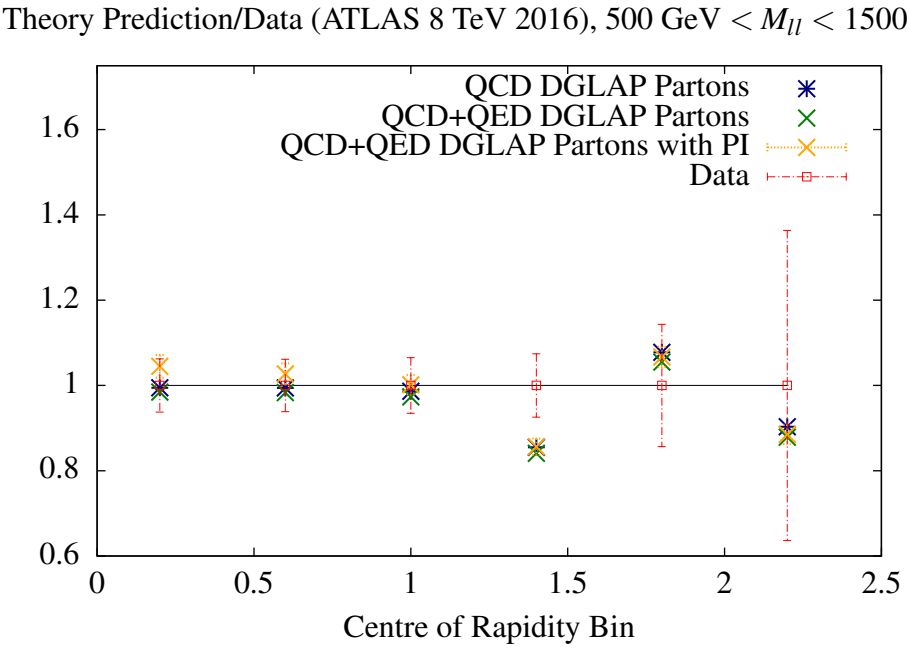

Figure 9.6: As the figure above, for the mass bin 500 GeV $< M_{ll} <$ 1500 GeV

Of note, however, is the fact that, at high η, the change due to QED inclusions in the evolution (the green points as compared with the blue, whose effect is only manifested as changes in the quarks and the gluon, as contributing to the NNLO QCD cross section calculation) is seen to be of comparable in magnitude to that of PI contributions (the orange points as compared with the green). In particular, we wish to highlight that for precision calculations of electroweak effects, one requires that all the partons be consistently treated (i.e. to contain all QED splittings for the quarks and gluons in an interdependent and coupled fashion) with QED in the evolution, as well as including the photon for a consistent treatment. This is especially noteworthy since the general trend of the partons after refitting with QED has an opposing effect on the cross section compared to that of PI contributions (due to a reduction of the total quark singlet), and as such, neglecting them can in principle lead to an over-estimation of the cross section where PI contributions are simply added on top of the standard QCD result, without the compensating effect in the other partons.

In fact, at high x, η, where PI contributions are relatively less important as $x\gamma(x, Q^2)$ rapidly diminishes, the effect of refitting the partons with QED is such that even the inclusion of PI contributions after accounting for QED in the evolution leads to a cross section less than that of the standard NNLO QCD prediction. In other words, the reduction of the total quark singlet content has a greater impact than the additional cross section contributions that are available from PI processes.

9.2 Sensitivity of a Global Fit to High Mass Drell-Yan Data

In the previous section, the cross section calculations were performed using a set of PDFs (for all three types of points represented in Figs. 9.2 to 9.6) which has not included the Drell-Yan data from ATLAS itself in the global fit for the determination of parton parameters. In the remainder of this section, we discuss the effects of including these data in the fit itself and the subsequent effect on the recalculation of the cross section.

In Figs. 9.7 to 9.11 we present the ratio of the cross section calculation from the QED corrected partons, including the contributions of PI processes both before and after refitting to the data with these effects. In these figures, it is seen that there is no substantial improvement in fit quality after refitting.

Of note however, is the fact that the PDF contributions to the uncertainties of the predicted cross sections (the sole contributuon to the uncertainty bands in Figs. 9.7 to 9.11) are incrementally reduced when refitting with the effects of QED included (best observed in the bins for high η, especially in the lower mass bins). In particular, we note that this incremental reduction is seen when refitting with the effects of QED in the evolution and with the inclusion of PI effects, but not when refit with purely with NNLO QCD parton evolution (and the absence of the photon). This indicates a weak preference to the effects of QED in the partons themselves and more accurate data may yet provide a better indication of how sensitive the comparison to the theory is with and without the effects outlined in this thesis.

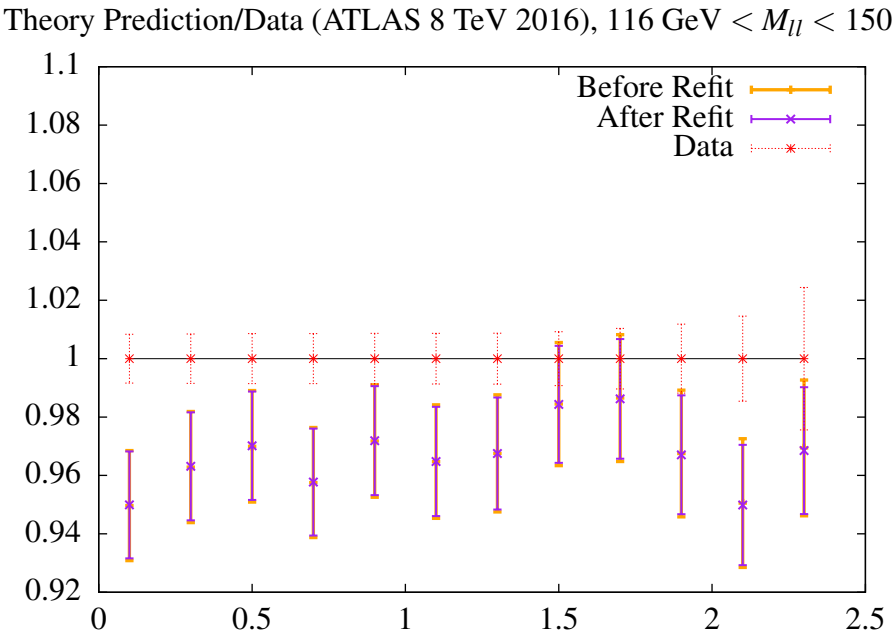

Figure 9.7: The ratio of theory to data for the cross section of Drell-Yan production in the mass bin 116 GeV $< M_{ll} <$ 150 GeV, differential in rapidity, as provided by the ATLAS experiment [23], with all PDF errors including those of the γ included. The ratios are provided for cross section calculations performed from QCD+QED PDFs with photon-initiated contributions, for PDFs fit with and without the high mass Drell-Yan data itself.

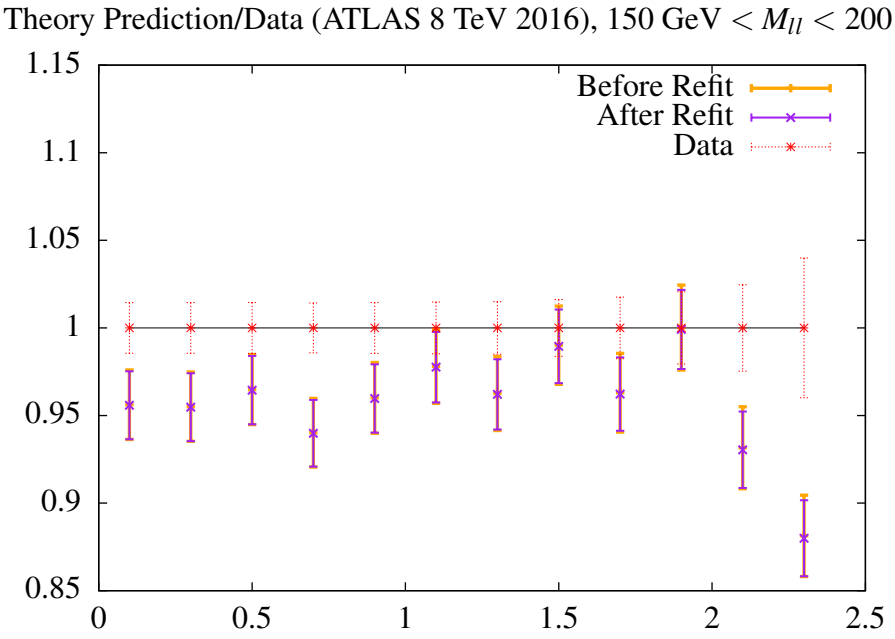

Figure 9.8: As the figure above, for the mass bin 150 GeV $< M_{ll} <$ 200 GeV

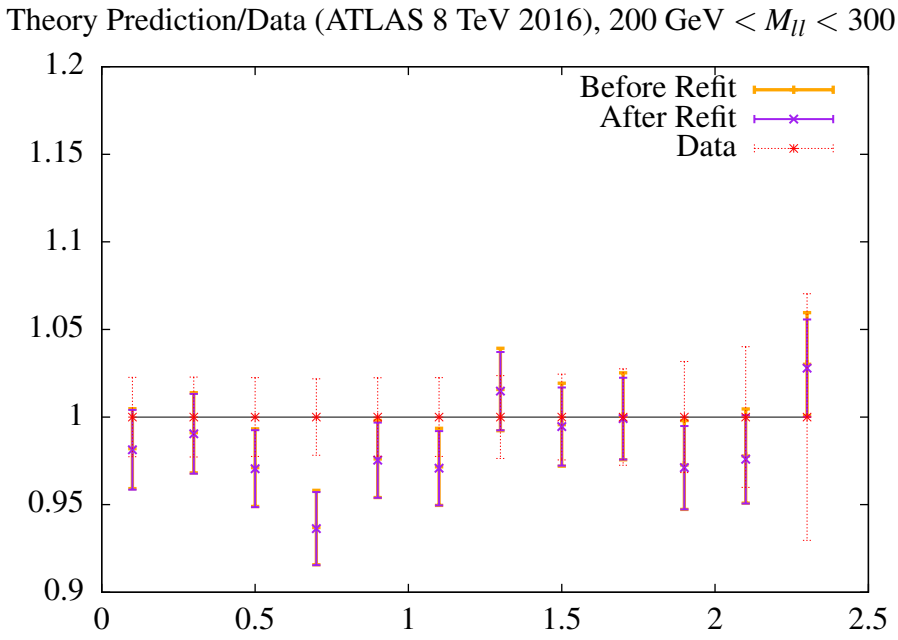

Figure 9.9: As the figure above, for the mass bin 200 GeV $< M_{ll} <$ 300 GeV

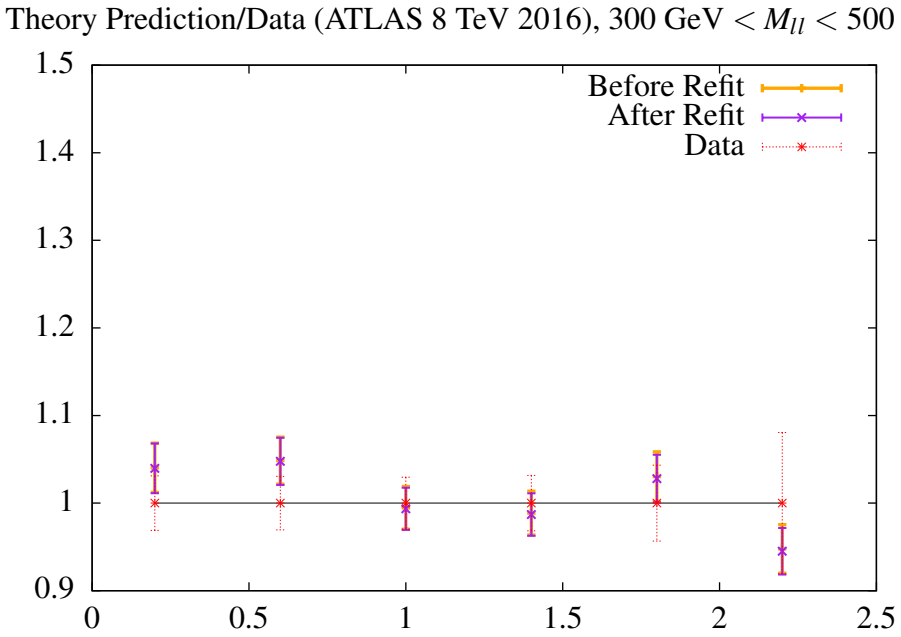

Figure 9.10: As the figure above, for the mass bin 300 GeV $< M_{ll} <$ 500 GeV

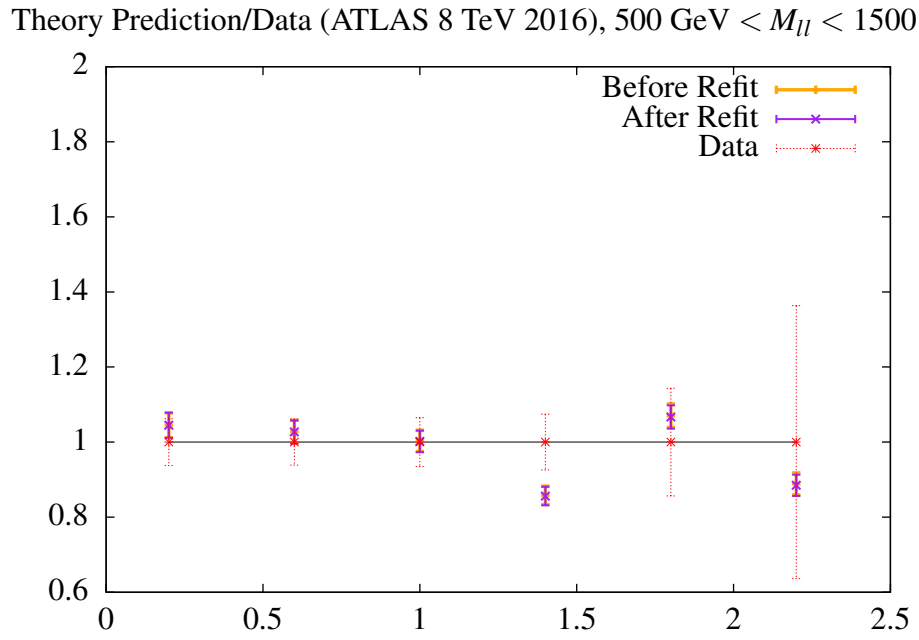

Figure 9.11: As the figure above, for the mass bin 500 GeV $< M_{ll} <$ 1500 GeV

Chapter 10

General Conclusions

In this thesis, the updated MMHT partons have been presented, modified to include the effects of QED in their evolution. Our resultant photon PDF, $x\gamma(x, Q^2)$, based on a similar methodology for the input to that of LUXqed is seen to bear a close resemblance in form with others in the literature, despite several modifications made to take into account our lower starting scale for the evolution and the use of a fully consistent, coupled DGLAP evolution using the MMHT PDFs.

Also outlined was the procedure developed to provide an approximate QED corrected DGLAP evolution for the PDFs of the neutron, leading to a neutron photon PDF (which was seen to be of a similar magnitude to that of the proton at higher Q^2), and isospin violating valence quark PDFs, which may hold importance for the future development of neutron PDFs and more significantly, the future development of nuclear PDFs which are already developed in the literature.

Although the fit quality remains broadly unchanged after refitting with these effects, it was observed that for the process of high-mass Drell-Yan production, the effects of both photon initiated processes, as well as changes in the quark and antiquark PDFs due to the effects of evolution, may become significant with the advent of precision measurements in this kinematic region and that the effects of QED in the evolution may be as significant as that of the photon, highlighting a need for a fully consistent set of QED corrected partons.

Finally, we note that the work undertaken in this thesis lays the foundation for the analysis of future data such as more precise Drell-Yan data and other such

processes (e.g. Higgs + W production) which are anticipated to be sensitive to photon-induced corrections and more generally, the improved theoretical accuracy of a QED corrected set of PDFs. In future, as the LHC is expected to move into a High Luminosity phase, as well as the PDFs providing the theoretical predictions needed for physics analyses, more accurate data may itself be able to provide alternative constraints to the photon as developed in this thesis.

Appendix A

χ^2 breakdown

Here the χ^2/N_{pts} (where N_{pts} represents the number of data points) are presented, broken down by data set for QCD and QCD + QED PDF fits, as described in Section 8.2, for both NLO and NNLO in QCD.

Change in χ^2 due to QED evolution compared to MMHT14+HERA I+II		
Data set	χ^2/N_{pts} **NNLO before fit (QCD)**	χ^2/N_{pts} **NNLO after fit(QCD+QED)**
BCDMS μp F_2 [132]	178 / 163	182 / 163 (+4)
BCDMS μd F_2 [133]	142 / 151	144 / 151 (+2)
NMC μp F_2 [134]	124 / 123	125 / 123
NMC μd F_2 [134]	108 / 123	108 / 123
NMC $\mu n/\mu p$ F_2 [135]	128 / 148	127 / 148
E665 μp F_2 [136]	65 / 53	65 / 53
E665 μd F_2 [136]	61 / 53	61 / 53
SLAC ep F_2 [137][138]	31 / 37	31 / 37
SLAC ed F_2 [137][138]	26 / 38	25 / 38
NMC/BCDMS/SLAC/HERA F_L [134, 132, 138, 139, 140, 141]	66 / 57	66 / 57
E866/NuSea pp DY [142]	224 / 184	223 / 184
E866/NuSea pd/pp DY [143]	11 / 15	11 / 15
NuTeV νN F_2 [144]	37 / 53	36 / 53 (-1)
CHORUS νN F_2 [145]	29 / 42	29 / 42
NuTeV νN xF_3 [144]	31 / 42	31 / 42
CHORUS νN xF_3 [145]	19 / 28	19 / 28
CCFR $\nu N \to \mu\mu X$ [146]	77 / 86	78 / 86
NuTeV $\nu N \to \mu\mu X$ [146]	42 / 84*	41 / 84*
HERA I+II CC e^+p [96]	52 / 39	52 / 39
HERA I+II CC e^-p [96]	63 / 42	65 / 42 (+2)
HERA I+II NC e^+p 920 GeV [96]	510 / 402	510 / 402
HERA I+II NC e^-p 920 GeV [96]	239 / 159	240 / 159 (+1)
HERA I+II NC e^+p 820 GeV [96]	88 / 75	88 / 75
HERA I+II NC e^-p 575 GeV [96]	261 / 259	262 / 259
HERA I+II NC e^-p 460 GeV [96]	246 / 209	246 / 209
HERA ep F_2^{charm} [147]	80 / 52	80 / 52
DØ II $p\bar{p}$ incl. jets [148]	117 / 110	117 / 110
CDF II $p\bar{p}$ incl. jets [149]	60 / 76	60 / 76
CDF II W asm. [150]	16 / 13	15 / 13
DØ II $W \to \nu e$ asym. [151]	31 / 12	30 / 12
DØ II $W \to \nu\mu$ asym. [152]	16 / 10	16 / 10
DØ II Z rap. [153]	17 / 28	17 / 28
CDF Z rap. [154]	40 / 28	40 / 28
ATLAS W^+, W^-, Z [155]	41 / 30	41 / 30
CMS W asymm $p_T > 35$ GeV [156]	7 / 11	7 / 11
CMS asymm $p_T > 25$ GeV, 30 GeV [157]	8 / 24	8 / 24
LHCb $Z \to e^+e^-$ [158]	22 / 9	22 / 9
LHCb W asymm $p_T > 20$ GeV [159]	14 / 10	13 / 10
CMS $Z \to e^+e^-$ [160]	23 / 35	22 / 35
ATLAS high-mass Drell-Yan [6]	17 / 13	18 / 13
CMS double diff. Drell-Yan [161]	152 / 132	152 / 132
Tevatron, ATLAS, CMS $\sigma_{t\bar{t}}$* [162, 163, 164, 165, 166, 167, 168]	14 / 18	14 / 18
All data	**3532 / 3276**	**3539/3276** (+7)

Change in χ^2 due to QED evolution compared to MMHT14+HERA I+II		
Data set	χ^2/N_{pts} **NLO before fit (QCD)**	χ^2/N_{pts} **NLO after fit(QCD+QED)**
BCDMS μp F_2 [132]	177 / 163	184 / 163 (+7)
BCDMS μd F_2 [133]	139 / 151	140 / 151
NMC μp F_2 [134]	135 / 123	136 / 123
NMC μd F_2 [134]	118 / 123	121 / 123 (+3)
NMC $\mu n/\mu p$ F_2 [135]	128 / 148	131 / 148 (+3)
E665 μp F_2 [136]	60 / 53	61 / 53
E665 μd F_2 [136]	52 / 53	52 / 53
SLAC ep F_2 [137][138]	31 / 37	30 / 37
SLAC ed F_2 [137][138]	31 / 38	30 / 38
NMC/BCDMS/SLAC/HERA F_L [134, 132, 138, 139, 140, 141]	73 / 57	72 / 57
E866/NuSea pp DY [142]	218 / 184	217 / 184 (-1)
E866/NuSea pd/pp DY [143]	12 / 15	12 / 15
NuTeV νN F_2 [144]	39 / 53	36 / 53 (-3)
CHORUS νN F_2 [145]	26 / 42	25 / 42
NuTeV νN xF_3 [144]	36 / 42	36 / 42
CHORUS νN xF_3 [145]	23 / 28	23 / 28
CCFR $\nu N \to \mu\mu X$ [146]	69 / 86	69 / 86
NuTeV $\nu N \to \mu\mu X$ [146]	41 / 84*	40 / 84*
HERA I+II CC e^+p [96]	51 / 39	50 / 39
HERA I+II CC e^-p [96]	76 / 42	79 / 42 (+3)
HERA I+II NC e^+p 920 GeV [96]	546 / 402	544 / 402 (-2)
HERA I+II NC e^-p 920 GeV [96]	248 / 159	248 / 159
HERA I+II NC e^+p 820 GeV [96]	89 / 75	89 / 75
HERA I+II NC e^-p 575 GeV [96]	268 / 259	268 / 259
HERA I+II NC e^-p 460 GeV [96]	254 / 209	253 / 209
HERA ep F_2^{charm} [147]	72 / 52	72 / 52
H1 9900 e^+p incl. jets	14 / 24	14 / 24
ZEUS incl. jets	45 / 60	45 / 60
DØ II $p\bar{p}$ incl. jets [148]	119 / 110	119 / 110
CDF II $p\bar{p}$ incl. jets [149]	65 / 76	69 / 76
CDF II W asm. [150]	16 / 13	16 / 13
DØ II $W \to \nu e$ asym. [151]	33 / 12	33 / 12
DØ II $W \to \nu\mu$ asym. [152]	16 / 10	16 / 10
DØ II Z rap. [153]	16 / 28	16 / 28
CDF Z rap. [154]	37 / 28	37 / 28
ATLAS W^+, W^-, Z [155]	38 / 30	39 / 30
CMS W asymm $p_T > 35$ GeV [156]	7 / 11	7 / 11
CMS asymm $p_T > 25$ GeV, 30 GeV [157]	7 / 24	7 / 24
LHCb $Z \to e^+e^-$ [158]	14 / 9	14 / 9
LHCb W asymm $p_T > 20$ GeV [159]	12 / 10	12 / 10
CMS $Z \to e^+e^-$ [160]	19 / 35	19 / 35
ATLAS high-mass Drell-Yan [6]	21 / 13	22 / 13
CMS double diff. Drell-Yan [161]	379 / 132	385 / 132 (+5)
Tevatron, ATLAS, CMS $\sigma_{t\bar{t}}$* [162, 163, 164, 165, 166, 167, 168]	14 / 18	14 / 18
ATLAS jets (2.76 TeV + 7 TeV)	110 / 116	111 / 116
CMS jets (7 TeV)	139 / 133	141 / 163 (+2)
All data	**4139 / 3609**	**4151/ 3609** (+12)

Appendix B

PDF Grids

As noted towards the end of Chapter 4 and Chapter 8, the set of QED corrected partons, MMHTqed, developed in this thesis will be released in the LHAPDF6 format for public use. The exact nature in which the grids are provided is clarified here. Each grid is a file labelled as 'MMHT2015qed_nlo_{type}_00{x}.dat' or 'MMHT2015qed_nnlo_{type}_00{x}.dat', where {type} is a label denoting which photon contribution is included in the set (described below) and $\{x\}$ represents numbers in the range $\{01, 02, ..., 62\}$. The particular uncertainties (as described above) associated with the numbers denoting each set are detailed in the Table B.1.

File number index $\{x\}$	**Corresponding Uncertainty**
01-50	The standard PDF uncertainties associated with the $q+\bar{q}$, $q-\bar{q}$ and g distributions for all flavours, as described in Chapter 4
51-52	The uncertainty contributions from A_2' (51: -0.4, 52:-0.2)
53-54	The uncertainty contributions from the Continuum contributions (53: Upper band, 54: Lower band)
55-56	The uncertainty contributions from the Resonance contributions (53: Upper band, 54: Lower band)
57-58	The uncertainty contributions from W_{cut} (57: 3 GeV^2, 58: 4 GeV^2)
59-60	The uncertainty contributions from R (59: +50%, 60: -50%)
61-62	The uncertainty contributions from the Elastic contributions (53: Upper band, 54: Lower band)

Table B.1: A table denoting how the numbering of the grid files (produced in the LHAPDF6 format) corresponds to the uncertainties listed in the text.

The grids are developed as three different sets, {type} = 'inelastic', 'elastic' or 'total', to accommodate three distinct representations of the photon PDF, $\gamma^{(inel)}$, $\gamma^{(el)}$ and $\gamma = \gamma^{(inel)} + \gamma^{(el)}$. This is because the LHAPDF6 format also requires that in each file for a given grid, each column, which represents a given PDF distribution, be labelled with an associated number from the Monte Carlo Particle Numbering Scheme as described in [38], where every flavour of particle is associated with an integer. This represents an obstacle for the photon distributions as represented in this paper, since only one such number is allocated for the γ, 22, while we wish to distinguish between the total, the elastic and the inelastic components.

To provide users with the ability to call upon γ, $\gamma^{(el)}$, $\gamma^{(inel)}$, as needed, we provide three separate PDF sets for each use case. Each set contains the full 62 eigenvector uncertainties as well as the central values described in Section 8.3. For example at NNLO, the 'MMHT2015qed_nnlo_total' set provides the full $\gamma = \gamma^{(el)} + \gamma^{(inel)}$ distribution in the column reserved for the photon (22). The 'MMHT2015qed_nnlo_inelastic' set provides the $\gamma^{(inel)}(x, Q^2)$ distribution while the 'MMHT2015qed_nnlo_elastic' set provides the $\gamma^{(el)}(x, Q^2)$ distribution (with the corresponding NLO PDF sets labelled appropriately). Users should therefore distinguish by name the appropriate LHAPDF6 variables in code for each distinct photon component as needed, calling each from the sets as labelled above.

Appendix C

Colophon

This document was set in the Times Roman typeface using LaTeX and BibTeX, composed on Overleaf and makes use of the UCL thesis template provided there. The software used in the production of results and figures was primarily the MMHT source code as modified by the author, with additional software provided from Applgrid. The grids were converted into LHAPDF6 format using code adapted from that provided by Lucian Harland-Lang and Shaun Bailey. All plots, where not cited from elsewhere, were generated using gnuplot and Feynman diagrams were generated in JaxoDraw. No physicists were seriously harmed in the making of this thesis.

Bibliography

[1] Joseph D. Lykken, CERN Yellow Report CERN-2010-002 101-109, arXiv:1005.1676

[2] Juan Rojo, Nuovo Cim. C037 (2014) no.6, 101-109, arXiv:1404.7071

[3] G. Altarelli and G. Parisi. (1977) Nucl.Phys. B126:298

[4] Yu.L. Dokshitzer. (1977) Sov.Phys. JETP 46:641

[5] V.N. Gribov, L.N. Lipatov. (1972) Sov.J.Nucl.Phys. 15:438

[6] ATLAS Collaboration, G. Aad et al., Phys. Lett. B 725 (2013) 223-242, arXiv:1305.4192

[7] A. Bierweiler, T. Kasprzik, H. Kuhn, and S. Uccirati, JHEP 1211 093 (2012), arXiv:1208.3147

[8] A. Denner, S. Dittmaier, S. Kallweit, and A. Muck, JHEP 03 075 (2012), arXiv:1112.5142

[9] L. A. Harland-Lang, V. A. Khoze, M. G. Ryskin, M.G. Eur. Phys. J. C (2016) 76: 255., arXiv:1601.03772

[10] Harland-Lang, L.A., Khoze, V.A., Ryskin, M.G. et al. J. High Energ. Phys. (2019) 2019: 10, arXiv:1812.04886

[11] L. Beresford, J. Liu, arXiv:1811.06465v1 [hep-ph]

[12] A.D. Martin, R.G. Roberts, W.J. Stirling, R.S. Thorne, Eur.Phys.J.C39:155-161 (2005), arXiv:0411040

[13] Carl Schmidt, Jon Pumplin, Daniel Stump, and C.P. Yuan, Phys. Rev. D 93, 114015 (2016), arXiv: 1509.02905

[14] The NNPDF Collaboration: Richard D. Ball et al, Nuclear Physics B 877(2), arXiv:1308.0598

[15] Giuli, F. and the xFitter Developers team Eur. Phys. J. C (2017) 77: 400. arXiv:1701.08553

[16] Martin, A.D. Ryskin, M.G. Eur. Phys. J. C (2014) 74: 3040. arXiv: 1406.2118

[17] L.A. Harland-Lang, V.A. Khoze, M.G. Ryskin, Phys. Rev. D 94, 074008 (2016), arXiv:1607.04635

[18] L. A. Harland-Lang, V. A. Khoze, M. G. Ryskin, Photon 2017: International Conference on the Structure and the Interactions of the Photon and 22th International Workshop on Photon-Photon Collisions and the International Workshop on High Energy Photon Colliders CERN, May 22-26, arXiv:1709.00176

[19] Aneesh Manohar, Paolo Nason, Gavin P. Salam, Giulia Zanderighi, Phys. Rev. Lett. 117, 242002, arXiv:1607.04266

[20] Daniel de Florian, German F. R. Sborlini, German Rodrigo, G. Eur. Phys. J. C (2016) 76: 282, arXiv:1512.00612

[21] Daniel de Florian, German F. R. Sborlini, German Rodrigo, Journal of High Energy Physics, Volume 2004, JHEP07(2004), arXiv:1606.02887

[22] G.P. Zeller et al., Phys. Rev. Lett. 88 (2002) 091802, arXiv:hep-ex/0110059

[23] ATLAS Collaboration, G. Aad et al., JHEP 08 (2016) 009, arXiv:1606.01736

[24] D. Hanneke, S. Fogwell, G. Gabrielse, Phys.Rev.Lett.100:120801 (2008), arXiv:0801.1134

[25] E. Rutherford, F.R.S., Philosophical Magazine Series 6, vol. 21 May 1911, p. 669-688

[26] J. Chadwick 136 Proceedings of the Royal Society of London. Series A, Containing Papers of a Mathematical and Physical Character

[27] Cathryn Carson, SLAC Beam Line 30N2 (2000) 6, https://www.slac.stanford.edu/pubs/beamline/30/2/30-2-carson.pdf

[28] David Griffiths, Introduction to Elementary Particles, Wiley VCH; 2nd, Revised edition (20 Aug. 2008)

[29] G. Zweig, CERN-TH-412, https://cds.cern.ch/record/570209 (1964)

[30] Y. Neeman, Nuclear Physics 26 (1961) p. 222.

[31] M. Gell-Mann, Phys. Rev. 125 (1962) p. 1067

[32] H. Fritzsch, M. Gell-Mann, and H. Leutwyler, Phys. Lett. B 47 (1973) p. 365

[33] M. Gell-Mann, Phys. Lett. 8 (1964) p. 214

[34] S. Glashow, Nucl. Phys. 22 (1961) p. 579

[35] S. Weinberg, Phys. Rev. Lett. 19 (1967) p. 1264

[36] A. Salam, Proceedings of the Eighth Nobel Symposium, Conf. Proc. C680519 (1968) p. 367

[37] Emmanual A. Paschos, Electroweak Theory, Cambridge University Press (2007)

[38] M. Tanabashi et al. (Particle Data Group), Phys. Rev. D 98, 030001 (2018).

[39] ATLAS Collaboration, G. Aad et al., Phys.Lett. B716 (2012) 1-29, arXiv: 1207.7214

[40] CMS Collaboration, Phys. Lett. B 716 (2012) 30, arXiv:1207.7235

[41] Gerard 't Hooft and M.J.G. Veltman, Nucl.Phys. B44 (1972) 189-213

[42] F. Englert and R. Brout, Phys. Rev. Lett. 13 (1964) p. 321

[43] P. W. Higgs, Phys. Rev. Lett. 13 (1964) p. 508

[44] G. S. Guralnik, C. R. Hagen, and T. W. B. Kibble, Phys. Rev. Lett. 13 (1964) p. 585

[45] T. W. B. Kibble, Phys. Rev. 155 (1967) p. 1554

[46] N. Cabibbo, Phys. Rev. Lett. 10, 531 (1963).

[47] M. Kobayashi, T. Maskawa; Maskawa (1973) Progress of Theoretical Physics. 49 (2): 652657

[48] B. Pontecorv, Sov.Phys.JETP 7 (1958) 172-173,

[49] Z. Maki, M. Nakagawa, S. Sakata, Progress of Theoretical Physics, Vol. 28, No. 5, pp. 870-880

[50] Dyson, F. J. (1949), Phys. Rev. 75 (3): 486502.

[51] Ling-Fong Li, 100 Years of Subatomic Physics, pp. 465-491 (2013), arXiv:1208.4700

[52] F. Hautmann, Quantum Chromodynamics, University of Antwerp Physics Department, 2016 (lecture notes)

[53] C. G. Callan, Phys. Rev. D 2 (1970) p. 1541.

[54] K. Symanzik, Commun. Math. Phys. 18 (1970) p. 227.

[55] Gross, D. J. and Wilczek,F., Phys. Rev. Lett. 30 , 1343 (1973)

[56] Politzer, H.D., Phys. Rev. Lett. 30, 1346 (1973)

[57] The CMS collaboration, Khachatryan, V., Sirunyan, A.M. et al. J. High Energ. Phys. (2017) 2017: 156., arXiv:1609.05331

[58] On the Interaction of Elementary Particles, H. Yukawa (1935)

[59] V. E. Barnes et al, Phys. Rev. Lett. 12, 204 (1964)

[60] M. Gell-Mann (1964). Physics Letters. 8 (3): 214215.

[61] G. Zweig (1964). CERN Report No.8182/TH.401.

[62] M. Breidenbach, et al., Phys. Rev. Lett.23 (1969) 935

[63] J I Friedman, and, and H W Kendall, Annual Review of Nuclear Science 1972 22:1, 203-254

[64] A. De Roeck R.S. Thorne, March 2011 Progress in Particle and Nuclear Physics 66(4), arXiv:1103.0555

[65] M. Tanabashi et al. (Particle Data Group), Phys. Rev. D 98, 030001 (2018), Section 19 (Structure Functions)

[66] C. G. Callan, Jr. and David J. Gross, Phys. Rev. Lett. 22, 156

[67] John C. Collins, Davison E. Soper George Sterman, Adv.Ser.Direct.High Energy Phys. 5 (1989) 1-91

[68] Tao Han, Joshua Sayre, Susanne Westhoff, Journal of High Energy Physics, April 2015, 2015:145, arXiv:1411.2588 [hep-ph]

[69] S. Dawson, A. Ismail, Ian Low, Phys. Rev. D 90, 014005 (2014), arXiv:1405.6211 [hep-ph]t

[70] M. Lim et al , J. High Energ. Phys. (2016) 2016: 132., arXiv:1605:09411

[71] J. Butterworth et al., J. Phys. G43, 023001 (2016), arXiv:1510.03865

[72] The NNPDF Collaboration: Richard D. Ball et al, Eur. Phys. J. C (2017) 77: 663., arXiv: 1706.00428

[73] Tie-Jiun Hou, Sayipjamal Dulat et al, J. High Energ. Phys. (2018) 2018: 59., arXiv: 1707.00657

[74] Ball, R.D., Bertone, V., Carrazza, S. et al. Eur. Phys. J. C (2017) 77: 663., arXiv:1706:00428

[75] Abramowicz, H., Abt, I., Adamczyk, L. et al. Eur. Phys. J. C (2015) 75: 580., arXiv: 1506.06042

[76] S. Alekhin, J. Bluemlein, S. Moch , R. Placakyte, Phys. Rev. D 96, 014011 (2017), 1701.05838

[77] Sayipjamal Dulat et al, Phys. Rev. D 93, 033006 (2016), arXiv:1506.07443

[78] Harland-Lang, L.A., Martin, A.D., Motylinski, P. et al. Eur. Phys. J. C (2015) 75: 204., arXiv: 1412.3989

[79] Martin, A.D., Stirling, W.J., Thorne, R.S. et al. Eur. Phys. J. C (2009) 63: 189., arXiv:0901.0002

[80] G. Watt, R. S. Thorne, J. High Energ. Phys. (2012) 2012: 52, arXiv:1205.4024

[81] Carrazza, S., Forte, S., Kassabov, Z. et al. Eur. Phys. J. C (2015) 75: 369., arXiv:1505.06736

[82] A. D. Martin et al., Eur.Phys.J. C73, 2318 (2013), arXiv:1211.1215

[83] A. D. Martin, R. Roberts, W. Stirling, and R. Thorne, Eur.Phys.J. C23, 73 (2002), arXiV: hep-ph/0110215

[84] D. Stump et al, Phys.Rev.D65:014012 (2001), arXiv:hep-ph/0101051

[85] J. Pumplin et al, JHEP 0207:012 (2002), arXiv:hep-ph/0201195

[86] K. Levenberg, A Method for the Solution of Certain Non-Linear Problems in LeastSquares, Quart. Appl. Math.2(1944) 164.

[87] D. W. Marquardt, An Algorithm for Least-Squares Estimation of Nonlinear Parameters, SIAM J. Appl. Math.11(1963) 431, doi:10.1137/0111030.

[88] A. Buckley et al, Eur.Phys.J. C75 (2015) 3, 132, arXiv:1412.7420

[89] L. A. Harland-Lang, A. D. Martin, P. Motylinski, R. S. Thorne, Eur. Phys. J. C (2016) 76:10, arXiv: 1601.03413

[90] Valerio Bertone, Stefano Carrazza, Nathan P. Hartland, Juan Rojo, SciPost Phys. 5, 008 (2018), arXiv:1712.07053v1

[91] C. F. von Weizsacker, Z. Phys. 88, 612 (1934)

[92] E. J. Williams, Phys. Rev. 45, 729 (1934).

[93] E. Fermi, Z. Phys. 29, 315 (1924)

[94] Budnev, V.M. et al., Nucl.Phys. B34 (1971) 470-476

[95] Budnev V.M et al, Physics Reports Volume 15, Issue 4, January (1975), Pages 181-282

[96] ZEUS, H1, H. Abramowicz et al., (2015). arXiv:1506.06042

[97] ZEUS collaboration: S. Chekanov et al., Phys. Lett. B595 (2004) 86

[98] M. Glck, C. Pisano, E. Reya, Phys.Lett.B540:75-80,2002, arXiv: 0206126

[99] Aneesh Manohar, Paolo Nason, Gavin P. Salam, and Giulia Zanderighi, J. High Energ. Phys. (2017) 2017, arXiv:1708.01256

[100] A1 collaboration, J. C. Bernauer et al., Phys. Rev. C90 (2014) 015206, arXiv:1307.6227.

[101] CLAS collaboration, M. Osipenko et al., Phys. Rev. D 67, 092001, arXiv:hep-ph/0301204.

[102] HERMES collaboration, A. Airapetian et al., J. High Energ. Phys. (2011) 2011: 126, arXiv:1103.5704.

[103] E143 collaboration, K. Abe et al. Phys. Lett. B452 (1999) 194200, [hep-ex/9808028]

[104] M. E. Christy and P. E. Bosted, Phys. Rev. C 81, 055213, arXiv:0712.3731.

[105] Bertone, V., Carrazza, S., Pagani, D. et al. J. High Energ. Phys. (2015) 2015: 194., arXiv: 1508.07002

[106] Bauer, C.W., Ferland, N. Webber, B.R. J. High Energ. Phys. (2017) 2017: 36., arXiv: 1703.08562

[107] R. J. FRIES, arXiv: hep-ph/0201311

[108] R.K. Ellis, W.J. Stirling and B.R Weber, QCD and Collider Physics, Cambridge Monographs on Particle Physics, Nuclear Physics and Cosmology (1996).

[109] I. Schienbein et al. , J. Phys. G 35 (2008) 053101 arXiv:0709.1775

[110] M. Dasgupta and B.R. Webber, Phys.Lett. B382 (1996) 273-281, arXiv:hep-ph/9604388

[111] M. Virchaux and A. Milsztajn, Phys.Lett. 274B (1992) 221, https://www.sciencedirect.com/journal/physics-letters-b/vol/274/issue/2

[112] J. Pumplin, D. R. Stump, J. Huston, H. L. Lai, P. M. Nadolsky and W. K. Tung, JHEP 0207 (2002) 012, arXiv:hep-ph/0201195

[113] G. Onengut et al. [CHORUS Collaboration], Phys. Lett. B 632 (2006) 65.

[114]] Y. L. Dokshitzer, G. Marchesini and B. R. Webber, Nucl. Phys. B 469 (1996) 93, arXiv:hep-ph/9512336

[115] K.J. Eskola, P. Paakkinen, H. Paukkunen and C.A. Salgado, Eur.Phys.J. C77 (2017) no.3, 163, arXiv:1612.05741

[116] K. Kovarik et al, Phys. Rev. D 93, 085037 (2016), arXiv:1509.00792

[117] K.J. Eskola, P. Paakkinen, H. Paukkunen and C.A. Salgado, Eur Phys J C Part Fields. 2017; 77(3): 163, arXiv:1612.05741

[118] S. Galster, H. Klein, J. Moritz, K. Schmidt, D. Wegener, and J. Bleckwenn, Nucl. Phys. B32 , 221 (1971)

[119] J.J. Kelly, Physical Review C 70, 068202 (2004)

[120] C. F. Perdrisat, V. Punjabi, M. Vanderhaeghen, Prog.Part.Nucl.Phys.59:694-764,2007, arXiv:hep-ph/0612014v2

[121] Bardeen, William A. and Buras, A. J. and Duke, D. W. and Muta, T., Phys. Rev. D18 (1978) 3998

[122] L. A. Harland-Lang, M. G. Ryskin, V. A. Khoze, Phys.Lett. B761 (2016) 20-24, arXiv:1605.04935

[123] L Adamczyk et al. (ATLAS) , Tech. Rep. CERN-LHCC-2015-009. ATLAS-TDR-024 (2015)

[124] M Albrow et al. (CMS and TOTEM Diffractive and Forward Physics Working Group), TOTEM-TDR-003, CMS-TDR13 (CERN, Geneva, 2006)

[125] V.A. Khoze, A.D. Martin, M.G. Ryskin, Eur. Phys. J. C (2013) 73: 2503, arXiv:1306.2149

[126] L. A. Harland-Lang, R. S. Thorne, Harland-Lang, L.A. Thorne, R.S. Eur. Phys. J. C (2019) 79: 225, arXiv:1811.08434

[127] ATLAS Collaboration, G. Aad et al., Eur. Phys. J. C 77 (2017) 367, arXiv:1612.03016

[128] J. Alwall, R. Frederix, S. Frixione, V. Hirschi, F. Maltoni, et al., JHEP 1407 (2014) 079, arXiv:1405.0301

[129] V. Bertone, R. Frederix, S. Frixione, J. Rojo, and M. Sutton, JHEP 1408 (2014) 166, arXiv:1406.7693

[130] R. Gavin, Y. Li, F. Petriello, and S. Quackenbush, Comput.Phys.Commun. 184 (2013) 208214, arXiv:1201.5896

[131] T. Carli, et al, The APPLGRID Project, Eur. Phys. J. C66 (2010) 503524, arXiv:0911.2985

[132] BCDMS Collaboration, A. Benvenuti et al., Phys.Lett. B223, 485 (1989).

[133] BCDMS Collaboration, A. Benvenuti et al., Phys.Lett. B237, 592 (1990)

[134] New Muon Collaboration, M. Arneodo et al., Nucl.Phys. B483, 3 (1997), hep-ph/9610231

[135] New Muon Collaboration, M. Arneodo et al., Nucl.Phys. B487, 3 (1997), hep-ex/9611022

[136] E665 Collaboration, M. Adams et al., Phys.Rev. D54, 3006 (1996)

[137] L. Whitlow, E. Riordan, S. Dasu, S. Rock, and A. Bodek, Phys.Lett. B282, 475 (1992)

[138] L. Whitlow, S. Rock, A. Bodek, E. Riordan, and S. Dasu, Phys.Lett. B250, 193 (1990).

[139] H1 Collaboration, F. Aaron et al., Phys.Lett. B665, 139 (2008), arXiv:0805.2809

[140] H1 Collaboration, F. Aaron et al., Eur.Phys.J. C71, 1579 (2011), arXiv:1012.4355

[141] ZEUS Collaboration, S. Chekanov et al., Phys.Lett. B682, 8 (2009), arXiv:0904.1092

[142] J. C. Webb, (2003), hep-ex/0301031

[143] NuSea Collaboration, R. Towell et al., Phys.Rev. D64, 052002 (2001), hep-ex/0103030

[144] NuTeV Collaboration, M. Tzanov et al., Phys.Rev. D74, 012008 (2006), hep-ex/0509010

[145] CHORUS Collaboration, G. Onengut et al., Phys.Lett. B632, 65 (2006)

[146] NuTeV Collaboration, M. Goncharov et al., Phys.Rev. D64, 112006 (2001), hepex/0102049

[147] H1 Collaboration, ZEUS Collaboration, H. Abramowicz et al., Eur.Phys.J. C73, 2311 (2013), 1211.1182

[148] D0 Collaboration, V. M. Abazov et al., Phys.Rev. D85, 052006 (2012), arXiv:1110.3771

[149] CDF Collaboration, A. Abulencia et al., Phys.Rev. D75, 092006 (2007), hep-ex/0701051

[150] CDF Collaboration, T. Aaltonen et al., Phys.Rev.Lett. 102, 181801 (2009), arXiv:0901.2169

[151] D0 Collaboration, V. Abazov et al., Phys.Rev.Lett. 101, 211801 (2008), arXiv:0807.3367

[152] D0 Collaboration, V. M. Abazov et al., Phys.Rev. D88, 091102 (2013), arXiv:1309.2591

[153] D0 Collaboration, V. Abazov et al., Phys.Rev. D76, 012003 (2007), hep-ex/0702025

[154] CDF Collaboration, T. A. Aaltonen et al., Phys.Lett. B692, 232 (2010), arXiv:0908.3914

[155] ATLAS Collaboration, G. Aad et al., Phys.Rev. D85, 072004 (2012), arXiv:1109.5141

[156] CMS Collaboration, S. Chatrchyan et al., Phys.Rev.Lett. 109, 111806 (2012), arXiv:1206.2598

[157] CMS Collaboration, S. Chatrchyan et al., JHEP 1104, 050 (2011), arXiv:1103.3470

[158] LHCb collaboration, R. Aaij et al., JHEP 1302, 106 (2013), arXiv:1212.4620

[159] LHCb Collaboration, R. Aaij et al., JHEP 1206, 058 (2012), arXiv:1204.1620

[160] CMS Collaboration, S. Chatrchyan et al., Phys.Rev. D85, 032002 (2012), arXiv:1110.4973

[161] CMS Collaboration, S. Chatrchyan et al., JHEP 1312, 030 (2013), arXiv:1310.7291

[162] CDF Collaboration, D0 Collaboration, T. A. Aaltonen et al., Phys.Rev. D89, 072001 (2014), arXiv:1309.7570

[163] ATLAS Collaboration, G. Aad et al., Eur.Phys.J. C71, 1577 (2011), arXiv:1012.1792

[164] ATLAS Collaboration, G. Aad et al., Phys.Lett. B707, 459 (2012), arXiv:1108.3699

[165] ATLAS Collaboration, G. Aad et al., Phys.Lett. B711, 244 (2012), arXiv:1201.1889

[166] ATLAS Collaboration, G. Aad et al., JHEP 1205, 059 (2012), arXiv:1202.4892

[167] ATLAS Collaboration, G. Aad et al., Phys.Lett. B717, 89 (2012), arXiv:1205.2067

[168] ATLAS Collaboration, G. Aad et al., Eur.Phys.J. C73, 2328 (2013), arXiv:1211.7205